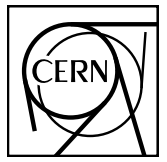


# EUROPEAN ORGANIZATION FOR NUCLEAR RESEARCH



ALICE-ANA-2016-xxx  
March 16, 2018

## Lambda-Kaon and Cascade-Kaon Femtoscopy in Pb-Pb Collisions at $\sqrt{s_{NN}} = 2.76 \text{ TeV}$ from the LHC ALICE Experiment

Jesse T. Buxton<sup>1</sup>

1. Department of Physics, The Ohio State University, Columbus, Ohio, USA

Email: jesse.thomas.buxton@cern.ch

### Abstract

We present results from a femtoscopic analysis of Lambda-Kaon correlations in Pb-Pb collisions at  $\sqrt{s_{NN}} = 2.76 \text{ TeV}$  by the ALICE experiment at the LHC. All pair combinations of  $\Lambda$  and  $\bar{\Lambda}$  with  $K^+$ ,  $K^-$  and  $K_S^0$  are analyzed. The femtoscopic correlations are the result of strong final-state interactions, and are fit with a parametrization based on a model by R. Lednicky and V. L. Lyuboshitz [1]. This allows us to both characterize the emission source and measure the scattering parameters for the particle pairs. We observe a large difference in the  $\Lambda K^+$  ( $\bar{\Lambda} K^-$ ) and  $\Lambda K^-$  ( $\bar{\Lambda} K^+$ ) correlations in pairs with low relative momenta ( $k^* \lesssim 100 \text{ MeV}$ ). Additionally, the average of the  $\Lambda K^+$  ( $\bar{\Lambda} K^-$ ) and  $\Lambda K^-$  ( $\bar{\Lambda} K^+$ ) correlation functions is consistent with our  $\Lambda K_S^0$  ( $\bar{\Lambda} K_S^0$ ) measurement. The results suggest an effect arising from different quark-antiquark interactions in the pairs, i.e.  $s\bar{s}$  in  $\Lambda K^+$  ( $\bar{\Lambda} K^-$ ) and  $u\bar{u}$  in  $\Lambda K^-$  ( $\bar{\Lambda} K^+$ ). To gain further insight into this hypothesis, we currently are conducting a  $\Xi$ -K femtoscopic analysis.



## Contents

<b>1</b>	<b>Introduction</b>	<b>6</b>
<b>2</b>	<b>Data Sample and Software</b>	<b>6</b>
2.1	Data Sample . . . . .	6
2.2	Software . . . . .	6
<b>3</b>	<b>Data Selection</b>	<b>6</b>
3.1	Event Selection and Mixing . . . . .	6
3.2	K $^{\pm}$ Track Selection . . . . .	7
3.3	V0 Selection . . . . .	8
3.3.1	Λ Reconstruction . . . . .	9
3.3.2	K $_S^0$ Reconstruction . . . . .	11
3.4	Cascade Reconstruction . . . . .	14
3.5	Pair Selection . . . . .	16
<b>4</b>	<b>Correlation Functions</b>	<b>20</b>
<b>5</b>	<b>Fitting</b>	<b>24</b>
5.1	Model: ΛK $_S^0$ , ΛK $^{\pm}$ , Ξ $^{ch}$ K $_S^0$ . . . . .	24
5.2	Model: Ξ $^{ch}$ K $^{ch}$ . . . . .	24
5.3	Momentum Resolution Corrections . . . . .	25
5.4	Residual Correlations . . . . .	29
5.5	Non-Flat Background . . . . .	38
5.6	LednickyFitter . . . . .	38
5.7	Coulomb Fitter . . . . .	39
<b>6</b>	<b>Systematic Errors</b>	<b>40</b>
6.1	Systematic Errors: ΛK $_S^0$ . . . . .	40
6.1.1	Particle and Pair Cuts . . . . .	40
6.1.2	Non-Flat Background . . . . .	41
6.1.3	Fit Range . . . . .	41
6.2	Systematic Errors: ΛK $^{\pm}$ . . . . .	41
6.2.1	Particle and Pair Cuts . . . . .	41
6.2.2	Non-Flat Background . . . . .	41

6.2.3	Fit Range	41
6.3	Systematic Errors: $\Xi K^\pm$	42
6.3.1	Particle and Pair Cuts	42
<b>7</b>	<b>Results and Discussion</b>	<b>42</b>
7.1	Results: $\Lambda K_S^0$ and $\Lambda K^\pm$	42
7.1.1	Results: $\Lambda K_S^0$ and $\Lambda K^\pm$ : No Residual Correlations Included in Fit	47
7.1.2	Results: $\Lambda K_S^0$ and $\Lambda K^\pm$ : 3 Residual Correlations Included in Fit	56
7.1.3	Results: $\Lambda K_S^0$ and $\Lambda K^\pm$ : 10 Residual Correlations Included in Fit	66
7.2	Results: $\Xi K^\pm$	76
<b>8</b>	<b>To Do</b>	<b>77</b>
<b>9</b>	<b>Additional Figures</b>	<b>82</b>
9.1	Residuals	82
9.1.1	$\Lambda K^+$ Residuals	82
9.1.2	$\Lambda K^-$ Residuals	88
9.1.3	$\Lambda K_S^0$ Residuals	94

## List of Figures

1	V0 Reconstruction	9
2	$K_S^0$ contamination in $\Lambda(\bar{\Lambda})$ collection	10
3	$\Lambda$ and $\bar{\Lambda}$ Purity	11
4	$\Lambda(\bar{\Lambda})$ contamination in $K_S^0$ collection	13
5	$K_S^0$ Purity	14
6	$\Xi$ Reconstruction	15
7	$\Xi^-(\bar{\Xi}^+)$ Purity	16
8	Average Separation of $\Lambda(\bar{\Lambda})$ and $K_S^0$ Daughters	17
9	Average Separation of $\Lambda(\bar{\Lambda})$ Daughter and $K^\pm$	18
10	Average Separation of $\Xi$ Daughters and $K^\pm$	19
11	$\Lambda(\bar{\Lambda})K_S^0$ Correlation Functions	21
12	$\Lambda K^+$ and $\bar{\Lambda} K^-$ Correlation Functions	22
13	$\Lambda K^-$ and $\bar{\Lambda} K^+$ Correlation Functions	23
14	Correlation Functions: $\Lambda K^+$ vs $\Lambda K^-$ for 0-10% Centrality	23
15	Momentum Resolution: Sample $k_{True}^*$ vs. $k_{Rec}^*$	27
16	Particle Contaminations Visible in $k_{True}^*$ vs. $k_{Rec}^*$	28
17	Transform Matrices for $\Lambda K^+$ Analysis	30
18	Transform Matrices for $\bar{\Lambda} K^+$ Analysis	31
19	$\Sigma^0 K^+$ Transform	36
20	$\Sigma^0 K^+$ Transform	37
21	Scattering Parameter Results	43
22	$\lambda$ vs. R (0-10% Centrality)	44
23	$\lambda$ vs. R (10-30% Centrality)	45
24	$\lambda$ vs. R (30-50% Centrality)	46
25	$\Lambda K_S^0(\bar{\Lambda} K_S^0)$ Fits with No Residuals	47
26	$\Lambda K_S^0(\bar{\Lambda} K_S^0)$ Fits with No Residuals (Wide Range)	48
27	$\Lambda K^+(\bar{\Lambda} K^-)$ Fits, with NO residual correlations included, with No Residuals	49
28	$\Lambda K^+(\bar{\Lambda} K^-)$ Fits with No Residuals (Wide Range)	50
29	$\Lambda K^-(\bar{\Lambda} K^+)$ Fits with No Residuals	51
30	$\Lambda K^-(\bar{\Lambda} K^+)$ Fits with No Residuals (Wide Range)	52
31	$m_T$ Scaling of Radii: No Residuals in Fit	55
32	$\Lambda K_S^0(\bar{\Lambda} K_S^0)$ Fits with 3 Residuals	56

33	Small Caption . . . . .	57
34	$\Lambda K^+(\bar{\Lambda}K^-)$ Fits with 3 Residuals . . . . .	58
35	Small Caption . . . . .	59
36	$\Lambda K^-(\bar{\Lambda}K^+)$ Fits with 3 Residuals . . . . .	60
37	Small Caption . . . . .	61
38	$m_T$ Scaling of Radii: 3 Residuals in Fit . . . . .	65
39	$\Lambda K_S^0(\bar{\Lambda}K_S^0)$ Fits with 10 Residuals . . . . .	66
40	Small Caption . . . . .	67
41	$\Lambda K^+(\bar{\Lambda}K^-)$ Fits with 10 Residuals . . . . .	68
42	Small Caption . . . . .	69
43	$\Lambda K^-(\bar{\Lambda}K^+)$ Fits with 10 Residuals . . . . .	70
44	Small Caption . . . . .	71
45	$m_T$ Scaling of Radii: 10 Residuals in Fit . . . . .	75
46	$\Xi K^\pm$ Results . . . . .	76
47	$\Xi K^\pm$ Data with Coulomb-Only Bands, 0-10% Centrality . . . . .	77
48	Effect of Strong Force Inclusion on Coulomb-Only Curve for $\Xi K^\pm$ systems . . . . .	78
49	$\Xi K^\pm$ Global Coulomb-Only Fit (Set 1) . . . . .	79
50	$\Xi K^\pm$ Global Coulomb-Only Fit (Set 2) . . . . .	80
51	$\Xi^- K^+$ Coulomb-Only Fit . . . . .	80
52	$\Xi^- K^-$ Coulomb-Only Fit . . . . .	81
53	Residuals: $\Sigma^0 K^+$ to $\Lambda K^+$ (0-10% Centrality) . . . . .	82
54	Residuals: $\Xi^0 K^+$ to $\Lambda K^+$ (0-10% Centrality) . . . . .	83
55	Residuals: $\Xi^- K^+$ to $\Lambda K^+$ (0-10% Centrality) . . . . .	83
56	Residuals: $\Sigma^{*+} K^+$ to $\Lambda K^+$ (0-10% Centrality) . . . . .	84
57	Residuals: $\Sigma^{*-} K^+$ to $\Lambda K^+$ (0-10% Centrality) . . . . .	84
58	Residuals: $\Sigma^{*0} K^+$ to $\Lambda K^+$ (0-10% Centrality) . . . . .	85
59	Residuals: $\Lambda K^{*0}$ to $\Lambda K^+$ (0-10% Centrality) . . . . .	85
60	Residuals: $\Sigma^0 K^{*0}$ to $\Lambda K^+$ (0-10% Centrality) . . . . .	86
61	Residuals: $\Xi^0 K^{*0}$ to $\Lambda K^+$ (0-10% Centrality) . . . . .	86
62	Residuals: $\Xi^- K^{*0}$ to $\Lambda K^+$ (0-10% Centrality) . . . . .	87
63	Residuals: $\Sigma^0 K^-$ to $\Lambda K^-$ (0-10% Centrality) . . . . .	88
64	Residuals: $\Xi^0 K^-$ to $\Lambda K^-$ (0-10% Centrality) . . . . .	89
65	Residuals: $\Xi^- K^-$ to $\Lambda K^-$ (0-10% Centrality) . . . . .	89

66	Residuals: $\Sigma^{*+}K^-$ to $\Lambda K^-$ (0-10% Centrality) . . . . .	90
67	Residuals: $\Sigma^{*-}K^-$ to $\Lambda K^-$ (0-10% Centrality) . . . . .	90
68	Residuals: $\Sigma^{*0}K^-$ to $\Lambda K^-$ (0-10% Centrality) . . . . .	91
69	Residuals: $\Lambda\bar{K}^{*0}$ to $\Lambda K^-$ (0-10% Centrality) . . . . .	91
70	Residuals: $\Sigma^0\bar{K}^{*0}$ to $\Lambda K^-$ (0-10% Centrality) . . . . .	92
71	Residuals: $\Xi^0\bar{K}^{*0}$ to $\Lambda K^-$ (0-10% Centrality) . . . . .	92
72	Residuals: $\Xi^-\bar{K}^{*0}$ to $\Lambda K^-$ (0-10% Centrality) . . . . .	93
73	Residuals: $\Sigma^0K_S^0$ to $\Lambda K_S^0$ (0-10% Centrality) . . . . .	94
74	Residuals: $\Xi^0K_S^0$ to $\Lambda K_S^0$ (0-10% Centrality) . . . . .	95
75	Residuals: $\Xi^-K_S^0$ to $\Lambda K_S^0$ (0-10% Centrality) . . . . .	95
76	Residuals: $\Sigma^{*+}K_S^0$ to $\Lambda K_S^0$ (0-10% Centrality) . . . . .	96
77	Residuals: $\Sigma^{*-}K_S^0$ to $\Lambda K_S^0$ (0-10% Centrality) . . . . .	96
78	Residuals: $\Sigma^{*0}K_S^0$ to $\Lambda K_S^0$ (0-10% Centrality) . . . . .	97
79	Residuals: $\Lambda K^{*0}$ to $\Lambda K_S^0$ (0-10% Centrality) . . . . .	97
80	Residuals: $\Sigma^0K^{*0}$ to $\Lambda K_S^0$ (0-10% Centrality) . . . . .	98
81	Residuals: $\Xi^0K^{*0}$ to $\Lambda K_S^0$ (0-10% Centrality) . . . . .	98
82	Residuals: $\Xi^-K^{*0}$ to $\Lambda K_S^0$ (0-10% Centrality) . . . . .	99

---

## 12 1 Introduction

13 We present results from a femtoscopic analysis of Lambda-Kaon correlations in Pb-Pb collisions at  $\sqrt{s_{NN}}$   
 14 = 2.76 TeV by the ALICE experiment at the LHC. All pair combinations of  $\Lambda$  and  $\bar{\Lambda}$  with  $K^+$ ,  $K^-$  and  
 15  $K_S^0$  are analyzed. The femtoscopic correlations are the result of strong final-state interactions, and are  
 16 fit with a parametrization based on a model by R. Lednicky and V. L. Lyuboshitz [1]. This allows us to  
 17 both characterize the emission source and measure the scattering parameters for the particle pairs. We  
 18 observe a large difference in the  $\Lambda$ - $K^+$  ( $\bar{\Lambda}$ - $K^-$ ) and  $\Lambda$ - $K^-$  ( $\bar{\Lambda}$ - $K^+$ ) correlations in pairs with low relative  
 19 momenta ( $k^* \lesssim 100$  MeV). Additionally, the average of the  $\Lambda$ - $K^+$  ( $\bar{\Lambda}$ - $K^-$ ) and  $\Lambda$ - $K^-$  ( $\bar{\Lambda}$ - $K^+$ ) correlation  
 20 functions is consistent with our  $\Lambda$ - $K_S^0$  ( $\bar{\Lambda}$ - $K_S^0$ ) measurement. The results suggest an effect arising from  
 21 different quark-antiquark interactions in the pairs, i.e.  $s\bar{s}$  in  $\Lambda$ - $K^+$  ( $\bar{\Lambda}$ - $K^-$ ) and  $u\bar{u}$  in  $\Lambda$ - $K^-$  ( $\bar{\Lambda}$ - $K^+$ ). To  
 22 gain further insight into this hypothesis, we currently are conducting a  $\Xi$ -K femtoscopic analysis.

## 23 2 Data Sample and Software

### 24 2.1 Data Sample

25 The analysis used “pass 2” reconstructed Pb-Pb data from LHC11h (AOD145). The runlist was selected  
 26 from runs with global quality tag “1” in the ALICE Run Condition Table. Approximately 40 million  
 27 combined central, semi-central, and minimum bias events were analyzed. Runs from both positive (++)  
 28 and negative (--) magnetic field polarity settings were used.

29 Run list: 170593, 170572, 170388, 170387, 170315, 170313, 170312, 170311, 170309, 170308, 170306,  
 30 170270, 170269, 170268, 170230, 170228, 170207, 170204, 170203, 170193, 170163, 170159, 170155,  
 31 170091, 170089, 170088, 170085, 170084, 170083, 170081, 170040, 170027, 169965, 169923, 169859,  
 32 169858, 169855, 169846, 169838, 169837, 169835, 169591, 169590, 169588, 169587, 169586, 169557,  
 33 169555, 169554, 169553, 169550, 169515, 169512, 169506, 169504, 169498, 169475, 169420, 169419,  
 34 169418, 169417, 169415, 169411, 169238, 169167, 169160, 169156, 169148, 169145, 169144, 169138,  
 35 169099, 169094, 169091, 169045, 169044, 169040, 169035, 168992, 168988, 168826, 168777, 168514,  
 36 168512, 168511, 168467, 168464, 168460, 168458, 168362, 168361, 168342, 168341, 168325, 168322,  
 37 168311, 168310, 168315, 168108, 168107, 168105, 168076, 168069, 167988, 167987, 167985, 167920,  
 38 167915

39 Analysis was also performed on the LHC12a17a\_fix (AOD149) Monte Carlo HIJING events for certain  
 40 checks. THERMINATOR2 was also used for certain aspects, such as transform matrices described feed-  
 41 down contributions.

### 42 2.2 Software

43 The analysis was performed on the PWGCF analysis train using AliRoot v5-08-18-1 and AliPhysics  
 44 vAN-20161027-1.

45 The main classes utilized include: AliFemtoVertexMultAnalysis, AliFemtoEventCutEstimators, AliFem-  
 46 toESDTrackCutNSigmaFilter, AliFemtoV0TrackCutNSigmaFilter, AliFemtoXiTrackCut, AliFemtoV0PairCut,  
 47 AliFemtoV0TrackPairCut, AliFemtoXiTrackPairCut, and AliFemtoAnalysisLambdaKaon. All of these  
 48 classes are contained in /AliPhysics/PWGCF/FEMTOSCOPY/AliFemto and .../AliFemtoUser.

## 49 3 Data Selection

### 50 3.1 Event Selection and Mixing

51 The events used in this study were selected with the class AliFemtoEventCutEstimators according to the  
 52 following criteria:

- 53        – Triggers
- 54            – minimum bias (kMB)
- 55            – central (kCentral)
- 56            – semi-central (kSemiCentral)
- 57        – z-position of reconstructed event vertex must be within 10 cm of the center of the ALICE detector
- 58        – the event must contain at least one particle of each type from the pair of interest
- 59     The event mixing was handled by the AliFemtoVertexMultAnalysis class, which only mixes events with
- 60     like vertex position and centrality. The following criteria were used for event mixing:
- 61            – Number of events to mix = 5
- 62            – Vertex position bin width = 2 cm
- 63            – Centrality bin width = 5
- 64     The AliFemtoEventReaderAODChain class is used to read the events. Event flattening is not currently
- 65     used. FilterBit(7). The centrality is determined by the “V0M” method of AliCentrality, set by calling Al-
- 66     iFemtoEventReaderAOD::SetUseMultiplicity(kCentrality). I utilize the SetPrimaryVertexCorrectionT-
- 67     PCPoints switch, which causes the reader to shift all TPC points to be relative to the event vertex.
- 68     **3.2 K<sup>±</sup> Track Selection**
- 69     Charged kaons are identified using the AliFemtoESDTrackCutNSigmaFilter class. The specific cuts used
- 70     in this analysis are as follows:
- 71     Track Selection:
- 72            – Kinematic range:
- 73                  –  $0.14 < p_T < 1.5 \text{ GeV}/c$
- 74                  –  $|\eta| < 0.8$
- 75            – FilterBit(7)
- 76                  – TPC tracks
- 77            – Track Quality
- 78                  – Minimum number of clusters in the TPC (fminTPCncls) = 80
- 79                  – Maximum allowed  $\chi^2/N_{DOF}$  for ITS clusters = 3.0
- 80                  – Maximum allowed  $\chi^2/N_{DOF}$  for TPC clusters = 4.0
- 81            – Primary Particle Selection:
- 82                  – Maximum XY impact parameter = 2.4 cm
- 83                  – Maximum Z impact parameter = 3.0 cm
- 84            – Remove particles with any kink labels (fRemoveKinks = true)
- 85            – Maximum allowed sigma to primary vertex (fMaxSigmaToVertex) = 3.0

86 K $^\pm$  Identification:

87 – PID Probabilities:

- 88 – K: > 0.2
- 89 –  $\pi$ : < 0.1
- 90 –  $\mu$ : < 0.8
- 91 – p: < 0.1

92 – Most probable particle type must be Kaon (fMostProbable=3)

93 – TPC and TOF N $_\sigma$  cuts:

- 94 –  $p < 0.4 \text{ GeV}/c$ : N $_{\sigma K, \text{TPC}} < 2$
- 95 –  $0.4 < p < 0.45 \text{ GeV}/c$ : N $_{\sigma K, \text{TPC}} < 1$
- 96 –  $0.45 < p < 0.8 \text{ GeV}/c$ : N $_{\sigma K, \text{TPC}} < 3 \& N_{\sigma K, \text{TOF}} < 2$
- 97 –  $0.8 < p < 1.0 \text{ GeV}/c$ : N $_{\sigma K, \text{TPC}} < 3 \& N_{\sigma K, \text{TOF}} < 1.5$
- 98 –  $p > 1.0 \text{ GeV}/c$ : N $_{\sigma K, \text{TPC}} < 3 \& N_{\sigma K, \text{TOF}} < 1$

99 – Electron Rejection: Reject if N $_{\sigma e^-, \text{TPC}} < 3$

100 – Pion Rejection: Reject if:

- 101 –  $p < 0.65 \text{ GeV}/c$ 
  - 102 \* if TOF and TPC available: N $_{\sigma \pi, \text{TPC}} < 3 \& N_{\sigma \pi, \text{TOF}} < 3$
  - 103 \* else
    - 104 ·  $p < 0.5 \text{ GeV}/c$ : N $_{\sigma \pi, \text{TPC}} < 3$
    - 105 ·  $0.5 < p < 0.65 \text{ GeV}/c$ : N $_{\sigma \pi, \text{TPC}} < 2$
- 106 –  $0.65 < p < 1.5 \text{ GeV}/c$ : N $_{\sigma \pi, \text{TPC}} < 5 \& N_{\sigma \pi, \text{TOF}} < 3$
- 107 –  $p > 1.5 \text{ GeV}/c$ : N $_{\sigma \pi, \text{TPC}} < 5 \& N_{\sigma \pi, \text{TOF}} < 2$

108 The purity of the K $^\pm$  collections was estimated using the MC data, for which the true identity of each  
109 reconstructed K $^\pm$  particle is known. Therefore, the purity may be estimated as:

$$\text{Purity}(K^\pm) = \frac{N_{\text{true}}}{N_{\text{reconstructed}}} \quad (1)$$

110 Purity(K $^+$ )  $\approx$  Purity(K $^-$ )  $\approx$  97%

### 111 3.3 V0 Selection

112  $\Lambda$  ( $\bar{\Lambda}$ ) and K $_S^0$  are neutral particles which cannot be directly detected, but must instead be reconstructed  
113 through detection of their decay products, or daughters. This process is illustrated in Figure 1. In  
114 general, particles which are topologically reconstructed in this fashion are called V0 particles. The  
115 class AliFemtoV0TrackCutNSigmaFilter (which is an extension of AliFemtoV0TrackCut) is used to  
116 reconstruct the V0s.

117 In order to obtain a true and reliable signal, one must ensure good purity of the V0 collection. The purity  
118 of the collection is calculated as:

$$\text{Purity} = \frac{\text{Signal}}{\text{Signal} + \text{Background}} \quad (2)$$

To obtain both the signal and background, the invariant mass distribution ( $m_{inv}$ ) of all V0 candidates must be constructed immediately before the final invariant mass cut. Examples of such distributions can be found in Figures 3 and 5. It is vital that this distribution be constructed immediately before the final  $m_{inv}$  cut, otherwise it would be impossible to estimate the background. As shown in Figures 3 and 5, the background is fit (with a polynomial) outside of the peak region of interest to obtain an estimate for the background within the region. Within the  $m_{inv}$  cut limits, the background is the region below the fit while the signal is the region above the fit.

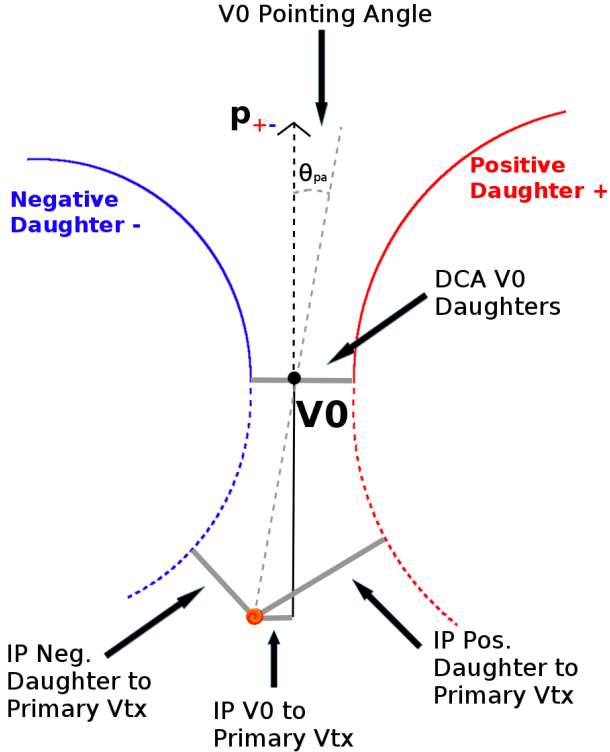


**Fig. 1:** V0 Reconstruction

### 3.3.1 $\Lambda$ Reconstruction

The following cuts were used to select good  $\Lambda$  ( $\bar{\Lambda}$ ) candidates:

#### 1. Daughter Particle Cuts

##### (a) Cuts Common to Both Daughters

- i.  $|\eta| < 0.8$
- ii. SetTPCnclsDaughters(80)
- iii. SetStatusDaughters(AliESDtrack::kTPCrefit)
- iv. DCA  $\pi p$  Daughters  $< 0.4$  cm

##### (b) Pion Specific Daughter Cuts

- i.  $p_T > 0.16$  GeV/c
- ii. DCA to prim vertex  $> 0.3$  cm
- iii. TPC and TOF N $\sigma$  Cuts
  - A.  $p < 0.5$  GeV/c : N $\sigma_{TPC} < 3$
  - B.  $p > 0.5$  GeV/c :

- if TOF & TPC available:  $N\sigma_{\text{TPC}} < 3$  &  $N\sigma_{\text{TOF}} < 3$
- else  $N\sigma_{\text{TOF}} < 3$

142 (c) Proton Specific Daughter Cuts

- i.  $p_T > 0.5(p)[0.3(\bar{p})] \text{ GeV}/c$
- ii. DCA to prim vertex  $> 0.1 \text{ cm}$
- iii. TPC and TOF  $N\sigma$  Cuts
  - A.  $p < 0.8 \text{ GeV}/c : N\sigma_{\text{TPC}} < 3$
  - B.  $p > 0.8 \text{ GeV}/c :$ 
    - if TOF & TPC available:  $N\sigma_{\text{TPC}} < 3$  &  $N\sigma_{\text{TOF}} < 3$
    - else  $N\sigma_{\text{TOF}} < 3$

150 2. V0 Cuts

- (a)  $|\eta| < 0.8$
- (b)  $p_T > 0.4 \text{ GeV}/c$
- (c)  $|m_{\text{inv}} - m_{\text{PDG}}| < 3.8 \text{ MeV}$
- (d) DCA to prim. vertex  $< 0.5 \text{ cm}$
- (e) Cosine of pointing angle  $> 0.9993$
- (f) OnFlyStatus = false
- (g) Decay Length  $< 60 \text{ cm}$

155 3. Shared Daughter Cut for V0 Collection

- Iterate through V0 collection to ensure that no daughter is used in more than one V0 candidate

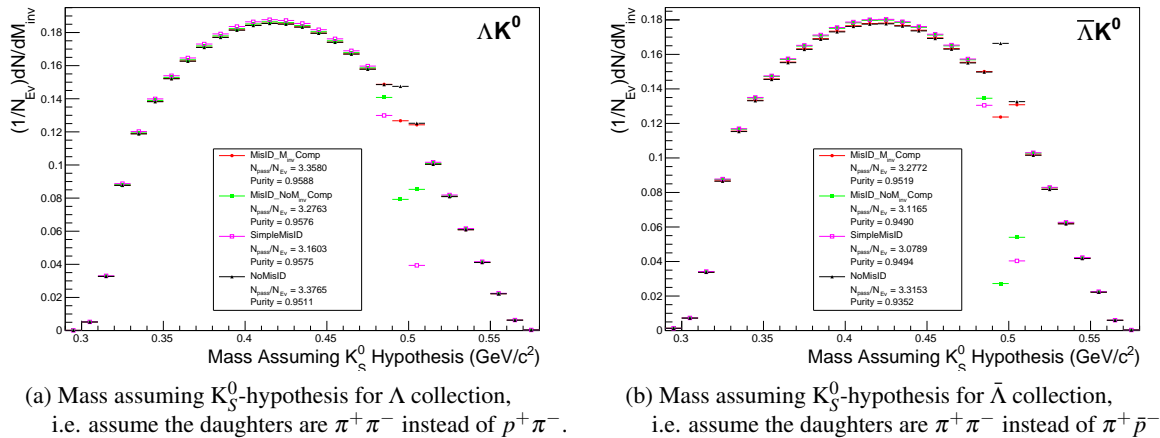


**Fig. 2:** Mass assuming  $K_S^0$ -hypothesis for V0 candidates passing all  $\Lambda$  (2a) and  $\bar{\Lambda}$  (2b) cuts. The “NoMisID” distribution (black triangles) uses the V0 finder without any attempt to remove misidentified  $K_S^0$ . The slight peak in the “NoMisID” distribution around  $m_{\text{inv}} = 0.5 \text{ GeV}/c^2$  contains misidentified  $K_S^0$  particles in our  $\Lambda(\bar{\Lambda})$  collection. “SimpleMisID” (pink squares) simply cuts out the entire peak, which throws away some good  $\Lambda$  and  $\bar{\Lambda}$  particles. “MisID\_NoM<sub>inv</sub>Comp” (green squares) uses the misidentification cut outlined in the text, but does not utilize the invariant mass comparison method. “MisID\_M<sub>inv</sub>Comp” (red circles) utilizes the full misidentification methods, and is currently used for this analysis. “ $N_{\text{pass}}/N_{\text{ev}}$ ” is the total number of  $\Lambda(\bar{\Lambda})$  particles found, normalized by the total number of events. The purity of the collection is also listed.

Figure 2a shows the mass assuming  $K_S^0$  hypothesis for the  $\Lambda$  collection, i.e. assume the daughters are  $\pi^+\pi^-$  instead of  $\pi^+\bar{p}$ . Figure 2b is a similar plot, but is for the  $\bar{\Lambda}$  collection, i.e. assume the daughters are  $\pi^+\pi^-$  instead of  $\pi^+\bar{p}$ . The  $K_S^0$  contamination is visible, although not profound, in both in the slight peaks around  $m_{\text{inv}} = 0.497 \text{ GeV}/c^2$ . If one simply cuts out the entire peak, good  $\Lambda$  particles will be lost. Ideally, the  $\Lambda$  selection and  $K_S^0$  misidentification cuts are selected such that the peak is removed from this plot while leaving the distribution continuous. To attempt to remove these  $K_S^0$  contaminations without throwing away good  $\Lambda$  and  $\bar{\Lambda}$  particles, the following misidentification cuts are imposed; a  $\Lambda(\bar{\Lambda})$  candidate is rejected if all of the following criteria are satisfied:

- $|m_{\text{inv}, K_S^0 \text{ Hypothesis}} - m_{\text{PDG}, K_S^0}| < 9.0 \text{ MeV}/c^2$
- Positive and negative daughters pass  $\pi$  daughter cut implemented for  $K_S^0$  reconstruction
- $|m_{\text{inv}, K_S^0 \text{ Hypothesis}} - m_{\text{PDG}, K_S^0}| < |m_{\text{inv}, \Lambda(\bar{\Lambda}) \text{ Hypothesis}} - m_{\text{PDG}, \Lambda(\bar{\Lambda})}|$

Figure 3 shows the invariant mass ( $m_{\text{inv}}$ ) distribution of all  $\Lambda(\bar{\Lambda})$  candidates immediately before the final invariant mass cut. These distributions are used to calculate the collection purities. The  $\Lambda$  and  $\bar{\Lambda}$  purities are found to be:  $\text{Purity}(\Lambda) \approx \text{Purity}(\bar{\Lambda}) \approx 95\%$ .

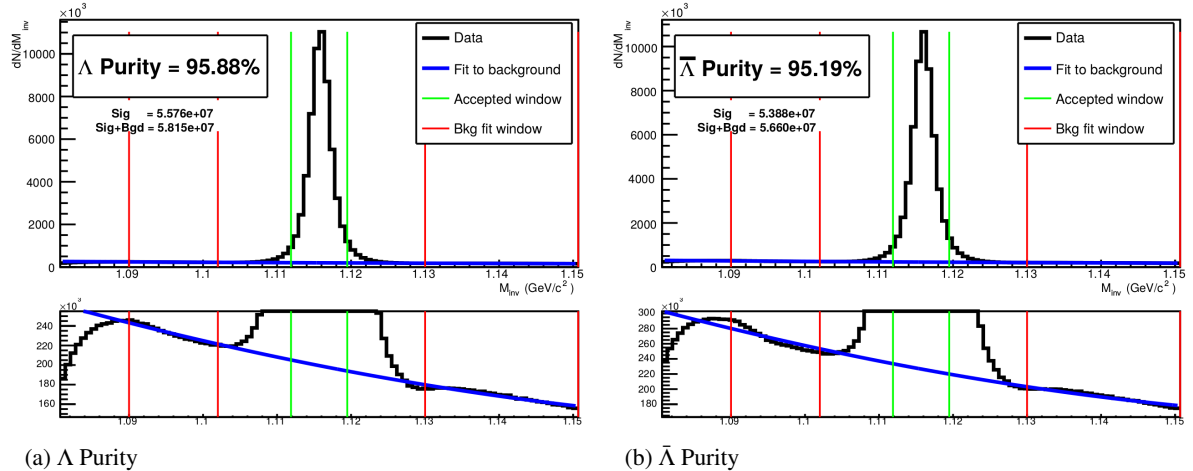


**Fig. 3:** Invariant mass ( $m_{\text{inv}}$ ) distribution of all  $\Lambda$  (a) and  $\bar{\Lambda}$  (b) candidates immediately before the final invariant mass cut. The bottom figures are zoomed to show the background with fit. The vertical green lines represent the  $m_{\text{inv}}$  cuts used in the analyses, the red vertical lines delineate the region over which the background was fit, and the blue line shows the background fit. These distributions are used to calculate the collection purities,  $\text{Purity}(\Lambda) \approx \text{Purity}(\bar{\Lambda}) \approx 95\%$ .

### 3.3.2 $K_S^0$ Reconstruction

The following cuts were used to select good  $K_S^0$  candidates:

#### 1. Pion Daughter Cuts

- (a)  $|\eta| < 0.8$
- (b) SetTPCnclsDaughters(80)
- (c) SetStatusDaughters(AliESDtrack::kTPCrefic)
- (d) DCA  $\pi^+\pi^-$  Daughters  $< 0.3 \text{ cm}$

- 181 (e)  $p_T > 0.15 \text{ GeV}/c$
- 182 (f) DCA to prim vertex  $> 0.3 \text{ cm}$
- 183 (g) TPC and TOF N $\sigma$  Cuts
  - 184 i.  $p < 0.5 \text{ GeV}/c : \text{N}\sigma_{\text{TPC}} < 3$
  - 185 ii.  $p > 0.5 \text{ GeV}/c :$ 
    - 186 – if TOF & TPC available:  $\text{N}\sigma_{\text{TPC}} < 3 \& \text{N}\sigma_{\text{TOF}} < 3$
    - 187 – else  $\text{N}\sigma_{\text{TOF}} < 3$

## 188 2. $K_S^0$ Cuts

- 189 (a)  $|\eta| < 0.8$
- 190 (b)  $p_T > 0.2 \text{ GeV}/c$
- 191 (c)  $m_{\text{PDG}} - 13.677 \text{ MeV} < m_{\text{inv}} < m_{\text{PDG}} + 2.0323 \text{ MeV}$
- 192 (d) DCA to prim. vertex  $< 0.3 \text{ cm}$
- 193 (e) Cosine of pointing angle  $> 0.9993$
- 194 (f) OnFlyStatus = false
- 195 (g) Decay Length  $< 30 \text{ cm}$

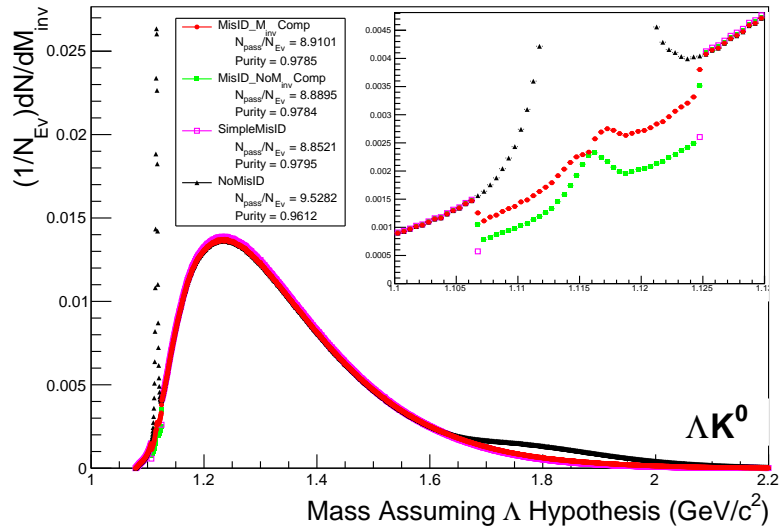
## 196 3. Shared Daughter Cut for V0 Collection

- 197 – Iterate through V0 collection to ensure that no daughter is used in more than one V0 candidate

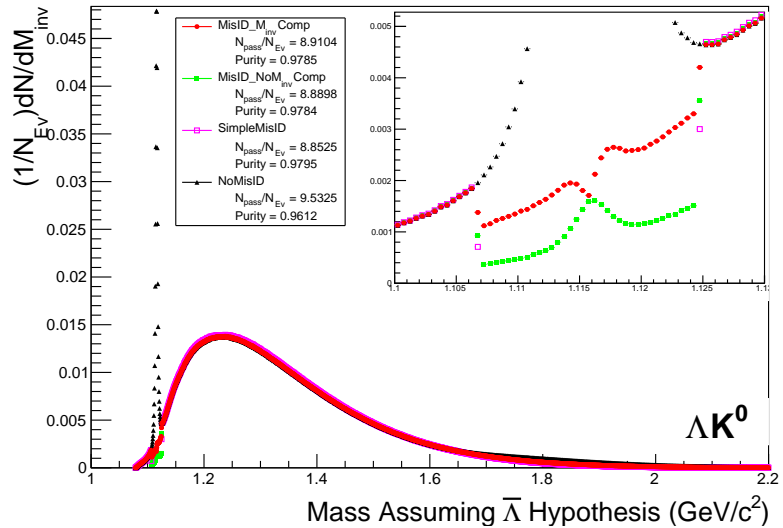
198 As can be seen in Figure 4, some misidentified  $\Lambda$  and  $\bar{\Lambda}$  particles contaminate our  $K_S^0$  sample. Figure  
 199 4a shows the mass assuming  $\Lambda$ -hypothesis for the  $K_S^0$  collection, i.e. assume the daughters are  $p^+\pi^-$   
 200 instead of  $\pi^+\pi^-$ . Figure 4b is similar, but shows the mass assuming  $\bar{\Lambda}$  hypothesis for the collection,  
 201 i.e. assume the daughters are  $\pi^+\bar{p}^-$  instead of  $\pi^+\pi^-$ . The  $\Lambda$  contamination can be seen in 4a, and the  
 202  $\bar{\Lambda}$  contamination in 4b, in the peaks around  $m_{\text{inv}} = 1.115 \text{ GeV}/c^2$ . Additionally, the  $\bar{\Lambda}$  contamination is  
 203 visible in Figure 4a, and the  $\Lambda$  contamination visible in Figure 4b, in the region of excess around  $1.65$   
 204  $< m_{\text{inv}} < 2.1 \text{ GeV}/c^2$ . This is confirmed as the number of misidentified  $\Lambda$  particles in the sharp peak  
 205 of Figure 4a (misidentified  $\bar{\Lambda}$  particles in the sharp peak of Figure 4b) approximately equals the excess  
 206 found in the  $1.65 < m_{\text{inv}} < 2.1 \text{ GeV}/c^2$  region of Figure 4a (Figure 4b).

207 The peaks around  $m_{\text{inv}} = 1.115 \text{ GeV}/c^2$  in Figure 4 contain both misidentified  $\Lambda$  ( $\bar{\Lambda}$ ) particles and good  
 208  $K_S^0$ . If one simply cuts out the entire peak, some good  $K_S^0$  particles will be lost. Ideally, the  $K_S^0$  selection  
 209 and  $\Lambda(\bar{\Lambda})$  misidentification cuts can be selected such that the peak is removed from this plot while leaving  
 210 the distribution continuous. To attempt to remove these  $\Lambda$  and  $\bar{\Lambda}$  contaminations without throwing away  
 211 good  $K_S^0$  particles, the following misidentification cuts are imposed; a  $K_S^0$  candidate is rejected if all of  
 212 the following criteria are satisfied (for either  $\Lambda$  or  $\bar{\Lambda}$  hypothesis):

- 213 –  $|m_{\text{inv}, \Lambda(\bar{\Lambda}) \text{ Hypothesis}} - m_{\text{PDG}, \Lambda(\bar{\Lambda})}| < 9.0 \text{ MeV}/c^2$
- 214 – Positive daughter passes  $p^+(\pi^+)$  daughter cut implemented for  $\Lambda(\bar{\Lambda})$  reconstruction
- 215 – Negative daughter passes  $\pi^-(\bar{p}^-)$  daughter cut implemented by  $\Lambda(\bar{\Lambda})$  reconstruction
- 216 –  $|m_{\text{inv}, \Lambda(\bar{\Lambda}) \text{ Hypothesis}} - m_{\text{PDG}, \Lambda(\bar{\Lambda})}| < |m_{\text{inv}, K_S^0 \text{ Hypothesis}} - m_{\text{PDG}, K_S^0}|$



(a) Mass assuming  $\Lambda$ -hypothesis for  $K_S^0$  collection, i.e. assume the daughters are  $p^+ \pi^-$  instead of  $\pi^+ \pi^-$ .



(b) Mass assuming  $\bar{\Lambda}$ -hypothesis for  $K_S^0$  collection, i.e. assume the daughters are  $\pi^+ \bar{p}^-$  instead of  $\pi^+ \pi^-$ .

**Fig. 4:** Mass assuming  $\Lambda$ -hypothesis (4a) and  $\bar{\Lambda}$ -hypothesis (4b) for  $K_S^0$  collection. The “NoMisID” distribution (black triangles) uses the V0 finder without any attempt to remove misidentified  $\Lambda$  and  $\bar{\Lambda}$ . The peak in the “NoMisID” distribution around  $m_{\text{inv}} = 1.115 \text{ GeV}/c^2$  contains misidentified  $\Lambda$  (4a) and  $\bar{\Lambda}$  (4b) particles in our  $K_S^0$  collection. “SimpleMisID” (pink squares) simply cuts out the entire peak, which throws away some good  $K_S^0$  particles. “MisID\_NoM<sub>inv</sub>Comp” (green squares) uses the misidentification cut outlined in the text, but does not utilize the invariant mass comparison method. “MisID\_M<sub>inv</sub>Comp” (red circles) utilizes the full misidentification methods, and is currently used for this analysis. “ $N_{\text{pass}}/N_{\text{ev}}$ ” is the total number of  $K_S^0$  particles found, normalized by the total number of events. The purity of the collection is also listed. Also note, the relative excess of the “NoMisID” distribution around  $1.65 < m_{\text{inv}} < 2.1 \text{ GeV}/c^2$  shows misidentified  $\bar{\Lambda}$  (4a) and  $\Lambda$  (4b) particles in our  $K_S^0$  collection.

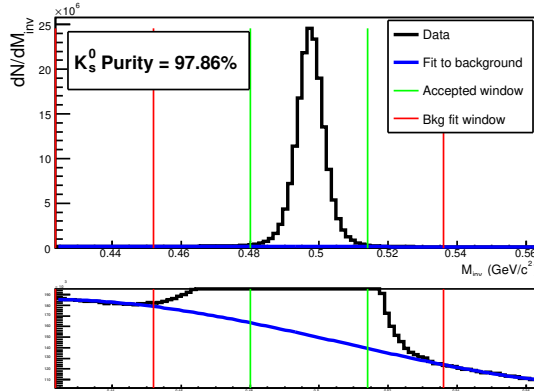


**Fig. 5:** Invariant mass ( $m_{inv}$ ) distribution of all  $K_s^0$  candidates immediately before the final invariant mass cut. The bottom figure is zoomed to show the background with fit. The vertical green lines represent the  $m_{inv}$  cut used in the analyses, the red vertical lines delineate the region over which the background was fit, and the blue line shows the background fit. This distribution is used to calculate the collection purity,  $Purity(K_s^0) \approx 98\%$ .

### 217 3.4 Cascade Reconstruction

218 Our motivation for studying  $\Xi K^\pm$  systems is to hopefully better understand the striking difference in the  
219  $\Lambda K^+$  and  $\Lambda K^-$  data at low  $k^*$  (Figure 14).

220 The reconstruction of  $\Xi$  particles is one step above V0 reconstruction. V0 particles are topologically  
221 reconstructed by searching for the charged daughters' tracks into which they decay. With  $\Xi$  particles, we  
222 search for the V0 particle and charged daughter into which the  $\Xi$  decays. In the case of  $\Xi^-$ , we search  
223 for the  $\Lambda$  (V0) and  $\pi^-$  (track) daughters. We will refer to this  $\pi$  as the “bachelor  $\pi$ ”.

224 The following cuts were used to select good  $\Xi^-$  ( $\bar{\Xi}^+$ ) candidates:

225 1. V0 Daughter Reconstruction

226 (a) V0 Daughter Particle Cuts

227 i. Cuts Common to Both Daughters

- 228 A.  $|\eta| < 0.8$
- 229 B. SetTPCnclsDaughters(80)
- 230 C. SetStatusDaughters(AliESDtrack::kTPCrefic)
- 231 D. SetMaxDcaV0Daughters(0.4)

232 ii. Pion Specific Daughter Cuts

- 233 A.  $p_T > 0.16$
- 234 B. DCA to prim vertex  $> 0.3$

235 iii. Proton Specific Daughter Cuts

- 236 A.  $p_T > 0.5(p) [0.3(\bar{p})] \text{ GeV}/c$

- 237 B. DCA to prim vertex  $> 0.1$

238 (b) V0 Cuts

- 239 i.  $|\eta| < 0.8$

- 240 ii.  $p_T > 0.4 \text{ GeV}/c$

- 241 iii.  $|m_{inv} - m_{PDG}| < 3.8 \text{ MeV}$

- 242 iv. DCA to prim. vertex  $> 0.2 \text{ cm}$

- 243 v. Cosine of pointing angle to  $\Xi$  decay vertex  $> 0.9993$

```

244     vi. OnFlyStatus = false
245     vii. Decay Length < 60 cm
246     viii. The misidentification cuts described in Section 3.3.1 are utilized
247 2. Bachelor  $\pi$  Cuts
248     (a)  $|\eta| < 0.8$ 
249     (b)  $p_T < 100 \text{ GeV}/c$ 
250     (c) DCA to prim vertex  $> 0.1 \text{ cm}$ 
251     (d) SetTPCnclsDaughters(70)
252     (e) SetStatusDaughters(AliESDtrack::kTPCrefic)

253 3.  $\Xi$  Cuts
254     (a)  $|\eta| < 0.8$ 
255     (b)  $0.8 < p_T < 100 \text{ GeV}/c$ 
256     (c)  $|m_{inv} - m_{PDG}| < 3.0 \text{ MeV}$ 
257     (d) DCA to prim. vertex  $< 0.3 \text{ cm}$ 
258     (e) Cosine of pointing angle  $> 0.9992$ 

259 4. Shared Daughter Cut for  $\Xi$  Collection
260     – Iterate through  $\Xi$  collection to ensure that no daughter is used in more than one  $\Xi$  candidate

```

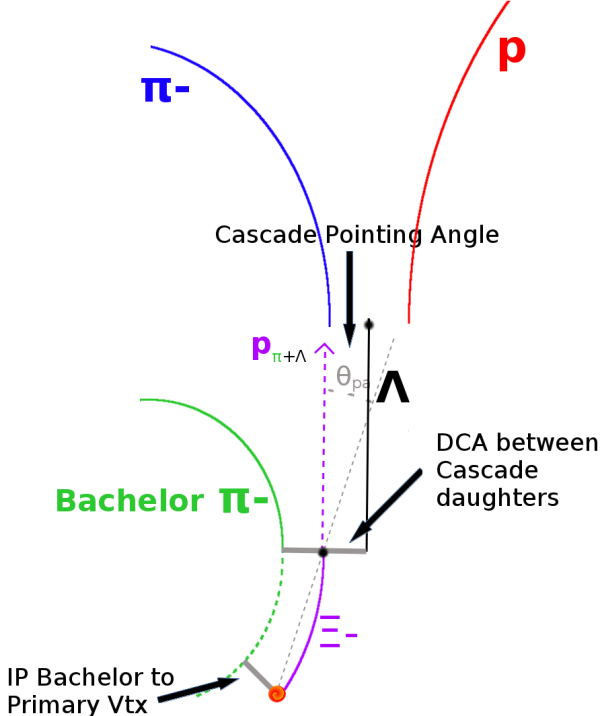


**Fig. 6:**  $\Xi$  Reconstruction

```

261 The purity of our  $\Xi$  and  $\bar{\Xi}$  collections are calculated just as those of our V0 collections 3.3. Figure 7,
262 which is used to calculate the purity, shows the  $m_{inv}$  distribution of our  $\Xi(\bar{\Xi})$  candidates just before the
263 final  $m_{inv}$  cut. Currently, we have Purity( $\Xi^-$ )  $\approx 90\%$  and Purity( $\bar{\Xi}^+$ )  $\approx 92\%$ .

```

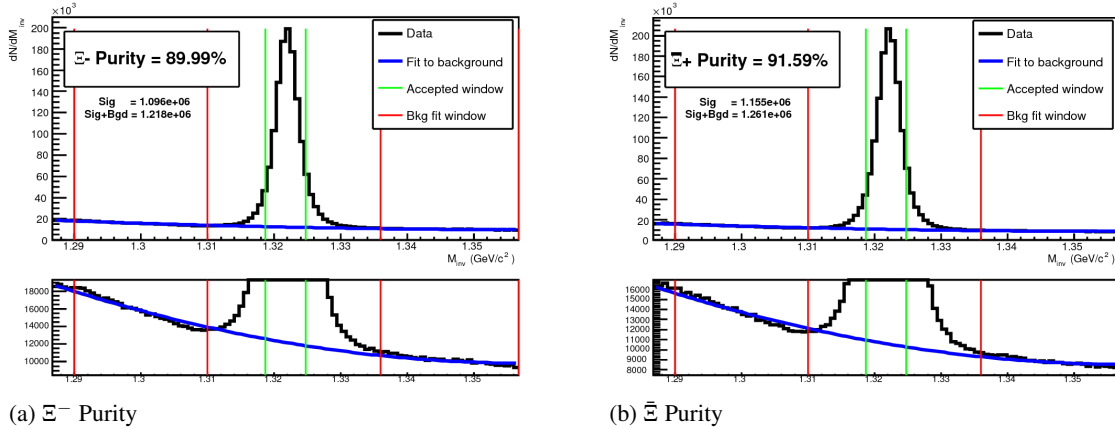


**Fig. 7:**  $\Xi^-$ - $(\bar{\Xi}^+)$  Purity 0-10%: Purity( $\Xi^-$ )  $\approx$  90% and Purity( $\bar{\Xi}^+$ )  $\approx$  92%.

### 3.5 Pair Selection

It is important to obtain true particle pairs in the analysis. In particular, contamination from pairs constructed with split or merged tracks, and pairs sharing daughters, can introduce an artificial signal into the correlation function, obscuring the actual physics.

#### 1. Shared Daughter Cut for Pairs

##### (a) V0-V0 Pairs (i.e. $\Lambda(\bar{\Lambda})K_S^0$ analyses)

- Remove all pairs which share a daughter
  - Ex.  $\Lambda$  and  $K_S^0$  particles which share a  $\pi^-$  daughter are not included

##### (b) V0-Track Pairs (i.e. $\Lambda(\bar{\Lambda})K^\pm$ analyses)

- Remove pairs if Track is also used as a daughter of the V0
  - In these analyses, this could only occur if, for instance, a  $K$  is misidentified as a  $\pi$  or  $p$  in the V0 reconstruction

##### (c) $\Xi$ -Track Pairs

- Remove pairs if Track is also used as a daughter of the  $\Xi$ 
  - In these analyses, this could only occur if, for instance, a  $K$  is misidentified as a  $\pi$  or  $p$  in the V0 reconstruction, or misidentified as bachelor  $\pi$ .
- Remove pair if bachelor  $\pi$  is also a daughter of the  $\Lambda$ 
  - This is not a pair cut, but is included here because this cut occurs in the AliFemtoXiTrackPairCut class

#### 2. Average Separation Cuts

- Used to cut out splitting and merging effects
- The motivation for these cuts can be seen in Figures 8, 9, and 10, in which average separation correlation functions are presented

##### (a) $\Lambda(\bar{\Lambda})K_S^0$ Analyses

- Average separation  $> 6.0$  cm for like charge sign daughters
  - ex.  $p$  daughter of  $\Lambda$  and  $\pi^+$  daughter of  $K_S^0$
  - No cut for unlike-sign daughters

291 (b)  $\Lambda(\bar{\Lambda})K^\pm$  Analyses

- 292 – Average Separation  $> 8.0$  cm for daughter of  $\Lambda(\bar{\Lambda})$  sharing charge sign of  $K^\pm$   
 293 – ex. in  $\Lambda K^+$  analysis,  $p$  daughter of  $\Lambda$  with  $K^+$   
 294 – No cut for unlike signs

295 (c)  $\Xi(\bar{\Xi})K^\pm$  Analyses

- 296 – Average Separation  $> 8.0$  cm for any daughter of  $\Xi$  sharing charge sign of  $K^\pm$   
 297 – ex. in  $\Xi^- K^-$  analysis,  $\pi^-$  daughter of  $\Lambda$  daughter with  $K^-$ , and bachelor  $\pi^-$  daugh-  
 298 ter with  $K^-$   
 299 – No cut for unlike signs

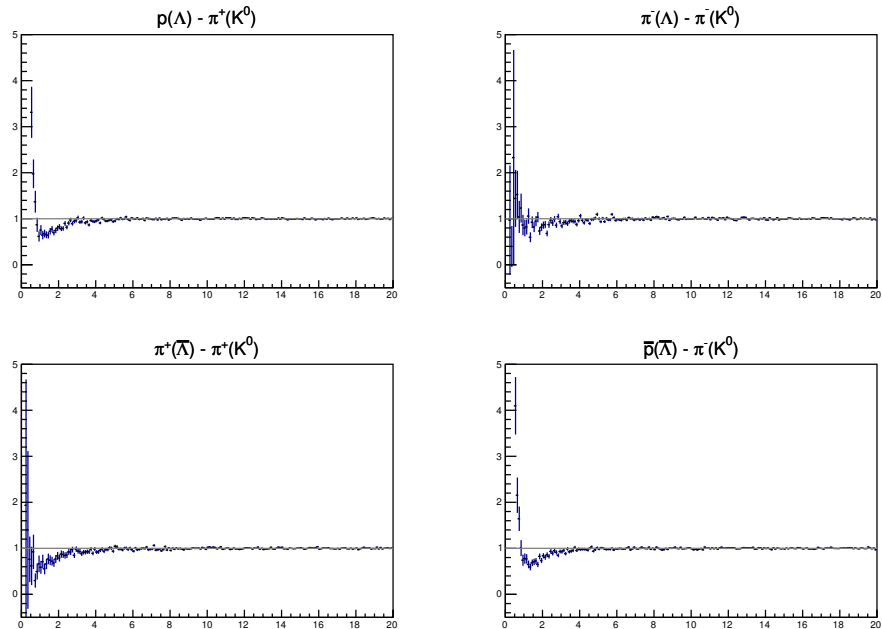


**Fig. 8:** Average separation (cm) correlation functions of  $\Lambda(\bar{\Lambda})$  and  $K_S^0$  Daughters. Only like-sign daughter pairs are shown (the distributions for unlike-signs were found to be flat). The title of each subfigure shows the daughter pair, as well as the mother of each daughter (in “()”), ex. top left is  $p$  from  $\Lambda$  with  $\pi^+$  from  $K_S^0$ .

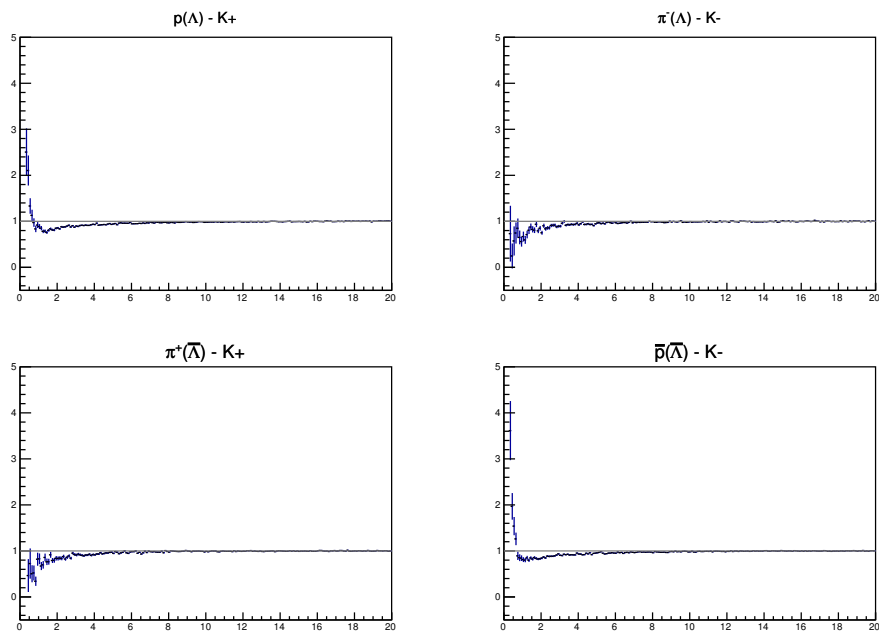


**Fig. 9:** Average separation (cm) correlation functions of  $\Lambda(\bar{\Lambda})$  Daughter and  $K^\pm$ . Only like-sign pairs are shown (unlike-signs were flat). In the subfigure titles, the particles in “( )” represent the mothers, ex. top left is  $p$  from  $\Lambda$  with  $K^+$ .

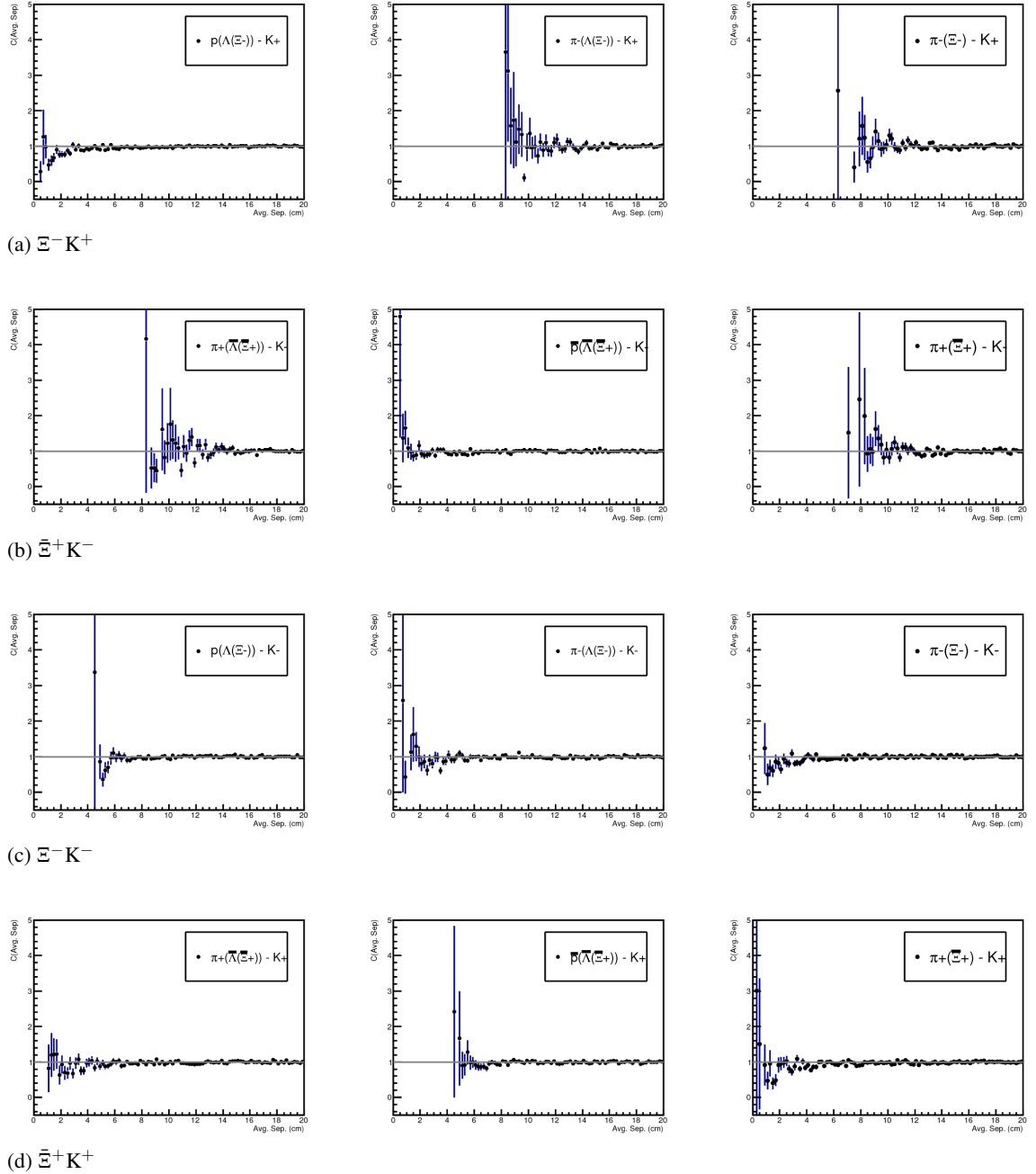


**Fig. 10:** Average separation (cm) correlation functions of  $\Xi$  Daughter and  $K^\pm$ . In the subfigure titles, the particles in “()” represent the mothers, ex. top left is  $p$  from  $\Lambda$  from  $\Xi^-$  with  $K^+$ .

## 300 4 Correlation Functions

301 This analysis studies the momentum correlations of both  $\Lambda$ -K and  $\Xi$ -K pairs using the two-particle correlation function, defined as  $C(k^*) = A(k^*)/B(k^*)$ , where  $A(k^*)$  is the signal distribution,  $B(k^*)$  is the reference (or background) distribution, and  $k^*$  is the momentum of one of the particles in the pair rest frame. In practice,  $A(k^*)$  is constructed by binning in  $k^*$  pairs from the same event. Ideally,  $B(k^*)$  is similar to  $A(k^*)$  in all respects excluding the presence of femtoscopic correlations [2]; as such,  $B(k^*)$  is used to divide out the phase-space effects, leaving only the femtoscopic effects in the correlation function.

307 In practice,  $B(k^*)$  is obtained by forming mixed-event pairs, i.e. particles from a given event are paired with particles from  $N_{mix}(= 5)$  other events, and these pairs are then binned in  $k^*$ . In forming the background distribution, it is important to mix only similar events; mixing events with different phase-spaces can lead to artificial signals in the correlation function. Therefore, in this analysis, we mix events with primary vertices within 2 cm and centralities within 5% of each other. Also note, a vertex correction is also applied to each event, which essentially re-centers the primary vertices to  $z = 0$ .

313 This analysis presents correlation functions for three centrality bins (0-10%, 10-30%, and 30-50%), and is currently pair transverse momentum ( $k_T = 0.5|\mathbf{p}_{T,1} + \mathbf{p}_{T,2}|$ ) integrated (i.e. not binned in  $k_T$ ).  
 314 The correlation functions are constructed separately for the two magnetic field configurations, and are  
 316 combined using a weighted average:

$$C_{combined}(k^*) = \frac{\sum_i w_i C_i(k^*)}{\sum_i w_i} \quad (3)$$

317 where the sum runs over the correlation functions to be combined, and the weight,  $w_i$ , is the number of  
 318 numerator pairs in  $C_i(k^*)$ . Here, the sum is over the two field configurations.

319 Figures 11, 12, and 13 show the correlation functions for all centralities studied for  $\Lambda K_S^0(\bar{\Lambda} K_S^0)$ ,  $\Lambda K^+(\bar{\Lambda} K^-)$ ,  
 320 and  $\Lambda K^-(\bar{\Lambda} K^+)$ , respectively. All were normalized in the range  $0.32 < k^* < 0.4$  GeV/c.

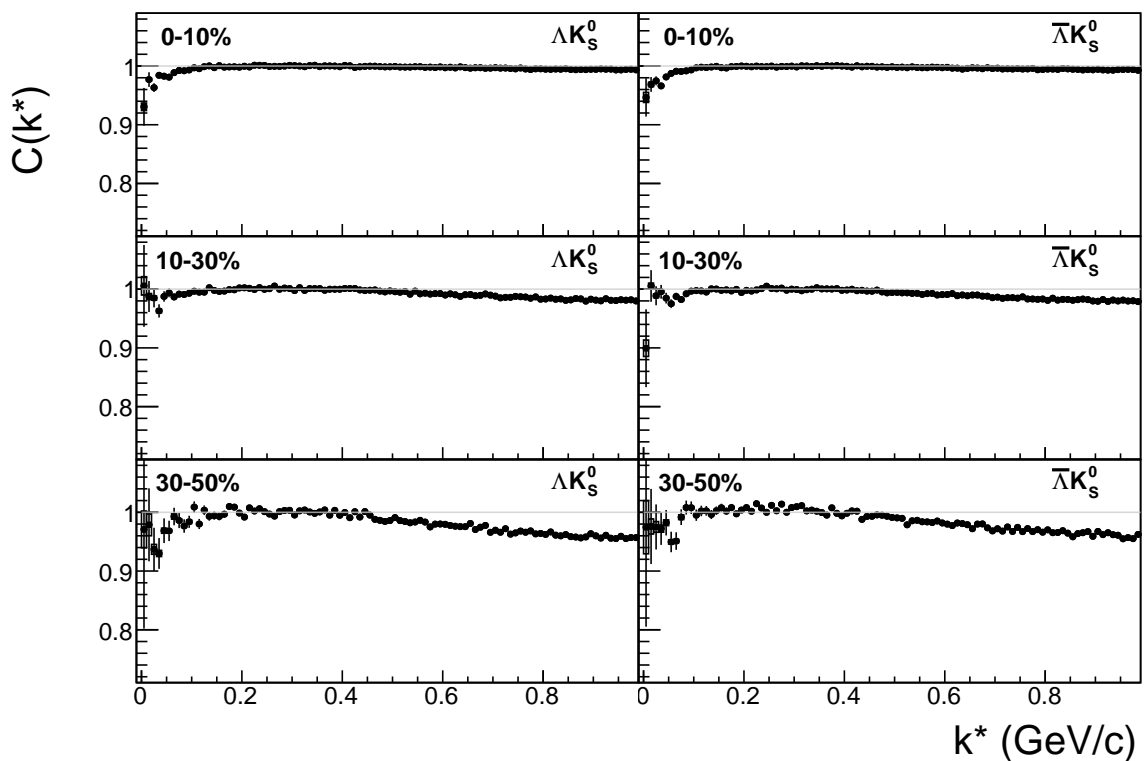


**Fig. 11:**  $\Lambda K_s^0$  (left) and  $\bar{\Lambda} K_s^0$  (right) correlation functions for 0-10% (top), 10-30% (middle), and 30-50% (bottom) centralities. The lines represent the statistical errors, while the boxes represent the systematic errors.

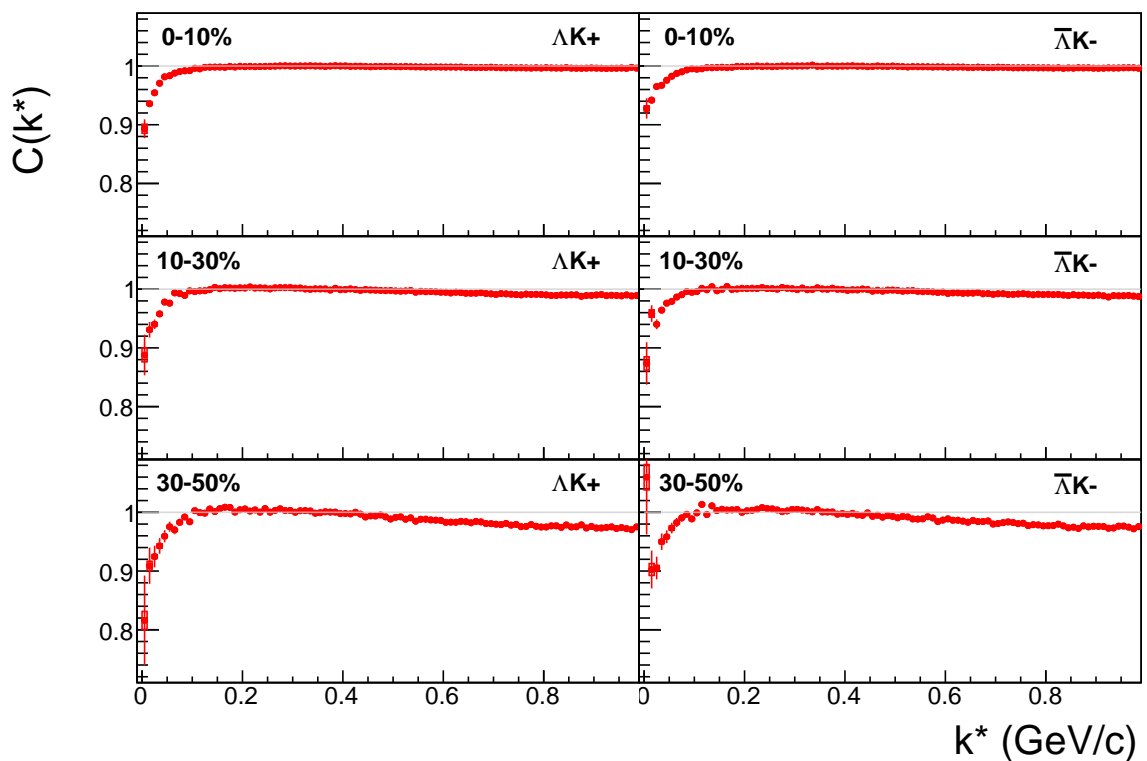


**Fig. 12:**  $\Lambda K^+$  (left) and  $\bar{\Lambda} K^-$  (right) correlation functions for 0-10% (top), 10-30% (middle), and 30-50% (bottom) centralities. The lines represent the statistical errors, while the boxes represent the systematic errors.

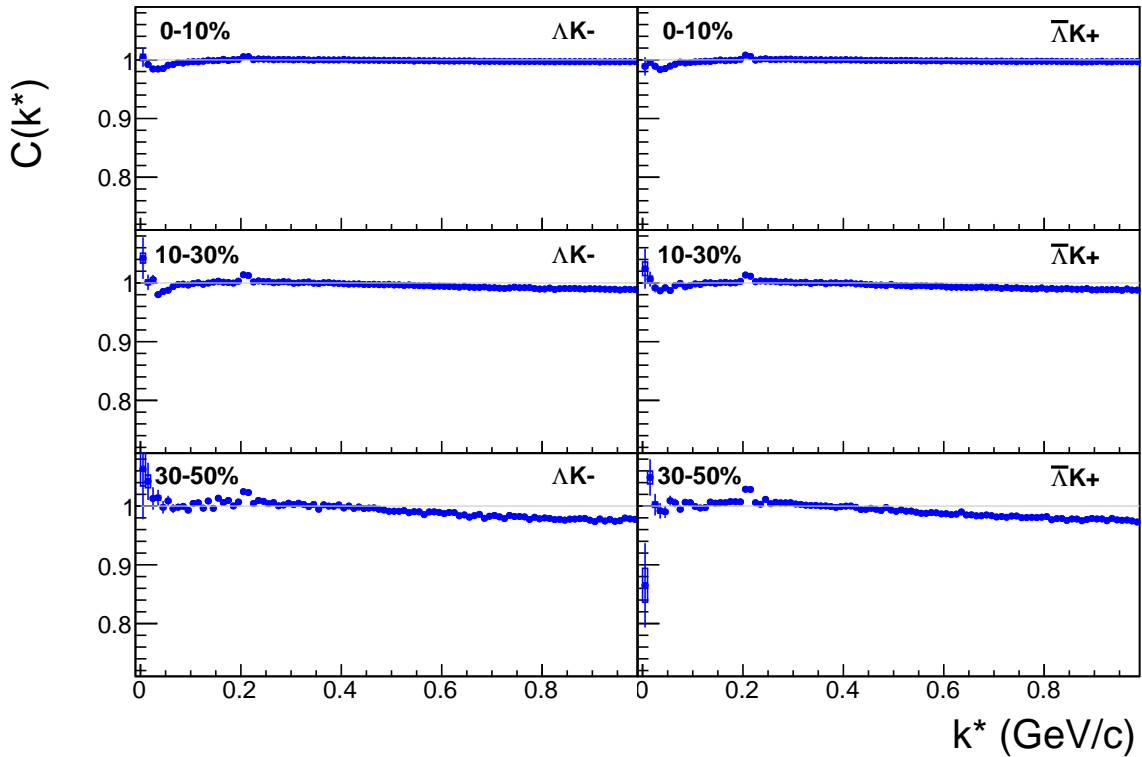


**Fig. 13:**  $\Lambda K^-$  (left) and  $\bar{\Lambda} K^+$  (right) correlation functions for 0-10% (top), 10-30% (middle), and 30-50% (bottom) centralities. The lines represent the statistical errors, while the boxes represent the systematic errors. The peak at  $k^* \approx 0.2$  GeV/c is due to the  $\Omega^-$  resonance.

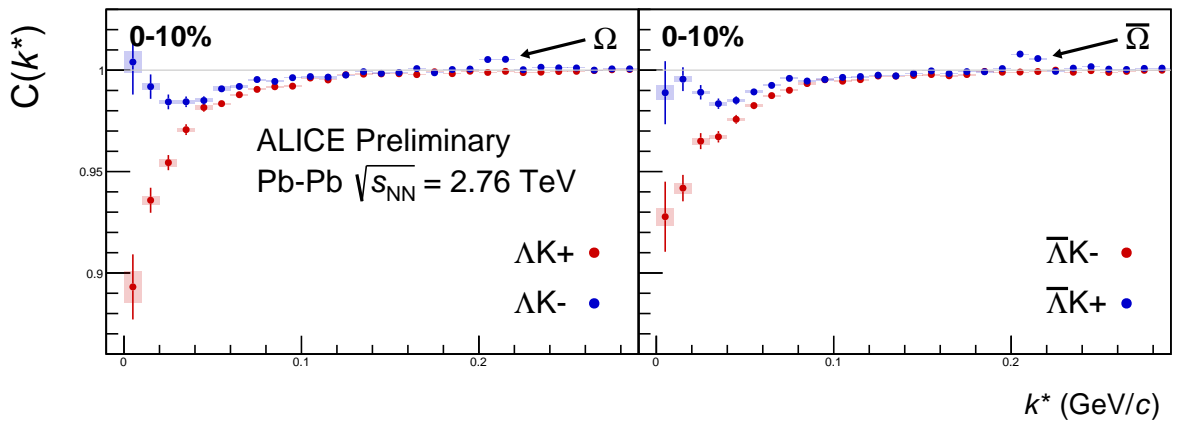


**Fig. 14:** Correlation Functions:  $\Lambda K^+$  vs  $\Lambda K^-$  ( $\bar{\Lambda} K^+$  vs  $\bar{\Lambda} K^-$ ) for 0-10% centrality. The peak in  $\Lambda K^-$  ( $\bar{\Lambda} K^+$ ) at  $k^* \approx 0.2$  GeV/c is due to the  $\Omega^-$  resonance. The lines represent the statistical errors. (NOTE: This figure is slightly dated, and a new one will be generated which includes both statistical and systematic uncertainties)

321 **5 Fitting**

322 **5.1 Model:  $\Lambda K_S^0$ ,  $\Lambda K^\pm$ ,  $\Xi^{ch} K_S^0$**

323 The two-particle relative momentum correlation function may be written theoretically by the Koonin-  
324 Pratt equation [3, 4]:

$$C(\mathbf{k}^*) = \int S(\mathbf{r}^*) |\Psi_{\mathbf{k}^*}(\mathbf{r}^*)|^2 d^3\mathbf{r}^* \quad (4)$$

325 In the absence of Coulomb effects, and assuming a spherically gaussian source of width  $R$ , the 1D  
326 femtoscopic correlation function can be calculated analytically using:

$$C(k^*) = 1 + C_{QI}(k^*) + C_{FSI}(k^*) \quad (5)$$

327  $C_{QI}$  describes plane-wave quantum interference:

$$C_{QI}(k^*) = \alpha \exp(-4k^{*2}R^2) \quad (6)$$

328 where  $\alpha = (-1)^{2j}/(2j+1)$  for identical particles with spin  $j$ , and  $\alpha = 0$  for non-identical particles.  
329 Obviously,  $\alpha = 0$  for all analyses presented in this note.  $C_{FSI}$  describes the s-wave strong final state  
330 interaction between the particles:

$$\begin{aligned} C_{FSI}(k^*) &= (1 + \alpha) \left[ \frac{1}{2} \left| \frac{f(k^*)}{R} \right|^2 \left( 1 - \frac{d_0}{2\sqrt{\pi}R} \right) + \frac{2\Re f(k^*)}{\sqrt{\pi}R} F_1(2k^*R) - \frac{\Im f(k^*)}{R} F_2(2k^*R) \right] \\ f(k^*) &= \left( \frac{1}{f_0} + \frac{1}{2} d_0 k^{*2} - ik^* \right)^{-1}; \quad F_1(z) = \int_0^z \frac{e^{x^2-z^2}}{z} dx; \quad F_2(z) = \frac{1-e^{-z^2}}{z} \end{aligned} \quad (7)$$

331 where  $R$  is the source size,  $f(k^*)$  is the s-wave scattering amplitude,  $f_0$  is the complex scattering length,  
332 and  $d_0$  is the effective range of the interaction.

333 An additional parameter  $\lambda$  is typically included in the femtoscopic fit function to account for the purity  
334 of the pair sample. In the case of no residual correlations (to be discussed in Section 5.4, the fit function  
335 becomes:

$$C(k^*) = 1 + \lambda [C_{QI}(k^*) + C_{FSI}(k^*)] \quad (8)$$

336 **5.2 Model:  $\Xi^{ch} K^{ch}$**

337 The two-particle correlation function may be written as:

$$C(\mathbf{k}^*) = \sum_S \rho_S \int S(\mathbf{r}^*) |\Psi_{\mathbf{k}^*}^S(\mathbf{r}^*)|^2 d^3\mathbf{r}^* \quad (9)$$

338 where  $\rho_S$  is the normalized emission probability of particles in a state with spin  $S$ ,  $S(\mathbf{r}^*)$  is the pair  
339 emission source distribution (assumed to be Gaussian), and  $\Psi_{\mathbf{k}^*}^S(\mathbf{r}^*)$  is the two-particle wave-function  
340 including both strong and Coulomb interactions [5]:

$$\Psi_{\mathbf{k}^*}(\mathbf{r}^*) = e^{i\delta_c} \sqrt{A_c(\eta)} [e^{i\mathbf{k}^* \cdot \mathbf{r}^*} F(-i\eta, 1, i\xi) + f_c(k^*) \frac{\tilde{G}(\rho, \eta)}{r^*}] \quad (10)$$

341 where  $\rho = k^* r^*$ ,  $\eta = (k^* a_c)^{-1}$ ,  $\xi = \mathbf{k}^* \cdot \mathbf{r}^* + k^* r^* \equiv \rho(1 + \cos \theta^*)$ , and  $a_c = (\mu z_1 z_2 e^2)^{-1}$  is the two-  
 342 particle Bohr radius (including the sign of the interaction).  $\delta_c$  is the Coulomb s-wave phase shift,  $A_c(\eta)$   
 343 is the Coulomb penetration factor,  $\tilde{G} = \sqrt{A_c}(G_0 + iF_0)$  is a combination of the regular ( $F_0$ ) and singular  
 344 ( $G_0$ ) s-wave Coulomb functions.  $f_c(k^*)$  is the s-wave scattering amplitude:

$$f_c(k^*) = \left[ \frac{1}{f_0} + \frac{1}{2} d_0 k^{*2} - \frac{2}{a_c} h(\eta) - ik^* A_c(\eta) \right]^{-1} \quad (11)$$

345 where, the “h-function”,  $h(\eta)$ , is expressed through the digamma function,  $\psi(z) = \Gamma'(z)/\Gamma(z)$  as:

$$h(\eta) = 0.5[\psi(i\eta) + \psi(-i\eta) - \ln(\eta^2)] \quad (12)$$

346 In this case, the  $\lambda$  parameter may be included as:

$$C(\mathbf{k}^*) = (1 - \lambda) + \lambda \sum_S \rho_S \int S(\mathbf{r}^*) |\Psi_{\mathbf{k}^*}^S(\mathbf{r}^*)|^2 d^3 \mathbf{r}^* \quad (13)$$

### 347 5.3 Momentum Resolution Corrections

348 Finite track momentum resolution causes the reconstructed momentum of a particle to smear around the  
 349 true value. This, of course, also holds true for V0 particles. The effect is propagated up to the pairs  
 350 of interest, which causes the reconstructed relative momentum ( $k_{Rec}^*$ ) to differ from the true momentum  
 351 ( $k_{True}^*$ ). Smearing of the momentum typically will result in a suppression of the signal.

352 The effect of finite momentum resolution can be investigated using the MC data, for which both the true  
 353 and reconstructed momenta are available. Figure 15 shows sample  $k_{True}^*$  vs.  $k_{Rec}^*$  plots for  $\Lambda(\bar{\Lambda})K^\pm$  0-  
 354 10% analyses; Figure 15a was generated using same-event pairs, while Figure 15b was generated using  
 355 mixed-event pairs (with  $N_{mix} = 5$ ).

356 If there are no contaminations in our particle collection, the plots in Figure 15 should be smeared around  
 357  $k_{True}^* = k_{Rec}^*$ ; this is mostly true in our analyses. However, there are some interesting features of our results  
 358 which demonstrate a small (notice the log-scale on the z-axis) contamination in our particle collection.  
 359 The structure around  $k_{Rec}^* = k_{True}^* - 0.15$  is mainly caused by  $K_S^0$  contamination in our  $\Lambda(\bar{\Lambda})$  sample. The  
 360 remaining structure not distributed about  $k_{Rec}^* = k_{True}^*$  is due to  $\pi$  and  $e$  contamination in our  $K^\pm$  sample.  
 361 These contaminations are more visible in Figure 16, which show  $k_{Rec}^*$  vs.  $k_{True}^*$  plots (for a small sample  
 362 of the  $\Lambda K^\pm$  0-10% central analysis), for which the MC truth (i.e. true, known identity of the particle)  
 363 was used to eliminate misidentified particles in the  $K^+(a)$  and  $\Lambda(b)$  collections. (NOTE: This is an old  
 364 figure and is for a small sample of the data. A new version will be generated shortly. It, nonetheless,  
 365 demonstrates the point well).

366 Information gained from looking at  $k_{Rec}^*$  vs  $k_{True}^*$  can be used to apply corrections to account for the  
 367 effects of finite momentum resolution on the correlation functions. A typical method involves using the  
 368 MC HIJING data to build two correlation functions,  $C_{Rec}(k^*)$  and  $C_{True}(k^*)$ , using the generator-level  
 369 momentum ( $k_{True}^*$ ) and the measured detector-level momentum ( $k_{Rec}^*$ ). The data is then corrected by  
 370 multiplying by the ratio,  $C_{True}/C_{Rec}$ , before fitting. This essentially unsmears the data, which that can  
 371 be compared directly to theoretical predictions and fits. Although this is conceptually simple, there are  
 372 a couple of big disadvantages to this method. First, HIJING does not incorporate final-state interactions,  
 373 so weights must be used when building same-event (numerator) distributions. These weights account for  
 374 the interactions, and, in the absence of Coulomb interactions, can be calculated using Eq. 5. Of course,  
 375 these weights are valid only for a particular set of fit parameters. Therefore, in the fitting process, during  
 376 which the fitter explores a large parameter set, the corrections will not remain valid. As such, applying  
 377 the momentum resolution correction and fitting becomes a long and drawn out iterative process. An initial

parameter set is obtained (through fitting without momentum resolution corrections, theoretical models, or a good guess), then the MC data is run over to obtain the correction factor, the data is fit using the correction factor, a refined parameter set is extracted, the MC data is run over again to obtain the new correction factor, etc. This process continues until the parameter set stabilizes. The second issue concerns statistics. With the MC data available on the grid, we were not able to generate the statistics necessary to use the raw  $C_{True}/C_{Rec}$  ratio. The ratio was not stable, and when applied to the data, obscured the signal. Attempting to fit the ratio to generate the corrections also proved problematic. However, as HIJING does not include final-state interactions, the same-event and mixed-event pairs are very similar (with the exception of things like energy and momentum conservation, etc). Therefore, one may build the numerator distribution using mixed-event pairs. This corresponds, more or less, to simply running a the weight generator through the detector framework.

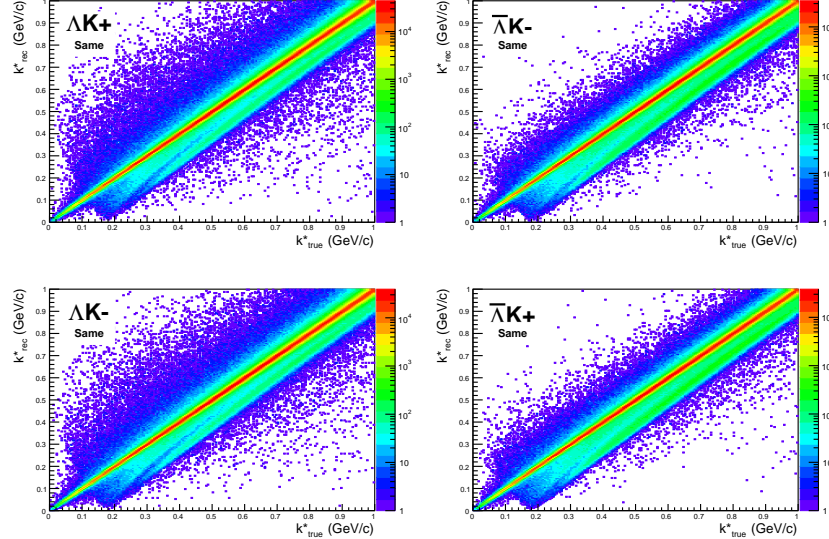
A second approach is to use information gained from plots like those in Figure 15, which can be considered response matrices. The response matrix describes quantitatively how each  $k_{Rec}^*$  bin receives contributions from multiple  $k_{True}^*$  bins, and can be used to account for the effects of finite momentum resolution. With this approach, the resolution correction is applied on-the-fly during the fitting process by propagating the theoretical (fit) correlation function through the response matrix, according to:

$$C_{fit}(k_{Rec}^*) = \frac{\sum_{k_{True}^*} M_{k_{Rec}^*, k_{True}^*} C_{fit}(k_{True}^*)}{\sum_{k_{True}^*} M_{k_{Rec}^*, k_{True}^*}} \quad (14)$$

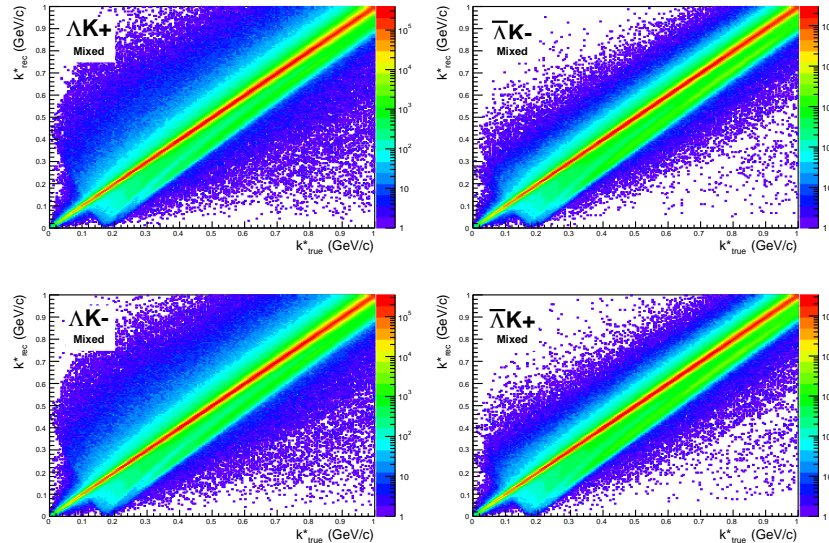
where  $M_{k_{Rec}^*, k_{True}^*}$  is the response matrix (Figure 15),  $C_{fit}(k_{True}^*)$  is the fit binned in  $k_{True}^*$ , and the denominator normalizes the result.

Equation 14 describes that, for a given  $k_{Rec}^*$  bin, the observed value of  $C(k_{Rec}^*)$  is a weighted average of all  $C(k_{True}^*)$  values, where the weights are the normalized number of counts in the  $[k_{Rec}^*, k_{True}^*]$  bin. As seen in Figure 15, overwhelmingly the main contributions come from the  $k_{Rec}^* = k_{True}^*$  bins. Although the correction is small, it is non-negligible for the low- $k^*$  region of the correlation function.

Here, the momentum resolution correction is applied to the fit, not the data. In other words, during fitting, the theoretical correlation function is smeared just as real data would be, instead of unsmeared the data. This may not be ideal for the theorist attempting to compare a model to experimental data, but it leaves the experimental data unadulterated. The current analyses use this second approach to applying momentum resolution corrections because of two major advantages. First, the MC data must be analyzed only once, and no assumptions about the fit are needed. Secondly, the momentum resolution correction is applied on-the-fly by the fitter, delegating the iterative process to a computer instead of the user.

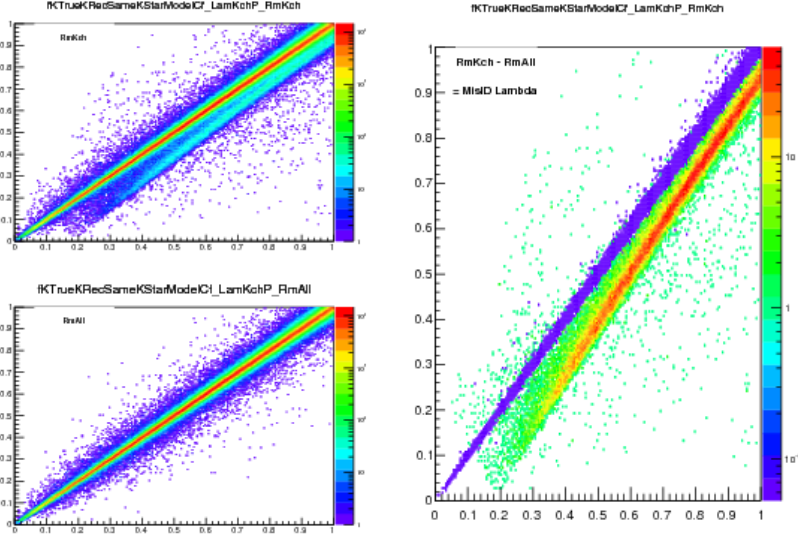


(a) Same Event Pairs ( $\Lambda(\bar{\Lambda})K^\pm$ , 0-10% Centrality)

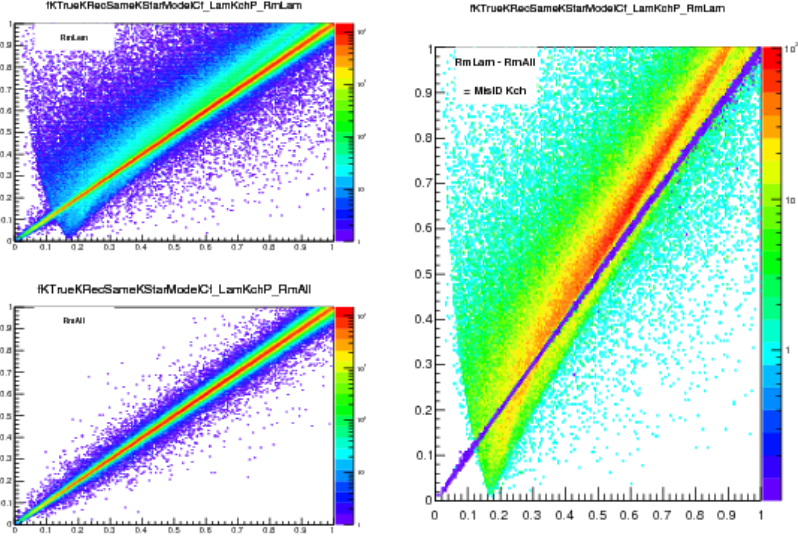


(b) Mixed Event Pairs ( $\Lambda(\bar{\Lambda})K^\pm$ , 0-10% Centrality)

**Fig. 15:** Sample  $k_{True}^*$  vs.  $k_{Rec}^*$  plot for  $\Lambda(\bar{\Lambda})K^\pm$  0-10% analyses. The structure which appears around  $k_{Rec}^* = k_{True}^* - 0.15$  is mainly caused by  $K_S^0$  contamination in our  $\Lambda(\bar{\Lambda})$  sample. The remaining structure not distributed about  $k_{Rec}^* = k_{True}^*$  is due to  $\pi$  and  $e$  contamination in our  $K^\pm$  sample. These contaminations are more clearly visible in Figure 16



(a) (Top Left) All misidentified  $K^+$  excluded. (Bottom Left) All misidentified  $\Lambda$  and  $K^+$  excluded. (Right) The difference of (Top Left) - (Bottom Left), which reveals the contamination in our  $\Lambda$  collection. The structure which appears around  $k_{Rec}^* = k_{True}^* - 0.15$  is mainly caused by  $K_S^0$  contamination in our  $\Lambda(\bar{\Lambda})$  sample.



(b) (Top Left) All misidentified  $\Lambda$  excluded. (Bottom Left) All misidentified  $\Lambda$  and  $K^+$  excluded. (Right) The difference of (Top Left) - (Bottom Left), which reveals the contamination in our  $K^+$  collection. The structure not distributed about  $k_{Rec}^* = k_{True}^*$  is due to  $\pi$  and  $e^-$  contamination in our  $K^\pm$  sample.

**Fig. 16:** Note: This is an old figure and is for a small sample of the data. A new version will be generated shortly.  
y-axis =  $k_{Rec}^*$ , x-axis =  $k_{True}^*$ .

(Left)  $k_{Rec}^*$  vs.  $k_{True}^*$  plots for a small sample of the  $\Lambda K^+$  0-10% central analysis, MC truth was used to eliminate misidentified particles in the  $K^+$ (a) and  $\Lambda$ (b) collections. (Right) The difference of the top left and bottom left plots. Contaminations in our particle collections are clearly visible. Figure (a) demonstrates a  $K_S^0$  contamination in our  $\Lambda$  collection; Figure (b) demonstrates a  $\pi$  and  $e^-$  contamination in our  $K^\pm$  collection.

407 **5.4 Residual Correlations**

408 The purpose of this analysis is study the interaction and scale of the emitting source of the pairs. In  
 409 order to obtain correct results, it is important for our particle collections to consist of primary particles.  
 410 In practice, this is difficult to achieve for our  $\Lambda$  and  $\bar{\Lambda}$  collections. Many of our  $\Lambda$  particles are not  
 411 primary, but originate as decay products from other hyperons, including  $\Sigma^0$ ,  $\Xi^0$ ,  $\Xi^-$  and  $\Sigma^{*(+,-,0)}(1385)$ .  
 412 Additionally, many of our K particles are not primary, but decay from  $K^{*(+,-,0)}(892)$  parents. In these  
 413 decays, the  $\Lambda$  carries away a momentum very similar to that of its parent. As a result, the correlation  
 414 function between a secondary  $\Lambda$  and, for instance, a  $K^+$  will be sensitive to, and dependent upon, the  
 415 interaction between the parent of the  $\Lambda$  and the  $K^+$ . In effect, the correlation between the parent of  
 416 the  $\Lambda$  and the  $K^+$  (ex.  $\Sigma^0 K^+$ ) will be visible, although smeared out, in the  $\Lambda K^+$  data. We call this a  
 417 residual correlation resulting from feed-down. Residual correlations are important in an analysis when  
 418 three criteria are met [6]: i) the parent correlation signal is large, ii) a large fraction of pairs in the sample  
 419 originate from the particular parent system, and iii) the decay momenta are comparable to the expected  
 420 correlation width in  $k^*$ .

421 As it is difficult for us to eliminate these residual correlations in our analyses, we must attempt to account  
 422 for them in our fitter. To achieve this, we will simultaneously fit the data for both the primary correlation  
 423 function and the residual correlations. For example, in the simple case of a  $\Lambda K^+$  analysis with residuals  
 424 arising solely from  $\Sigma^0 K^+$  feed-down:

$$C_{measured}(k_{\Lambda K^+}^*) = 1 + \lambda_{\Lambda K^+}[C_{\Lambda K^+}(k_{\Lambda K^+}^*) - 1] + \lambda_{\Sigma^0 K^+}[C_{\Sigma^0 K^+}(k_{\Lambda K^+}^*) - 1]$$

$$C_{\Sigma^0 K^+}(k_{\Lambda K^+}^*) \equiv \frac{\sum_{k_{\Sigma^0 K^+}^*} C_{\Sigma^0 K^+}(k_{\Sigma^0 K^+}^*) T(k_{\Sigma^0 K^+}^*, k_{\Lambda K^+}^*)}{\sum_{k_{\Sigma^0 K^+}^*} T(k_{\Sigma^0 K^+}^*, k_{\Lambda K^+}^*)} \quad (15)$$

425  $C_{\Sigma^0 K^+}(k_{\Sigma^0 K^+}^*)$  is the  $\Sigma^0 K^+$  correlation function from, for instance, Equation 5, and  $T$  is the transform  
 426 matrix generated with THERMINATOR. The transform matrix is formed for a given parent pair, AB,  
 427 by taking all  $\Lambda K$  pairs originating from AB, calculating the relative momentum of the parents ( $k^*_{AB}$ )  
 428 and daughters ( $k^*_{\Lambda K}$ ), and filling a two-dimensional histogram with the values. The transform matrix  
 429 is essentially an unnormalized probability distribution mapping the  $k^*$  of the parent pair to that of the  
 430 daughter pair when one or both parents decay. An example of such transform matrices can be found in  
 431 Figures 17 and 18.

432 The above equation can be easily extended to include feed-down from more sources:

$$C_{measured}(k_{\Lambda K}^*) = 1 + \lambda_{\Lambda K}[C_{\Lambda K}(k_{\Lambda K}^*) - 1] + \lambda_{\Sigma^0 K}[C_{\Sigma^0 K}(k_{\Lambda K}^*) - 1] + \dots$$

$$+ \lambda_{P_1 P_2}[C_{P_1 P_2}(k_{\Lambda K}^*) - 1] + \lambda_{other}[C_{other}(k_{\Lambda K}^*) - 1]$$

$$C_{P_1 P_2}(k_{\Lambda K}^*) \equiv \frac{\sum_{k_{P_1 P_2}^*} C_{P_1 P_2}(k_{P_1 P_2}^*) T(k_{P_1 P_2}^*, k_{\Lambda K}^*)}{\sum_{k_{P_1 P_2}^*} T(k_{P_1 P_2}^*, k_{\Lambda K}^*)} \quad (16)$$

433 Or, more compactly:

$$C_{measured}(k_{\Lambda K}^*) = 1 + \sum_i \lambda_i [C_i(k_{\Lambda K}^*) - 1] \quad (17)$$

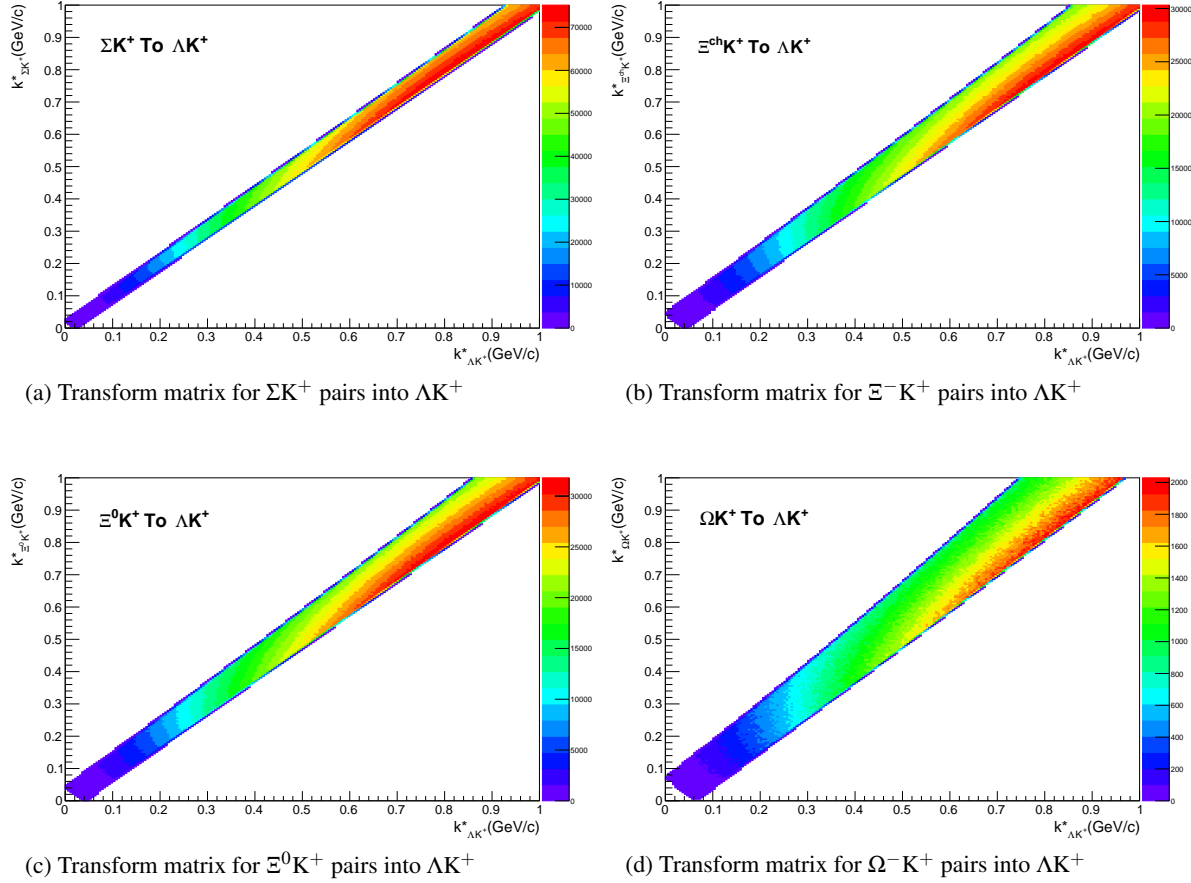


**Fig. 17:** Transform Matrices generated with THERMINATOR for  $\Lambda K^+$  Analysis

434 So, in practice, we model the correlation function of the parents, and run the correlation function through  
435 the appropriate transform matrix to determine the contribution to the daughter correlation function. A  
436 few questions still remain. First, what  $\lambda$  values should be used in the above equation? One option  
437 would be to leave all of these  $\lambda$ -parameters free during the fit process. However, this would introduce  
438 a huge number of new parameters into the fitter, and would make the fit results less trustworthy. The  $\lambda$   
439 parameters roughly dictate the strength of the parent contribution to the daughter pair. Additionally, as  
440 found in [7], the reconstruction efficiency for primary  $\Lambda$  particles is nearly equal to that of  $\Lambda$  particles  
441 originating from  $\Sigma$ ,  $\Sigma^*$ ,  $\Xi^0$ ,  $\Xi^-$ , and  $\Omega$  hyperons. Therefore, the  $\lambda$  parameter for parent system AB can  
442 be estimated using THERMINATOR as the total number of  $\Lambda K$  pairs originating from AB ( $N_{AB}$ ) divided  
443 by the total number of  $\Lambda K$  pairs ( $N_{Total}$ ):

$$\lambda_{AB} = \frac{N_{AB}}{N_{Total}} \quad (18)$$

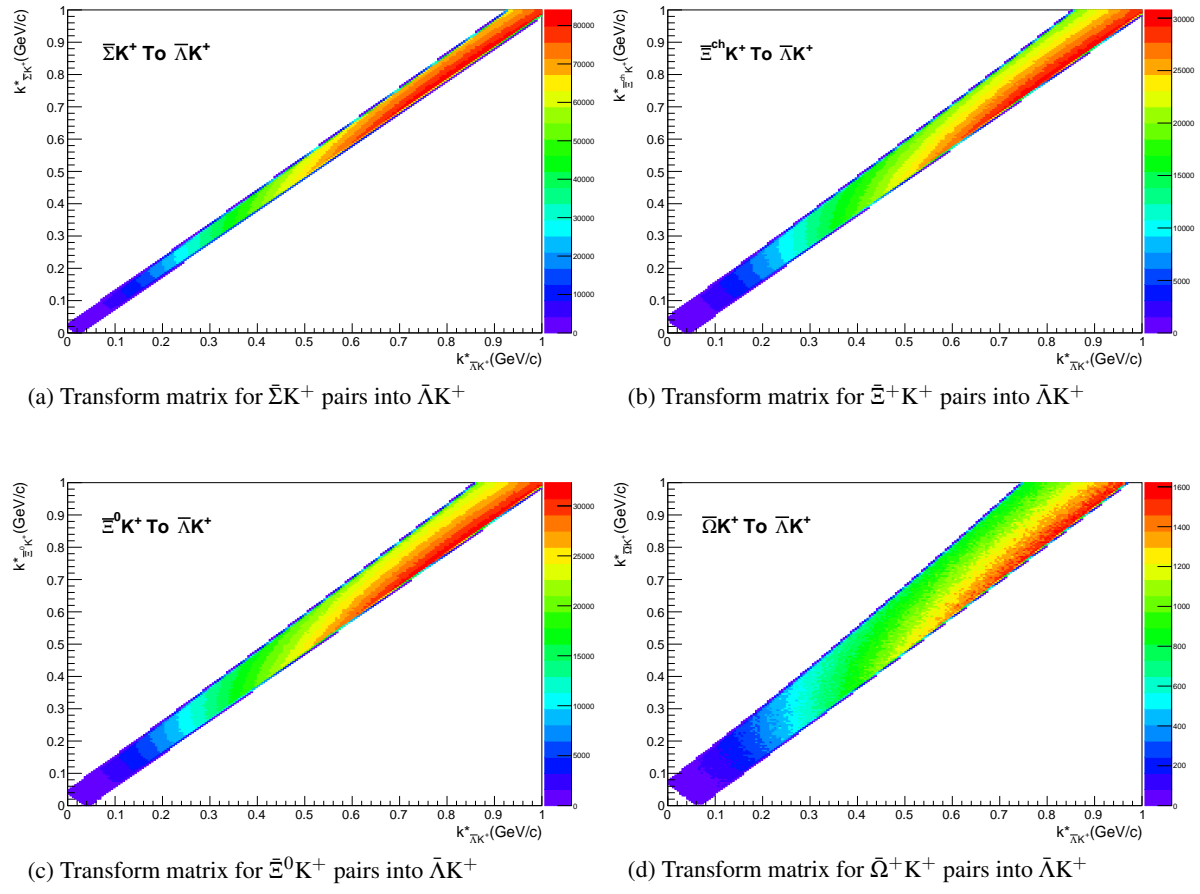


**Fig. 18:** Transform Matrices generated with THERMINATOR for  $\bar{\Lambda}K^+$  Analysis

$\Lambda K^+$ Residuals		$\bar{\Lambda} K^-$ Residuals	
Pair System	$\lambda$ value	Pair System	$\lambda$ value
$\Lambda K^+$	0.154	$\bar{\Lambda} K^-$	0.158
$\Sigma^0 K^+$	0.099	$\bar{\Sigma}^0 K^-$	0.102
$\Xi^0 K^+$	0.072	$\bar{\Xi}^0 K^-$	0.067
$\Xi^- K^+$	0.069	$\bar{\Xi}^+ K^-$	0.065
Other	0.558	Other	0.560
Fakes	0.048	Fakes	0.048

**Table 1:**  $\lambda$  values for the individual components of the  $\Lambda K^+$  (left) and  $\bar{\Lambda} K^-$  (right) correlation functions for the case of 3 residual contributions.

$\Lambda K^+$ Residuals		$\bar{\Lambda} K^-$ Residuals	
Pair System	$\lambda$ value	Pair System	$\lambda$ value
$\Lambda K^+$	0.154	$\bar{\Lambda} K^-$	0.158
$\Sigma^0 K^+$	0.099	$\bar{\Sigma}^0 K^-$	0.102
$\Xi^0 K^+$	0.072	$\bar{\Xi}^0 K^-$	0.067
$\Xi^- K^+$	0.069	$\bar{\Xi}^+ K^-$	0.065
$\Sigma^{*+} K^+$	0.046	$\bar{\Sigma}^{*-} K^-$	0.046
$\Sigma^{*-} K^+$	0.042	$\bar{\Sigma}^{*+} K^-$	0.045
$\Sigma^{*0} K^+$	0.042	$\bar{\Sigma}^{*0} K^-$	0.040
$\Lambda K^{*0}$	0.039	$\bar{\Lambda} \bar{K}^{*0}$	0.041
$\Sigma^0 K^{*0}$	0.035	$\bar{\Sigma}^0 \bar{K}^{*0}$	0.036
$\Xi^0 K^{*0}$	0.025	$\bar{\Xi}^0 \bar{K}^{*0}$	0.024
$\Xi^- K^{*0}$	0.024	$\bar{\Xi}^+ \bar{K}^{*0}$	0.023
Other	0.305	Other	0.305
Fakes	0.048	Fakes	0.048

**Table 2:**  $\lambda$  values for the individual components of the  $\Lambda K^+$  (left) and  $\bar{\Lambda} K^-$  (right) correlation functions for the case of 10 residual contributions.

AK <sup>-</sup> Residuals		ĀK <sup>+</sup> Residuals	
Pair System	λ value	Pair System	λ value
ΛK <sup>-</sup>	0.154	ĀK <sup>+</sup>	0.158
Σ <sup>0</sup> K <sup>-</sup>	0.099	ĀΣ <sup>0</sup> K <sup>+</sup>	0.103
Ξ <sup>0</sup> K <sup>-</sup>	0.071	ĀΞ <sup>0</sup> K <sup>+</sup>	0.068
Ξ <sup>-</sup> K <sup>-</sup>	0.068	ĀΞ <sup>+</sup> K <sup>+</sup>	0.066
Other	0.561	Other	0.557
Fakes	0.048	Fakes	0.048

**Table 3:**  $\lambda$  values for the individual components of the  $\Lambda K^-$  (left) and  $\bar{\Lambda} K^+$  (right) correlation functions for the case of 3 residual contributions.

AK <sup>-</sup> Residuals		ĀK <sup>+</sup> Residuals	
Pair System	λ value	Pair System	λ value
ΛK <sup>-</sup>	0.154	ĀK <sup>+</sup>	0.158
Σ <sup>0</sup> K <sup>-</sup>	0.099	ĀΣ <sup>0</sup> K <sup>+</sup>	0.103
Ξ <sup>0</sup> K <sup>-</sup>	0.071	ĀΞ <sup>0</sup> K <sup>+</sup>	0.068
Ξ <sup>-</sup> K <sup>-</sup>	0.068	ĀΞ <sup>+</sup> K <sup>+</sup>	0.066
Σ <sup>*+</sup> K <sup>-</sup>	0.046	ĀΣ <sup>*-</sup> K <sup>+</sup>	0.046
Σ <sup>*-</sup> K <sup>-</sup>	0.041	ĀΣ <sup>*+</sup> K <sup>+</sup>	0.045
Σ <sup>*0</sup> K <sup>-</sup>	0.041	ĀΣ <sup>*0</sup> K <sup>+</sup>	0.041
ΛĀK <sup>*0</sup>	0.039	ĀΛK <sup>*0</sup>	0.041
Σ <sup>0</sup> ĀK <sup>*0</sup>	0.035	ĀΣ <sup>0</sup> K <sup>*0</sup>	0.036
Ξ <sup>0</sup> ĀK <sup>*0</sup>	0.025	ĀΞ <sup>0</sup> K <sup>*0</sup>	0.024
Ξ <sup>-</sup> ĀK <sup>*0</sup>	0.024	ĀΞ <sup>+</sup> K <sup>*0</sup>	0.023
Other	0.308	Other	0.301
Fakes	0.048	Fakes	0.048

**Table 4:**  $\lambda$  values for the individual components of the  $\Lambda K^-$  (left) and  $\bar{\Lambda} K^+$  (right) correlation functions for the case of 10 residual contributions.

$\Lambda K_S^0$ Residuals		$\bar{\Lambda} K_S^0$ Residuals	
Pair System	$\lambda$ value	Pair System	$\lambda$ value
$\Lambda K_S^0$	0.165	$\bar{\Lambda} K_S^0$	0.169
$\Sigma^0 K_S^0$	0.107	$\bar{\Sigma}^0 K_S^0$	0.111
$\Xi^0 K_S^0$	0.077	$\bar{\Xi}^0 K_S^0$	0.073
$\Xi^- K_S^0$	0.075	$\bar{\Xi}^+ K_S^0$	0.071
Other	0.528	Other	0.528
Fakes	0.048	Fakes	0.048

**Table 5:**  $\lambda$  values for the individual components of the  $\Lambda K_S^0$  (left) and  $\bar{\Lambda} K_S^0$  (right) correlation functions for the case of 3 residual contributions.

$\Lambda K_S^0$ Residuals		$\bar{\Lambda} K_S^0$ Residuals	
Pair System	$\lambda$ value	Pair System	$\lambda$ value
$\Lambda K_S^0$	0.165	$\bar{\Lambda} K_S^0$	0.169
$\Sigma^0 K_S^0$	0.107	$\bar{\Sigma}^0 K_S^0$	0.111
$\Xi^0 K_S^0$	0.077	$\bar{\Xi}^0 K_S^0$	0.073
$\Xi^- K_S^0$	0.075	$\bar{\Xi}^+ K_S^0$	0.071
$\Sigma^{*+} K_S^0$	0.050	$\bar{\Sigma}^{*-} K_S^0$	0.050
$\Sigma^{*-} K_S^0$	0.045	$\bar{\Sigma}^{*+} K_S^0$	0.049
$\Sigma^{*0} K_S^0$	0.045	$\bar{\Sigma}^{*0} K_S^0$	0.044
$\Lambda K^{*0}$	0.019	$\bar{\Lambda} K^{*0}$	0.020
$\Sigma^0 K^{*0}$	0.017	$\bar{\Sigma}^0 K^{*0}$	0.017
$\Xi^0 K^{*0}$	0.012	$\bar{\Xi}^0 K^{*0}$	0.011
$\Xi^- K^{*0}$	0.012	$\bar{\Xi}^+ K^{*0}$	0.011
Other	0.329	Other	0.326
Fakes	0.048	Fakes	0.048

**Table 6:**  $\lambda$  values for the individual components of the  $\Lambda K_S^0$  (left) and  $\bar{\Lambda} K_S^0$  (right) correlation functions for the case of 10 residual contributions.

Now, the remaining question is how do we model the parent correlation functions? In an ideal world, we would simply look up the parent interaction in some table, and input this into our Lednicky equation (for the case of one or more charge neutral particle in the pair), or run it through the CoulombFitter machinery described in Sec. 5.2. Unfortunately, the world in which we live is not perfect, such a table does not exist, and little is known about the interaction between the residual pairs in this study. One solution would be to introduce a set of scattering parameters and radii for each residual system. However, as will be the case of the  $\lambda$ -parameters above, this would introduce a large number of additional fit parameters, and would make our fitter too unconstrained and would yield untrustworthy results. The second option, which is adopted in this analysis, is to assume all residual pairs have the same source size as the daughter pair, and all Coulomb-neutral residual pairs also share the same scattering parameters as the daughter pair (the case of charged pairs will be described below).

Concerning the radii of the residual parent pairs, it was suggested that these should be set to smaller values. In the interest of minimizing the number of parameters in the fitter, we tested this by introducing an  $m_T$ -scaling of the parent radii. The motivation for this scaling comes from the approximate  $m_T$ -scaling of the radii observed in 45. To achieve this scaling, we assume the radii follow an inverse-square-root distribution:  $R_{AB} = \alpha m_T^{-1/2}$ . Then, it follows that we should scale the parent radii as:

$$R_{AB} = R_{\Lambda K} \left( \frac{m_{T,AB}}{m_{T,\Lambda K}} \right)^{-1/2} \quad (19)$$

460 The values for  $m_T$  for each pair system was taken from THERMINATOR. As the fitter dances around  
 461 parameter space and selects new radii for the  $\Lambda K$  pairs, the radii of the residuals is scaled by the above  
 462 factor. In the end, this scaling factor made no significant difference in our fit results, so this complication  
 463 is excluded from our final results. Note that this is not surprising, as the most extreme scaling factor  
 464 was, in the case of using 10 residual systems, between  $\Lambda K^+$  with  $m_{T,\Lambda K^+} \approx 1.4 \text{ GeV}/c^2$  and  $\Xi^- K^{*0}$  with  
 465  $m_{T,\Xi^- K^{*0}} \approx 1.8 \text{ GeV}/c^2$ , resulting in a scale factor of  $\approx 0.9$ .

466 Now, as hinted above, accounting for charged residuals adds a complication in that they necessitate the  
 467 inclusion of the CoulombFitter into the process. The complication of combining the two fitters is not  
 468 troubling, but it increases the fitting time drastically (the parallelization of the CoulombFitter across a  
 469 large number of GPU cores, to drastically decrease run-time, is currently underway). We have two so-  
 470 lutions to bypass such a large increase in run time. First, we can use our experimental  $\Xi^{\text{ch}} K^{\text{ch}}$  data to  
 471 represent all charged parent pair system. In this case, there is no need to make any assumption about  
 472 scattering parameters or source sizes, as we already have the experimental data. The downside is that,  
 473 especially in the 30-50% centrality bin, the error bars on the data are large. Alternatively, we can assume  
 474 the strong interaction is negligible in the charged residual, and generate the parent correlation function  
 475 given radius and  $\lambda$  parameters. We find in our  $\Xi^{\text{ch}} K^{\text{ch}}$  study that a Coulomb-only description of the sys-  
 476 tem describes, reasonably well, the broad features of the correlation. The strong interaction is necessary  
 477 for the fine details. However, as these correlations are run through a transform matrix, which largely  
 478 flattens out and fine details, a Coulomb-only description should be sufficient. In practice, this Coulomb-  
 479 only scenario is achieved by first building a large number of Coulomb-only correlations for various radii  
 480 and  $\lambda$  parameter values, and interpolating from this grid during the fitting process. We find consistent  
 481 results between using the  $\Xi K$  data and the Coulomb-only interpolation method. When the number of  
 482 residual pairs used is increased to 10, so that pairs such as  $\Sigma^{*+} K^-$  enter the picture, the Coulomb-only  
 483 interpolation method is used. In other words, the  $\Xi K$  experimental data is only used to model the  $\Xi K$   
 484 residual contribution, all other charged pairs are treated with the Coulomb-only interpolation method.

485 Two examples of how very different transform matrices can alter a correlation function are shown in  
 486 Figures 19 and 20 below. These figures were taken using parameter values obtained from fits to the data.  
 487 In the top left corner of the figures, the input correlation function (closed symbols) is shown together  
 488 with the output, transformed, correlation function (open symbols). In the bottom left, the transformed  
 489 correlation is shown by itself. This is especially helpful when the  $\lambda$  parameter is very small, in which  
 490 case the contribution in the top left can look flat, but the zoomed in view in the bottom left shows the  
 491 structure. The right two plots in each figure show the transform matrix without (top right) and with  
 492 (bottom right) a log-scale on the z-axis. Note, more examples of these transforms can be found in Sec.  
 493 9.

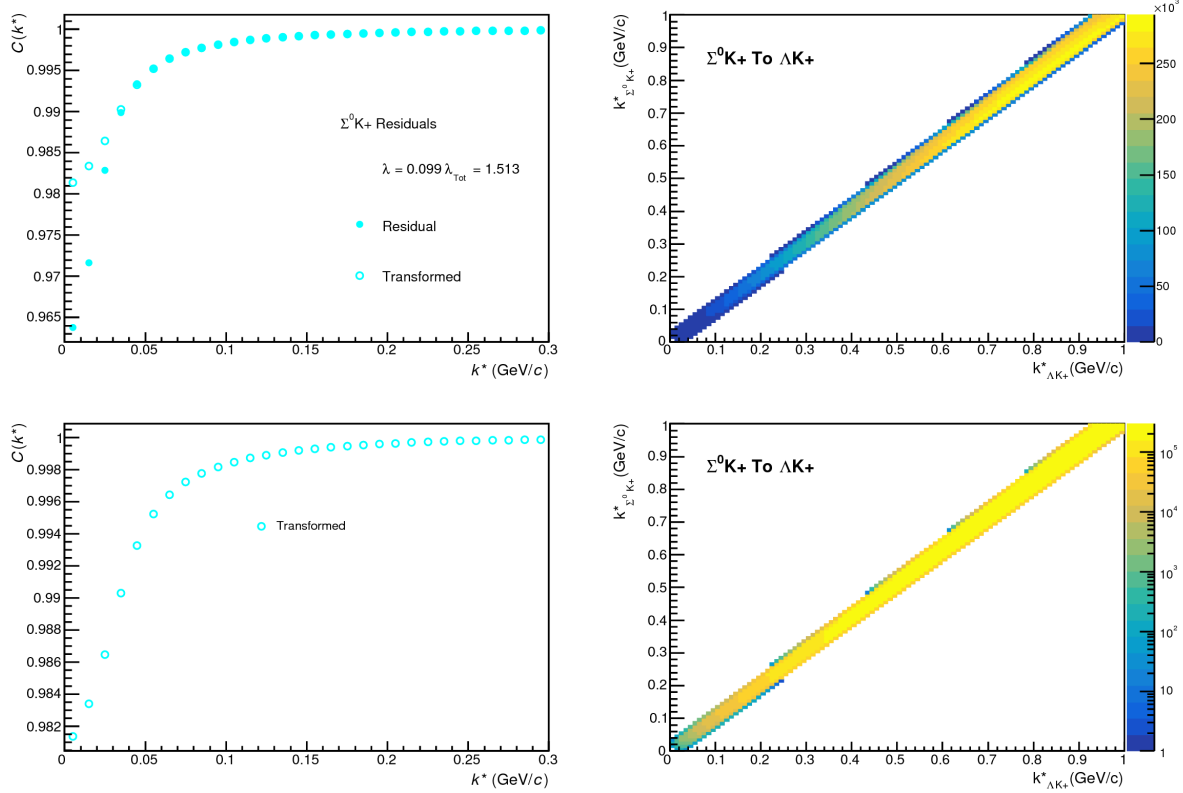


**Fig. 19:**  $\Sigma^0 \text{K}^+$  Transform. These figures were taken using parameter values obtained from fits to the data. In the top left corner of the figures, the input correlation function (closed symbols) is shown together with the output, transformed, correlation function (open symbols). In the bottom left, the transformed correlation is shown by itself. The right two plots in each figure show the transform matrix without (top right) and with (bottom right) a log-scale on the z-axis.

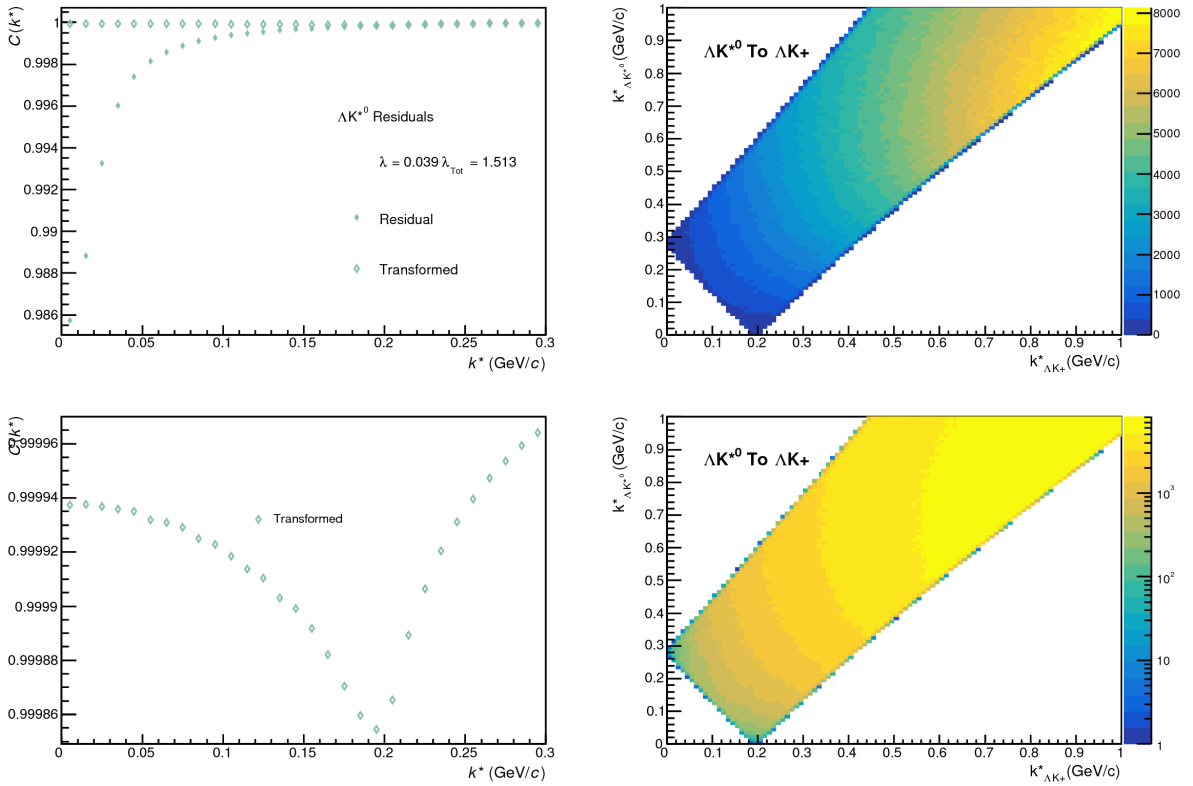


**Fig. 20:**  $\Sigma^0 K^+$  Transform. These figures were taken using parameter values obtained from fits to the data. In the top left corner of the figures, the input correlation function (closed symbols) is shown together with the output, transformed, correlation function (open symbols). In the bottom left, the transformed correlation is shown by itself. The right two plots in each figure show the transform matrix without (top right) and with (bottom right) a log-scale on the z-axis.

494 **5.5 Non-Flat Background**

495 Non-flat background Adam's paper [8].

496 **5.6 LednickyFitter**

497 The code developed to fit the data is called "LednickyFitter", and utilizes the ROOT TMinuit implemen-  
 498 tation of the MINUIT fitting package. In short, given a function with a number of parameters, the fitter  
 499 explores the parameter space searching for the minimum of the equation. In this implementation, the  
 500 function to be minimized should represent the difference between the measure and theoretical correla-  
 501 tion functions. However, a simple  $\chi^2$  test is inappropriate for fitting correlation functions, as the ratio  
 502 two Poisson distributions does not result in a Poisson distribution. Instead, a log-likelihood fit function  
 503 of the following form is used [2]:

$$\chi^2_{PML} = -2 \left[ A \ln \left( \frac{C(A+B)}{A(C+1)} \right) + B \ln \left( \frac{A+B}{B(C+1)} \right) \right] \quad (20)$$

504 where  $A$  is the experimental signal distribution (numerator),  $B$  is the experimental background distribu-  
 505 tion (denominator), and  $C$  is the theoretical fit correlation function.

506 The LednickyFitter uses Equations 5 – 7 to build the theoretical fit, and Equation 20 as the statistic  
 507 quantifying the quality of the fit. The parameters to be varied by MINUIT are:  $\lambda$ ,  $R$ ,  $f_0$  ( $\mathbb{R}f_0$  and  $\mathbb{I}f_0$   
 508 separately),  $d_0$ , and normalization  $N$ . The fitter currently includes methods to correct for momentum  
 509 resolution and a non-flat background. These corrections are applied to the fit function, the data is never  
 510 touched. The fitter is able to share parameters between different analyses and fit all simultaneously.

511 In a typical fit, a given pair is fit with its conjugate (ex.  $\Lambda K^+$  with  $\bar{\Lambda} K^-$ ) across all centralities (0-10%,  
 512 10-30%, 30-50%), for a total of 6 simultaneous analyses. Each analysis has a unique  $\lambda$  and normalization  
 513 parameter. The radii are shared between analyses of like centrality, as these should have similar source  
 514 sizes. The scattering parameters ( $\mathbb{R}f_0$ ,  $\mathbb{I}f_0$ ,  $d_0$ ) are shared amongst all.

515 In the case of fitting with residuals, the  $\lambda_{Fit}$  parameter serves as an overall normalization shared by all  
 516 contributors, such that Eqn 17 becomes:

$$\begin{aligned} C_{measured}(k_{\Lambda K}^*) &= 1 + \sum_i \lambda'_i [C_i(k_{\Lambda K}^*) - 1] \\ \lambda'_i &= \lambda_{Fit} \lambda_i \\ \sum_i \lambda'_i &= \lambda_{Fit} \sum_i \lambda_i = \lambda_{Fit} \end{aligned} \quad (21)$$

517 where  $\lambda_i$  is obtained from THERMINATOR, as explained in Section 5.4, and whose values are presented  
 518 in Tables 1 through 6. For Coulomb-neutral pairs, such as  $\Lambda K$ ,  $\Sigma^0 K$ , and  $\Xi^0 K$ ,  $C_i(k_{\Lambda K}^*)$  is calculated from  
 519 Eqn. 5, with the help of Eqn. 7. For those residual pairs which include a Coulomb interaction,  $C_i(k_{\Lambda K}^*)$   
 520 is either calculated using the CoulombFitter method (Sections 5.2 and 5.7) with no strong interaction, or  
 521 by using the  $\Xi^{ch} K^{ch}$  data directly. Unless otherwise stated, the  $\Xi^{ch} K^{ch}$  residual contribution is modeled  
 522 using the experimental  $\Xi^{ch} K^{ch}$  data, and all other charged contributors (ex.  $\Sigma^{*ch} K^{ch}$ ) are modeled using  
 523 the CoulombFitter technique with no strong interaction contribution.

524 To summarize, the complete fit function is constructed as follows:

- 525 1. The uncorrected correlation function,  $C'_{Fit}(k_{True}^*)$ , is constructed using Eq. 22

526 – in the case of no residual contributions included in the fit,  $\lambda_i = \lambda_{\text{AK}}$  in Eq. 22 is set equal to  
 527 1. Then, the extracted  $\lambda_{\text{Fit}}$  parameter should be roughly equal to the pair purity.

528 2. The correlation function is corrected to account for momentum resolution effects using Eq. 14

$$529 - C'_{\text{fit}}(k_{\text{Rec}}^*) = \frac{\sum_{k_{\text{True}}^*} M_{k_{\text{Rec}}^*, k_{\text{True}}^*} C'_{\text{fit}}(k_{\text{True}}^*)}{\sum_{k_{\text{True}}^*} M_{k_{\text{Rec}}^*, k_{\text{True}}^*}}$$

530 3. Finally, the non-flat background correction is applied, and the final fit function is obtained

$$531 - C_{\text{Fit}}(k_{\text{Rec}}^*) = C'_{\text{Fit}}(k_{\text{Rec}}^*) * F_{\text{Bgd}}(k_{\text{Rec}}^*)$$

532 Figures 25, 27, and 29 (32, 34, and 36, or 39, 41, and 43), in Section 7, show experimental data with fits  
 533 for all studied centralities for  $\Lambda K_S^0$  with  $\bar{\Lambda} K_S^0$ ,  $\Lambda K^+$  with  $\bar{\Lambda} K^-$ , and  $\Lambda K^-$  with  $\bar{\Lambda} K^+$ , respectively. In the  
 534 figures, the black solid line represents the “raw” fit, i.e. not corrected for momentum resolution effects  
 535 nor non-flat background. The green line shows the fit to the non-flat background. The purple points  
 536 show the fit after momentum resolution, non-flat background, and residual correlations (if applicable)  
 537 corrections have been applied. The initial values of the parameters is listed, as well as the final fit values  
 538 with uncertainties.

### 539 5.7 Coulomb Fitter

540 When fitting the  $\Xi^-(\bar{\Xi}^+)K^\pm$  results, it is necessary to include both strong and Coulomb effects. In this  
 541 case, Equation 5 is no longer valid, and, in fact, there is no analytical form with which to fit. Therefore,  
 542 we must begin with the wave function describing the pair interaction, and simulate many particle pairs  
 543 to obtain a theoretical fit correlation function. The code developed to achieve this functionality is called  
 544 “CoulombFitter”. Currently, in order to generate the statistics needed for a stable fit, we find that  $\sim 10^4$   
 545 simulated pairs per 10 MeV bin are necessary. Unfortunately, the nature of this process means that the  
 546 “CoulombFitter” takes much longer to run than the “LednickyFitter” of Section 5.1.

547 Unfortunately, with this analysis, we are not sensitive to, and therefore not able to distinguish between,  
 548 the iso-spin singlet and triplet states. We proceed with our analysis, but the results must be interpreted  
 549 as iso-spin averaged scattering parameters.

550 As stated before, to generate a fit correlation function, we must simulate a large number of pairs, calculate  
 551 the wave-function, and average  $\Psi^2$  over all pairs in a given  $k^*$  bin. Essentially, we calculate Equation 9  
 552 by hand:

$$\begin{aligned} C(\mathbf{k}^*) &= \sum_S \rho_S \int S(\mathbf{r}^*) |\Psi_{\mathbf{k}^*}^S(\mathbf{r}^*)|^2 d^3 \mathbf{r}^* \\ &\longrightarrow C(|\mathbf{k}^*|) \equiv C(k^*) = \sum_S \rho_S \langle |\Psi^S(\mathbf{k}_i^*, \mathbf{r}_i^*)|^2 \rangle_i \\ &\longrightarrow C(k^*) = \lambda \sum_S \rho_S \langle |\Psi^S(\mathbf{k}_i^*, \mathbf{r}_i^*)|^2 \rangle_i + (1 - \lambda) \end{aligned} \quad (22)$$

553 where  $\langle \rangle_i$  represents an average over all pairs in a given  $k^*$  bin.

554 In summary, for a given  $k^*$  bin, we must draw  $N_{\text{pairs}} \sim 10^4$  pairs, and for each pair:

- 555 1. Draw a random  $\mathbf{r}^*$  vector according to our Gaussian source distribution  $S(\mathbf{r}^*)$
- 556 2. Draw a random  $\mathbf{k}^*$  vector satisfying the  $|\mathbf{k}^*|$  restriction of the bin

- 557        – We draw from real  $k^*$  vectors obtained from the data  
 558        – However, we find that drawing from a distribution flat in  $k^*$  gives similar results

559        3. Construct the wave-function  $\Psi$

560 After all pairs for a given  $k^*$  bin are simulated and wave-functions obtained, the results are averaged to  
 561 give the fit result.

562 Construction of the wave-functions, Equation 10, involves a number of complex functions not included  
 563 in standard C++ or ROOT libraries (namely,  $h(\eta)$ ,  $\tilde{G}(\rho, \eta)$ , and  $F(-i\eta, 1, i\xi)$ ). These functions were  
 564 even difficult to find and implement from elsewhere. Our solution was to embed a Mathematica kernel  
 565 into our C++ code to evaluate these functions. However, having Mathematica work on-the-fly with the  
 566 fitter was far too time consuming (fitter would have taken day, maybe weeks to finish). Our solution  
 567 was to use Mathematica to create matrices representing these functions for different parameter values.  
 568 During fitting, these matrices were then interpolated and the results used to build the wave-functions.  
 569 This method decreased the running time dramatically, and we are not able to generate results in under  $\sim$   
 570 1 hour. This process will be explained in more detail in future versions of the note.

571 **6 Systematic Errors**

572 In order to understand my systematic uncertainties, the analysis code was run many times using slightly  
 573 different values for a number of important cuts, and the results were compared.

574 In order to quantify the systematic errors on the data, all correlation functions built using all varied cut  
 575 values were bin-by-bin averaged, and the resulting variance of each bin was taken as the systematic error.  
 576 The cuts which were utilized in this study are presented in Sections 6.1.1 ( $\Lambda K_S^0$ ) and 6.2.1 ( $\Lambda K^\pm$ ).

577 Similarly, the fit parameters extracted from all of these correlation functions were averaged, and the  
 578 resulting variances were taken as the systematic errors for the fit parameters. As with the systematic  
 579 errors on the data, this was performed for all varied cut values. Additionally, a systematic analysis was  
 580 done on our fit method (which, for now, just includes our choice of fit range). These two sources of  
 581 uncertainty were combined in quadrature to obtain the final systematic uncertainties on the extracted fit  
 582 parameters.

583 **6.1 Systematic Errors:  $\Lambda K_S^0$**

584 **6.1.1 Particle and Pair Cuts**

585 The cuts included in the systematic study, as well as the values used in the variations, are listed below.  
 586 Note, the central value corresponds to that used in the analysis.

- 587        1. DCA  $\Lambda(\bar{\Lambda})$ : {4, 5, 6 mm}  
 588        2. DCA  $K_S^0$ : {2, 3, 4 mm}  
 589        3. DCA  $\Lambda(\bar{\Lambda})$  Daughters: {3, 4, 5 mm}  
 590        4. DCA  $K_S^0$  Daughters: {2, 3, 4 mm}  
 591        5.  $\Lambda(\bar{\Lambda})$  Cosine of Pointing Angle: {0.9992, 0.9993, 0.9994}  
 592        6.  $K_S^0$  Cosine of Pointing Angle: {0.9992, 0.9993, 0.9994}  
 593        7. DCA to Primary Vertex of  $p(\bar{p})$  Daughter of  $\Lambda(\bar{\Lambda})$ : {0.5, 1, 2 mm}

- 594     8. DCA to Primary Vertex of  $\pi^-(\pi^+)$  Daughter of  $\Lambda(\bar{\Lambda})$ : {2, 3, 4 mm}
- 595     9. DCA to Primary Vertex of  $\pi^+$  Daughter of  $K_S^0$ : {2, 3, 4 mm}
- 596    10. DCA to Primary Vertex of  $\pi^-$  Daughter of  $K_S^0$ : {2, 3, 4 mm}
- 597   11. Average Separation of Like-Charge Daughters: {5, 6, 7 cm}

598   **6.1.2 Non-Flat Background**

599   We fit our non-flat background with a linear function. To study the contribution of this choice to our sys-  
 600   tematic errors, we also fit with a quadratic and Gaussian form. The resulting uncertainties are combined  
 601   with the uncertainties arising from our particle cuts.

602   **6.1.3 Fit Range**

603   Our choice of  $k^*$  fit range was varied by  $\pm 25\%$ . The resulting uncertainties in the extracted parameter  
 604   sets were combined with our uncertainties arising from our particle and pair cuts.

605   **6.2 Systematic Errors:  $\Lambda K^\pm$**

606   **6.2.1 Particle and Pair Cuts**

607   The cuts included in the systematic study, as well as the values used in the variations, are listed below.  
 608   Note, the central value corresponds to that used in the analysis.

- 609     1. DCA  $\Lambda(\bar{\Lambda})$ : {4, 5, 6 mm}
- 610     2. DCA  $\Lambda(\bar{\Lambda})$  Daughters: {3, 4, 5 mm}
- 611     3.  $\Lambda(\bar{\Lambda})$  Cosine of Pointing Angle: {0.9992, 0.9993, 0.9994}
- 612     4. DCA to Primary Vertex of  $p(\bar{p})$  Daughter of  $\Lambda(\bar{\Lambda})$ : {0.5, 1, 2 mm}
- 613     5. DCA to Primary Vertex of  $\pi^-(\pi^+)$  Daughter of  $\Lambda(\bar{\Lambda})$ : {2, 3, 4 mm}
- 614     6. Average Separation of  $\Lambda(\bar{\Lambda})$  Daughter with Same Charge as  $K^\pm$ : {7, 8, 9 cm}
- 615     7. Max. DCA to Primary Vertex in Transverse Plane of  $K^\pm$ : {1.92, 2.4, 2.88}
- 616     8. Max. DCA to Primary Vertex in Longitudinal Direction of  $K^\pm$ : {2.4, 3.0, 3.6}

617   **6.2.2 Non-Flat Background**

618   We fit our non-flat background with a linear function. To study the contribution of this choice to our sys-  
 619   tematic errors, we also fit with a quadratic and Gaussian form. The resulting uncertainties are combined  
 620   with the uncertainties arising from our particle cuts.

621   **6.2.3 Fit Range**

622   Our choice of  $k^*$  fit range was varied by  $\pm 25\%$ . The resulting uncertainties in the extracted parameter  
 623   sets were combined with our uncertainties arising from our particle and pair cuts.

---

## 624 6.3 Systematic Errors: $\Xi K^\pm$

### 625 6.3.1 Particle and Pair Cuts

626 The cuts included in the systematic study, as well as the values used in the variations, are listed below.  
 627 Note, the central value corresponds to that used in the analysis.

- 628 1. Max. DCA  $\Xi(\bar{\Xi})$ : {2, 3, 4 mm}
- 629 2. Max. DCA  $\Xi(\bar{\Xi})$  Daughters: {2, 3, 4 mm}
- 630 3. Min.  $\Xi(\bar{\Xi})$  Cosine of Pointing Angle to Primary Vertex: {0.9991, 0.9992, 0.9993}
- 631 4. Min.  $\Lambda(\bar{\Lambda})$  Cosine of Pointing Angle to  $\Xi(\bar{\Xi})$  Decay Vertex: {0.9992, 0.9993, 0.9994}
- 632 5. Min. DCA Bachelor  $\pi$ : {0.5, 1, 2 mm}
- 633 6. Min. DCA  $\Lambda(\bar{\Lambda})$ : {1, 2, 3 mm}
- 634 7. Max. DCA  $\Lambda(\bar{\Lambda})$  Daughters: {3, 4, 5 mm}
- 635 8. Min. DCA to Primary Vertex of  $p(\bar{p})$  Daughter of  $\Lambda(\bar{\Lambda})$ : {0.5, 1, 2 mm}
- 636 9. Min. DCA to Primary Vertex of  $\pi^-(\pi^+)$  Daughter of  $\Lambda(\bar{\Lambda})$ : {2, 3, 4 mm}
- 637 10. Min. Average Separation of  $\Lambda(\bar{\Lambda})$  Daughter and  $K^\pm$  with like charge: {7, 8, 9 cm}
- 638 11. Min. Average Separation of Bachelor  $\pi$  and  $K^\pm$  with like charge: {7, 8, 9 cm}
- 639 12. Max. DCA to Primary Vertex in Transverse Plane of  $K^\pm$ : {1.92, 2.4, 2.88}
- 640 13. Max. DCA to Primary Vertex in Longitudinal Direction of  $K^\pm$ : {2.4, 3.0, 3.6}

## 641 7 Results and Discussion

### 642 7.1 Results: $\Delta K_S^0$ and $\Delta K^\pm$

643 I first collect all of the summary results, and will show the actual fits to the data in Sections 7.1.1, 7.1.2,  
 644 and 7.1.3. In the first of the summary plots, we show the extracted scattering parameters in the form of a  
 645  $\text{Im}[f_0]$  vs  $\text{Re}[f_0]$  plot, which includes the  $d_0$  values to the right side. The next three summary plots show  
 646 the  $\lambda$  vs. Radius parameters. The first group of plots shows: 1) results without any residual correlations  
 647 included in the fit (marked as "QM 2017"), 2) results with 10 residual pairs included, and 3) results  
 648 with 3 residual pairs included. The second group of plots also includes the case where we fixed the  $d_0$   
 649 parameter to zero.

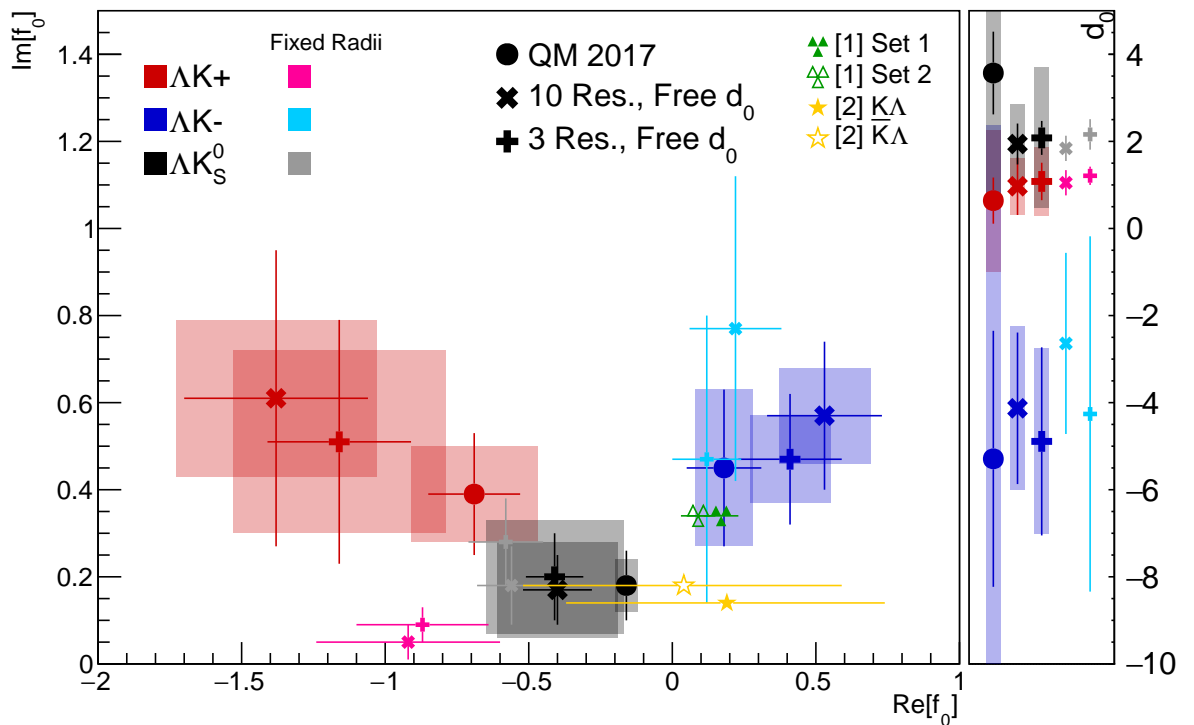


**Fig. 21:** Extracted scattering parameter results,  $\text{Im}[f_0]$  vs.  $\text{Re}[f_0]$ , together with  $d_0$  to the right, for all of our  $\Lambda K$  systems. The plot shows results including no residuals (circles), 10 residual pairs ( $\times$ ), and 3 residual pairs (+). The lighter color markers (pink, sky blue, gray) show the extracted parameters when we fix the radii to roughly align with the  $m_T$ -scaling plot, Fig. 31. The green [9] and yellow [10] points show theoretical predictions made using chiral perturbation theory. Note,  $\Lambda K^+$  on the plot is shorthand for  $\Lambda K^+$  and  $\bar{\Lambda} K^-$ , and similar for the others.

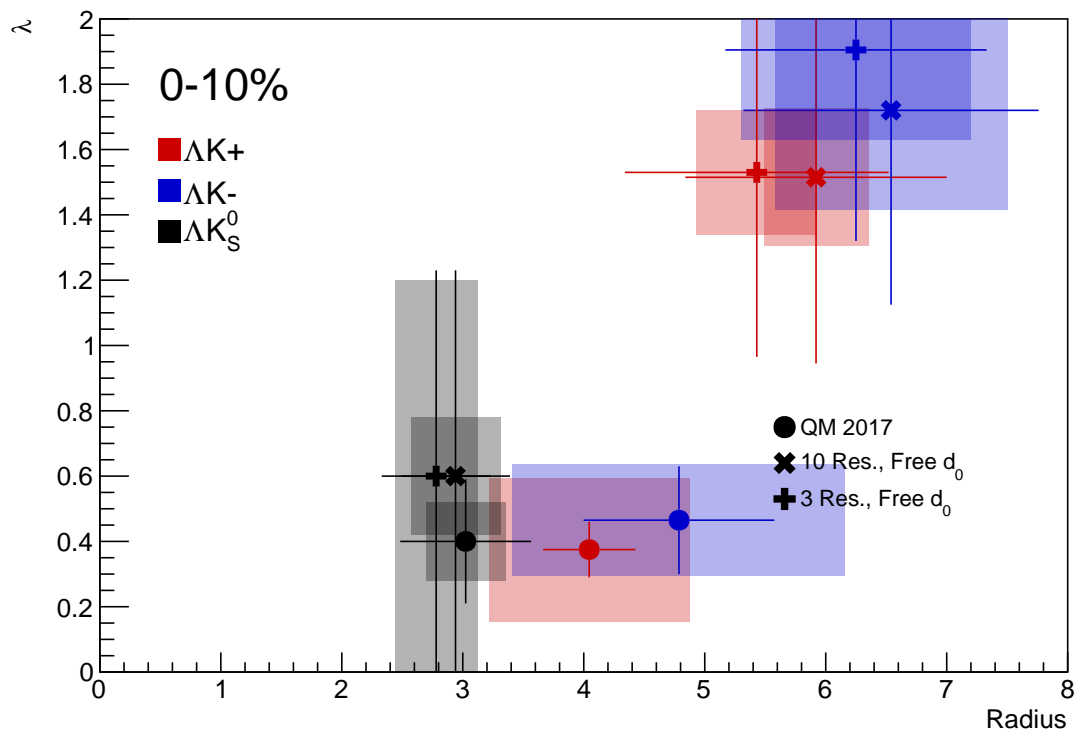


**Fig. 22:** Extracted  $\lambda$  vs Radius results, for the 0-10% centrality bin, for all of our  $\Lambda K^+$  systems. The plot shows results including no residuals (circles), 10 residual pairs (X), and 3 residual pairs (+). Note,  $\Lambda K^+$  on the plot is shorthand for  $\Lambda K^+$  and  $\bar{\Lambda} K^-$ , and similar for the others.

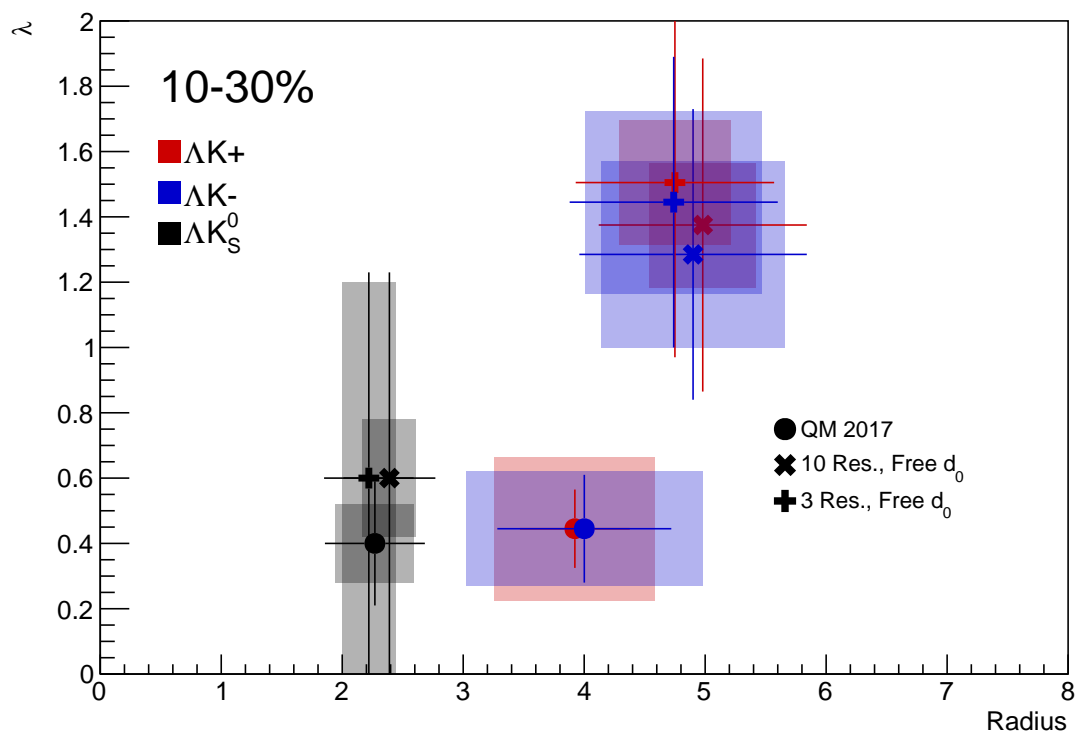


**Fig. 23:** Extracted  $\lambda$  vs Radius results, for the 10-30% centrality bin, for all of our  $\Lambda$ K systems. The plot shows results including no residuals (circles), 10 residual pairs (X), and 3 residual pairs (+). Note,  $\Lambda\bar{K}^+$  on the plot is shorthand for  $\Lambda\bar{K}^+$  and  $\bar{\Lambda}\bar{K}^-$ , and similar for the others.

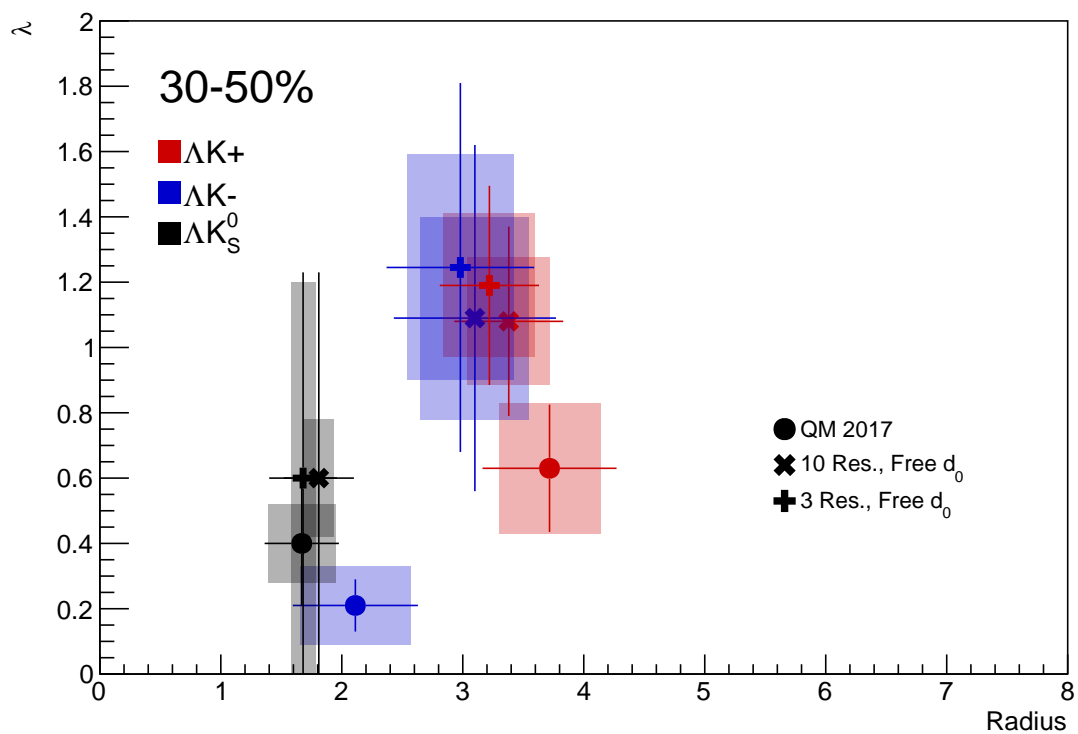


**Fig. 24:** Extracted  $\lambda$  vs Radius results, for the 30-50% centrality bin, for all of our  $\Lambda K$  systems. The plot shows results including no residuals (circles), 10 residual pairs ( $X$ ), and 3 residual pairs ( $+$ ). Note,  $\Lambda K^+$  on the plot is shorthand for  $\Lambda K^+$  and  $\bar{\Lambda} K^-$ , and similar for the others.

650 **7.1.1 Results:  $\Lambda K_S^0$  and  $\Lambda K^\pm$ : No Residual Correlations Included in Fit**

651 Figures 25, 27, and 29 (Section 7) show experimental data with fits for all studied centralities for  $\Lambda K_S^0$   
652 with  $\bar{\Lambda} K_S^0$ ,  $\Lambda K^+$  with  $\bar{\Lambda} K^-$ , and  $\Lambda K^-$  with  $\bar{\Lambda} K^+$ , respectively. The parameter sets extracted from the fits  
653 can be found in Tables ?? and ???. All correlation functions were normalized in the range  $0.32 < k^* <$   
654  $0.40 \text{ GeV}/c$ , and fit in the range  $0.0 < k^* < 0.30 \text{ GeV}/c$ . For the  $\Lambda K^-$  and  $\bar{\Lambda} K^+$  analyses, the region  $0.19$   
655  $< k^* < 0.23 \text{ GeV}/c$  was excluded from the fit to exclude the bump caused by the  $\Omega^-$  resonance. The  
656 non-flat background was fit with a linear form from  $0.6 < k^* < 0.9 \text{ GeV}/c$ . The theoretical fit function  
657 was then multiplied by this background during the fitting process.

658 In the figures (25, 27, and 29), the black solid line represents the “raw” fit, i.e. not corrected for momen-  
659 tum resolution effects nor non-flat background. The green line shows the fit to the non-flat background.  
660 The purple points show the fit after momentum resolution and non-flat background corrections have been  
661 applied. The initial values of the parameters is listed, as well as the final fit values with uncertainties.

662 For the  $\Lambda K_S^0$  fits without residuals,  $\lambda$  was restricted to [0.4, 0.6].

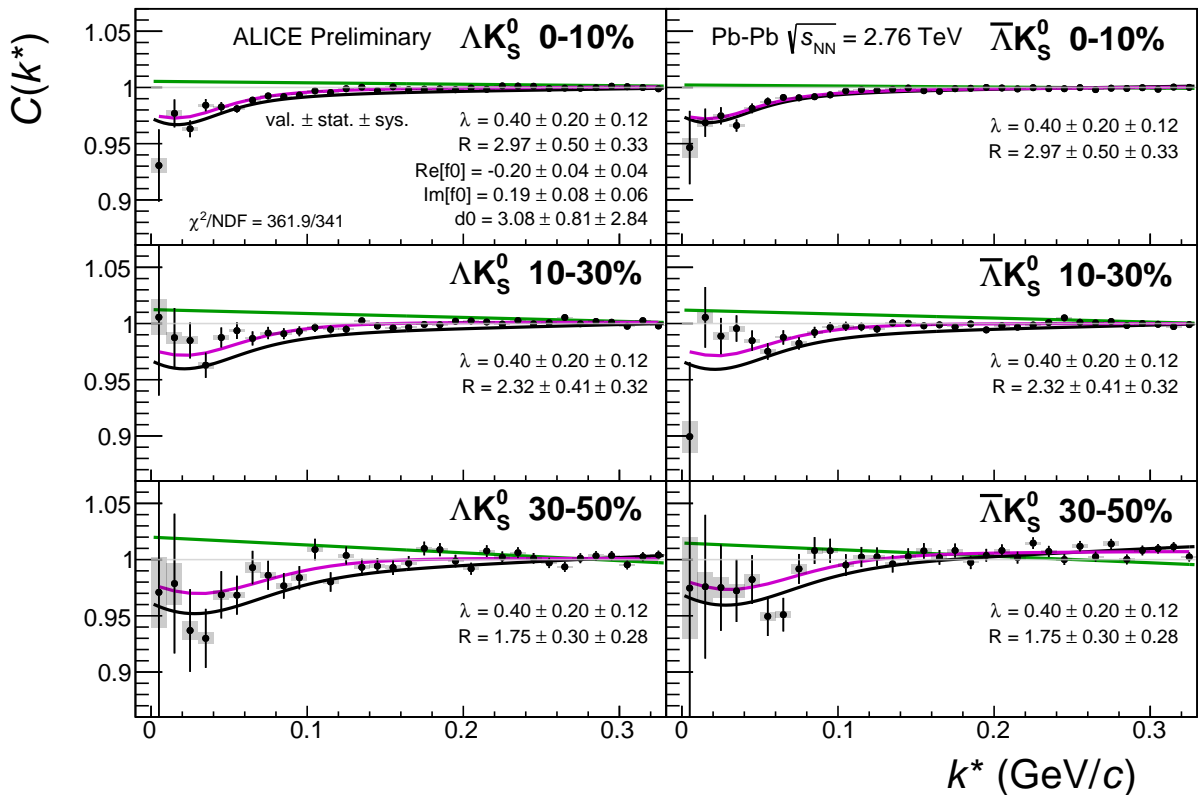


**Fig. 25:** Fits, with NO residual correlations included, to the  $\Lambda K_S^0$  (left) and  $\bar{\Lambda} K_S^0$  (right) data for the centralities 0-10% (top), 10-30% (middle), and 30-50% (bottom). The lines represent the statistical errors, while the boxes represent the systematic errors. Each has unique  $\lambda$  and normalization parameters. The radii are shared amongst like centralities; the scattering parameters ( $\mathbb{R} f_0, \mathbb{I} f_0, d_0$ ) are shared amongst all. The black solid line represents the “raw” fit, i.e. not corrected for momentum resolution effects nor non-flat background. The green line shows the fit to the non-flat background. The purple points show the fit after momentum resolution and non-flat background corrections have been applied. The initial values of the parameters is listed, as well as the final fit values with uncertainties. Here,  $R$  was restricted to [2.,10.] and  $\Lambda$  was restricted to [0.1,0.8].

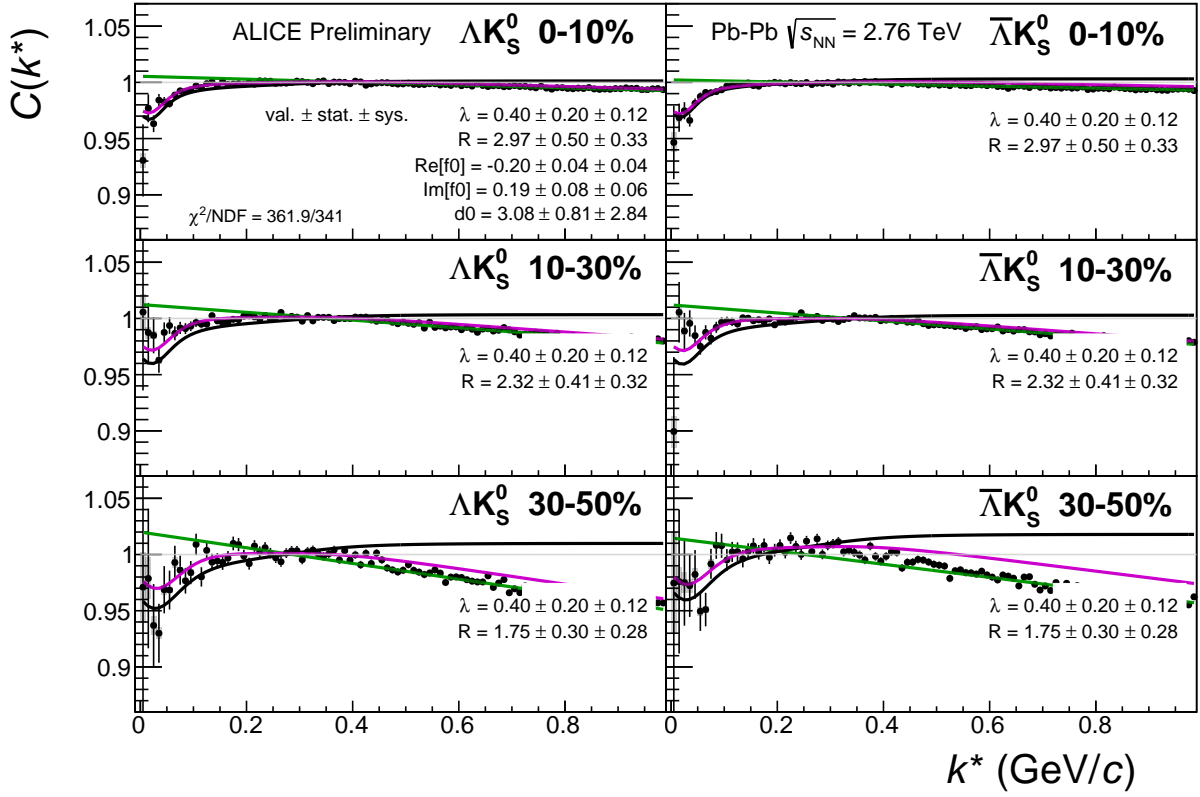


**Fig. 26:** Same as Fig. 25, but with a wider range of view. Fits, with NO residual correlations included, to the  $\Lambda K_s^0$  (left) and  $\bar{\Lambda} K_s^0$  (right) data for the centralities 0-10% (top), 10-30% (middle), and 30-50% (bottom). The lines represent the statistical errors, while the boxes represent the systematic errors. Each has unique  $\lambda$  and normalization parameters. The radii are shared amongst like centralities; the scattering parameters ( $\text{Re}[f_0]$ ,  $\text{Im}[f_0]$ ,  $d_0$ ) are shared amongst all. The black solid line represents the “raw” fit, i.e. not corrected for momentum resolution effects nor non-flat background. The green line shows the fit to the non-flat background. The purple points show the fit after momentum resolution and non-flat background corrections have been applied. The initial values of the parameters is listed, as well as the final fit values with uncertainties. Here,  $R$  was restricted to [2.,10.] and  $\Lambda$  was restricted to [0.1,0.8].

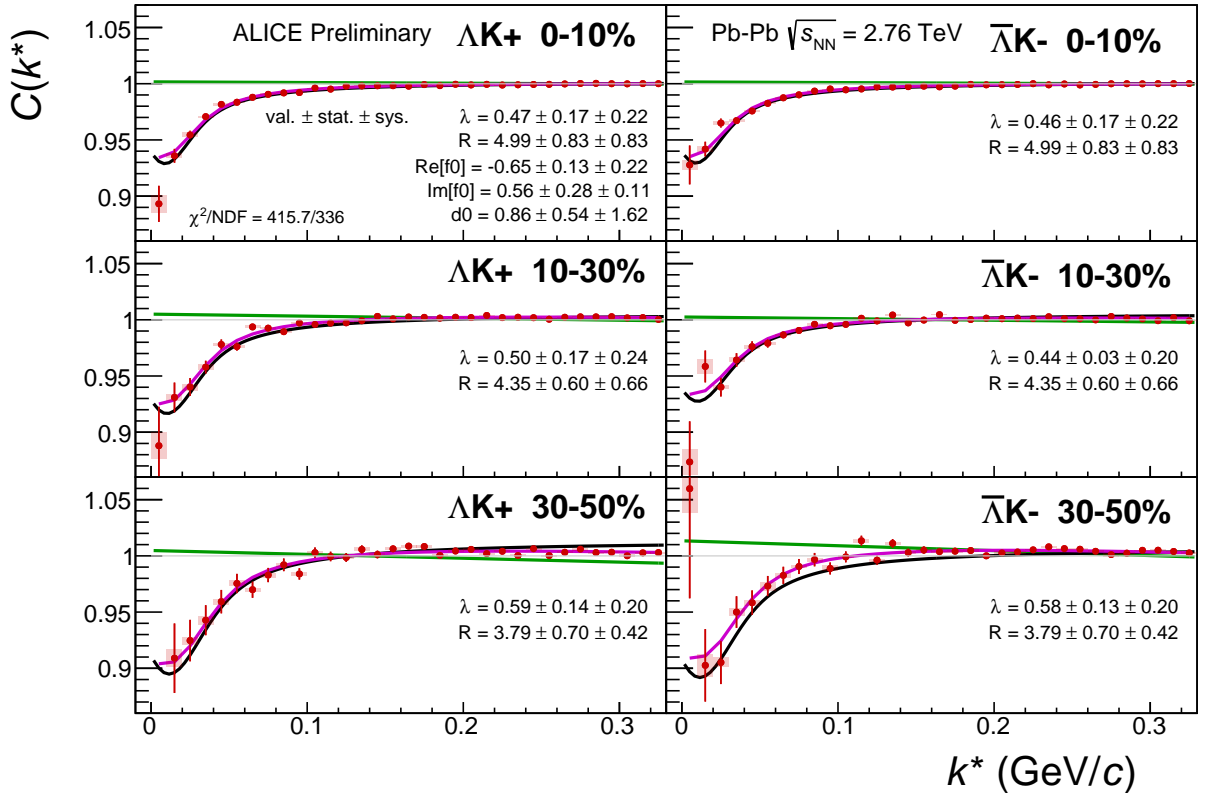


**Fig. 27:** Fits to the  $\Lambda K^+$  (left) and  $\bar{\Lambda} K^-$  (right) data for the centralities 0-10% (top), 10-30% (middle), and 30-50% (bottom). The lines represent the statistical errors, while the boxes represent the systematic errors. Each has unique  $\lambda$  and normalization parameters. The radii are shared amongst like centralities; the scattering parameters ( $\text{Re}[f_0]$ ,  $\text{Im}[f_0]$ ,  $d_0$ ) are shared amongst all. The black solid line represents the “raw” fit, i.e. not corrected for momentum resolution effects nor non-flat background. The green line shows the fit to the non-flat background. The purple points show the fit after momentum resolution and non-flat background corrections have been applied. The initial values of the parameters is listed, as well as the final fit values with uncertainties.

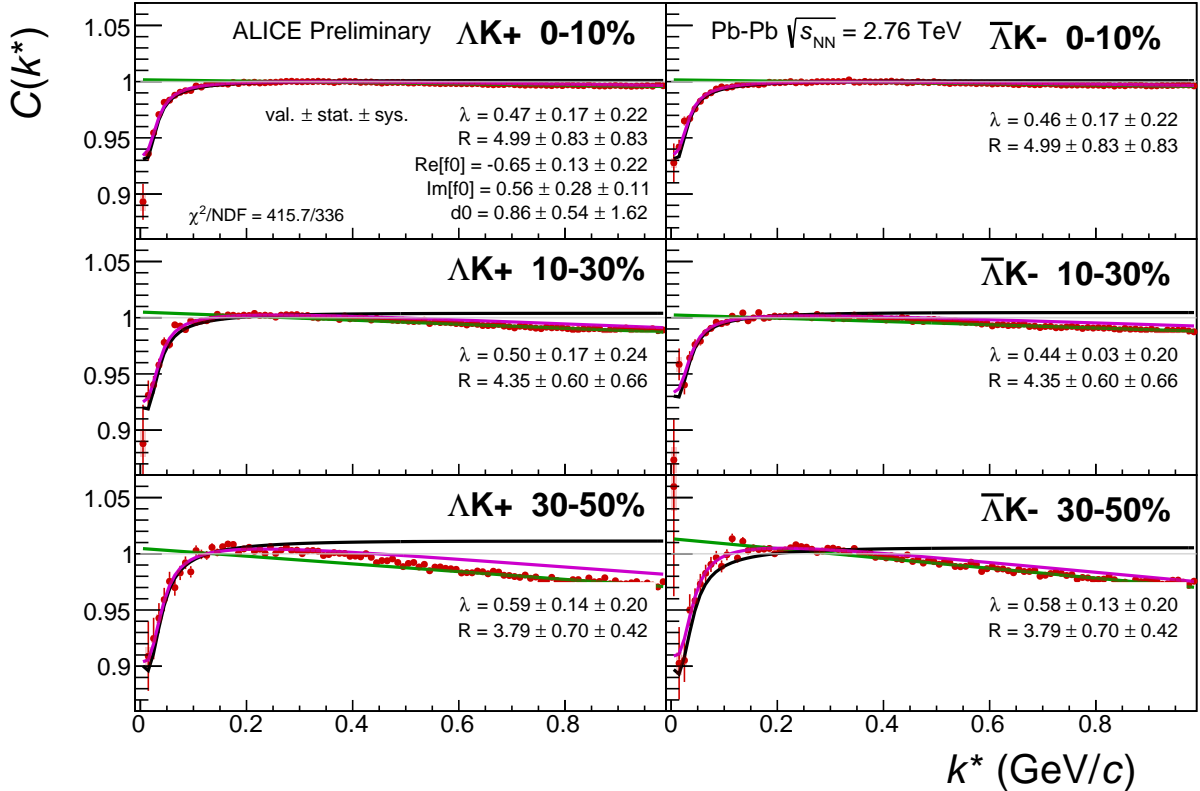


**Fig. 28:** Same as Fig. 27, but with a wider range of view. Fits, with NO residual correlations included, to the  $\Lambda K^+$  (left) and  $\bar{\Lambda}K^-$  (right) data for the centralities 0-10% (top), 10-30% (middle), and 30-50% (bottom). The lines represent the statistical errors, while the boxes represent the systematic errors. Each has unique  $\lambda$  and normalization parameters. The radii are shared amongst like centralities; the scattering parameters ( $\text{Re}[f_0]$ ,  $\text{Im}[f_0]$ ,  $d_0$ ) are shared amongst all. The black solid line represents the “raw” fit, i.e. not corrected for momentum resolution effects nor non-flat background. The green line shows the fit to the non-flat background. The purple points show the fit after momentum resolution and non-flat background corrections have been applied. The initial values of the parameters is listed, as well as the final fit values with uncertainties.

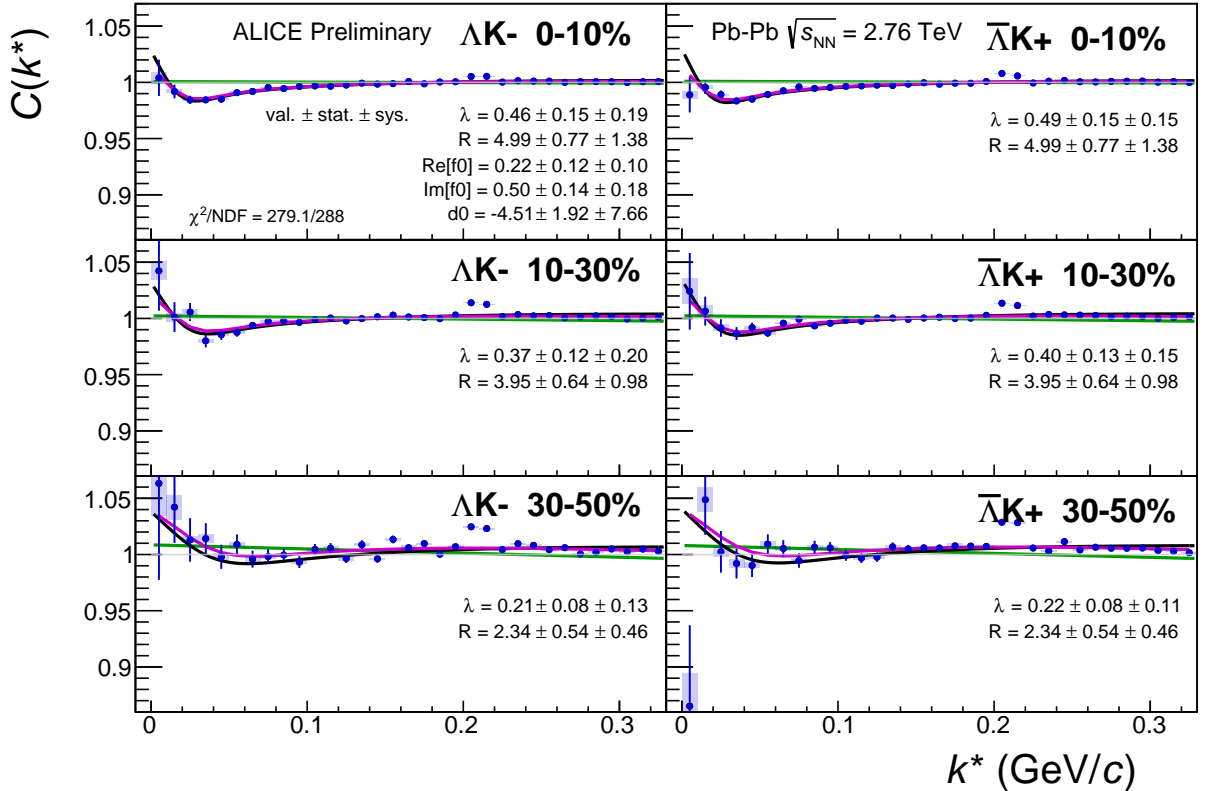


**Fig. 29:** Fits, with NO residual correlations included, to the  $\Lambda K^-$  (left) with  $\bar{\Lambda} K^+$  (right) data for the centralities 0-10% (top), 10-30% (middle), and 30-50% (bottom). The lines represent the statistical errors, while the boxes represent the systematic errors. Each has unique  $\lambda$  and normalization parameters. The radii are shared amongst like centralities; the scattering parameters ( $\mathbb{R}f_0$ ,  $\mathbb{I}f_0$ ,  $d_0$ ) are shared amongst all. The black solid line represents the “raw” fit, i.e. not corrected for momentum resolution effects nor non-flat background. The green line shows the fit to the non-flat background. The purple points show the fit after momentum resolution and non-flat background corrections have been applied. The initial values of the parameters is listed, as well as the final fit values with uncertainties.

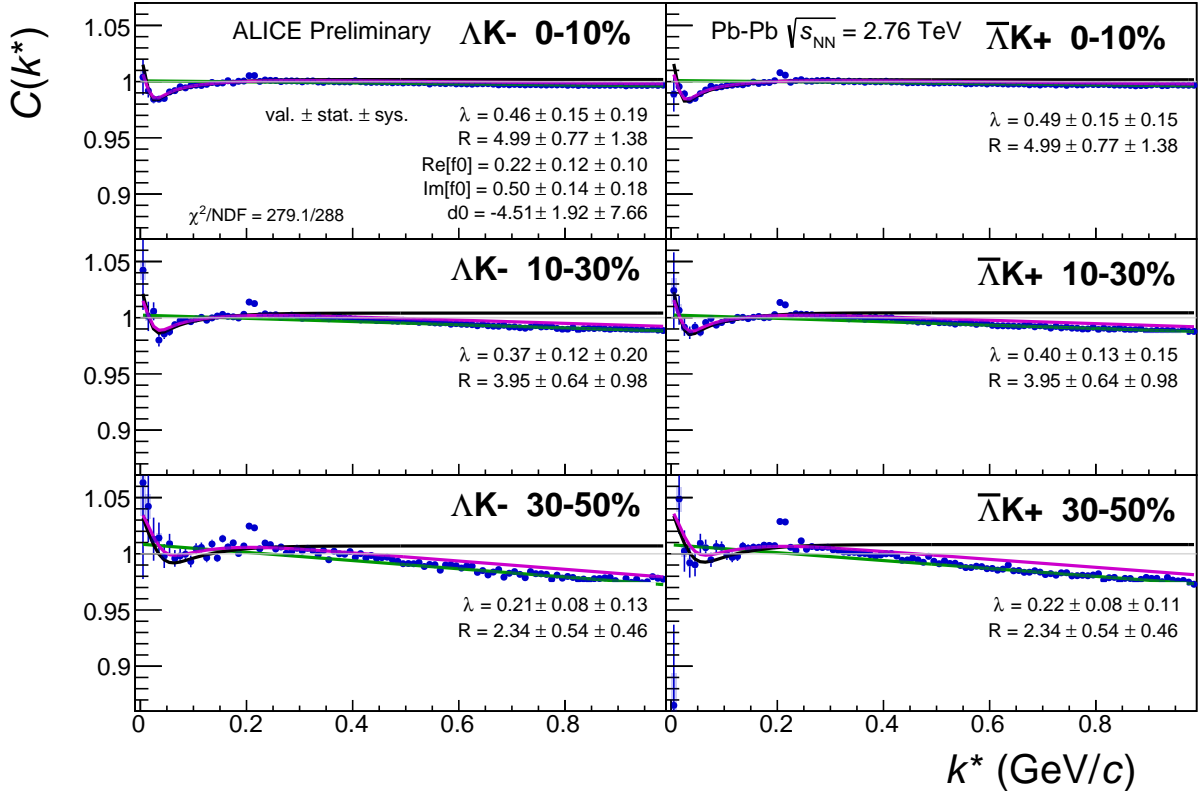


**Fig. 30:** Same as Fig. 29, but with a wider range of view. Fits, with NO residual correlations included, to the  $\Lambda K^-$  (left) with  $\bar{\Lambda} K^+$  (right) data for the centralities 0-10% (top), 10-30% (middle), and 30-50% (bottom). The lines represent the statistical errors, while the boxes represent the systematic errors. Each has unique  $\lambda$  and normalization parameters. The radii are shared amongst like centralities; the scattering parameters ( $\mathbb{R}f_0$ ,  $\mathbb{I}f_0$ ,  $d_0$ ) are shared amongst all. The black solid line represents the “raw” fit, i.e. not corrected for momentum resolution effects nor non-flat background. The green line shows the fit to the non-flat background. The purple points show the fit after momentum resolution and non-flat background corrections have been applied. The initial values of the parameters is listed, as well as the final fit values with uncertainties.

		Fit Results $\Lambda(\bar{\Lambda})K_S^0$				
Pair Type	Centrality	Fit Parameters				
		$\lambda$	$R$	$\mathbb{R}f_0$	$\mathbb{I}f_0$	$d_0$
$\Lambda K_S^0$	0-10%	$0.400 \pm 0.187 \text{ (stat.)} \pm 0.116 \text{ (sys.)}$	3.024 $\pm 0.541 \text{ (stat.)} \pm 0.329 \text{ (sys.)}$	-0.157 $\pm 0.031 \text{ (stat.)} \pm 0.043 \text{ (sys.)}$	$0.176 \pm 0.077 \text{ (stat.)} \pm 0.059 \text{ (sys.)}$	$3.566 \pm 0.947 \text{ (stat.)} \pm 2.836 \text{ (sys.)}$
	10-30%		2.270 $\pm 0.413 \text{ (stat.)} \pm 0.324 \text{ (sys.)}$			
	30-50%		1.669 $\pm 0.307 \text{ (stat.)} \pm 0.280 \text{ (sys.)}$			
	0-10%		3.024 $\pm 0.541 \text{ (stat.)} \pm 0.329 \text{ (sys.)}$			
	10-30%		2.270 $\pm 0.413 \text{ (stat.)} \pm 0.324 \text{ (sys.)}$			
	30-50%		1.669 $\pm 0.307 \text{ (stat.)} \pm 0.280 \text{ (sys.)}$			
$\bar{\Lambda} K_S^0$	0-10%	$0.400 \pm 0.187 \text{ (stat.)} \pm 0.116 \text{ (sys.)}$	2.270 $\pm 0.413 \text{ (stat.)} \pm 0.324 \text{ (sys.)}$	-0.157 $\pm 0.031 \text{ (stat.)} \pm 0.043 \text{ (sys.)}$	$0.176 \pm 0.077 \text{ (stat.)} \pm 0.059 \text{ (sys.)}$	$3.566 \pm 0.947 \text{ (stat.)} \pm 2.836 \text{ (sys.)}$
	10-30%		1.669 $\pm 0.307 \text{ (stat.)} \pm 0.280 \text{ (sys.)}$			
	30-50%		2.270 $\pm 0.413 \text{ (stat.)} \pm 0.324 \text{ (sys.)}$			
	0-10%		1.669 $\pm 0.307 \text{ (stat.)} \pm 0.280 \text{ (sys.)}$			
	10-30%		2.270 $\pm 0.413 \text{ (stat.)} \pm 0.324 \text{ (sys.)}$			
	30-50%		3.024 $\pm 0.541 \text{ (stat.)} \pm 0.329 \text{ (sys.)}$			

**Table 7:** Fit Results  $\Lambda(\bar{\Lambda})K_S^0$ , with NO residual correlations included. Each pair is fit simultaneously with its conjugate (ie.  $\Lambda K_S^0$  with  $\bar{\Lambda} K_S^0$ ) across all centralities (0-10%, 10-30%, 30-50%), for a total of 6 simultaneous analyses in the fit. Each analysis has a unique  $\lambda$  and normalization parameter. The radii are shared between analyses of like centrality, as these should have similar source sizes. The scattering parameters ( $\mathbb{R}f_0$ ,  $\mathbb{I}f_0$ ,  $d_0$ ) are shared amongst all. The fit is done on the data with only statistical error bars. The errors marked as “stat.” are those returned by MINUIT. The errors marked as “sys.” are those which result from my systematic analysis (as outlined in Section 6).

		Fit Results $\Lambda(\bar{\Lambda})K^\pm$				
Pair Type	Centrality	Fit Parameters				
		$\lambda$	$R$	$\mathbb{R}f_0$	$\mathbb{I}f_0$	$d_0$
$\Lambda K^+$	0-10%	$0.400 \pm 0.187 \text{ (stat.)} \pm 0.116 \text{ (sys.)}$	0.379 $\pm 0.085 \text{ (stat.)} \pm 0.220 \text{ (sys.)}$	4.045 $\pm 0.381 \text{ (stat.)} \pm 0.830 \text{ (sys.)}$	-0.687 $\pm 0.160 \text{ (stat.)} \pm 0.223 \text{ (sys.)}$	$0.391 \pm 0.143 \text{ (stat.)} \pm 0.111 \text{ (sys.)}$
	10-30%		0.485 $\pm 0.129 \text{ (stat.)} \pm 0.241 \text{ (sys.)}$	3.923 $\pm 0.454 \text{ (stat.)} \pm 0.663 \text{ (sys.)}$		
	30-50%		0.639 $\pm 0.195 \text{ (stat.)} \pm 0.204 \text{ (sys.)}$	3.717 $\pm 0.554 \text{ (stat.)} \pm 0.420 \text{ (sys.)}$		
	0-10%		0.371 $\pm 0.083 \text{ (stat.)} \pm 0.217 \text{ (sys.)}$	4.045 $\pm 0.381 \text{ (stat.)} \pm 0.830 \text{ (sys.)}$		
	10-30%		0.411 $\pm 0.111 \text{ (stat.)} \pm 0.201 \text{ (sys.)}$	3.923 $\pm 0.454 \text{ (stat.)} \pm 0.663 \text{ (sys.)}$		
	30-50%		0.616 $\pm 0.192 \text{ (stat.)} \pm 0.203 \text{ (sys.)}$	3.717 $\pm 0.554 \text{ (stat.)} \pm 0.420 \text{ (sys.)}$		
$\bar{\Lambda} K^-$	0-10%	$0.400 \pm 0.187 \text{ (stat.)} \pm 0.116 \text{ (sys.)}$	0.453 $\pm 0.162 \text{ (stat.)} \pm 0.186 \text{ (sys.)}$	4.787 $\pm 0.788 \text{ (stat.)} \pm 1.375 \text{ (sys.)}$	0.183 $\pm 0.134 \text{ (stat.)} \pm 0.095 \text{ (sys.)}$	$0.453 \pm 0.181 \text{ (stat.)} \pm 0.184 \text{ (sys.)}$
	10-30%		0.395 $\pm 0.149 \text{ (stat.)} \pm 0.198 \text{ (sys.)}$	4.001 $\pm 0.719 \text{ (stat.)} \pm 0.978 \text{ (sys.)}$		
	30-50%		0.199 $\pm 0.077 \text{ (stat.)} \pm 0.132 \text{ (sys.)}$	2.112 $\pm 0.517 \text{ (stat.)} \pm 0.457 \text{ (sys.)}$		
	0-10%		0.479 $\pm 0.170 \text{ (stat.)} \pm 0.152 \text{ (sys.)}$	4.787 $\pm 0.788 \text{ (stat.)} \pm 1.375 \text{ (sys.)}$		
	10-30%		0.491 $\pm 0.179 \text{ (stat.)} \pm 0.148 \text{ (sys.)}$	4.001 $\pm 0.719 \text{ (stat.)} \pm 0.978 \text{ (sys.)}$		
	30-50%		0.224 $\pm 0.083 \text{ (stat.)} \pm 0.106 \text{ (sys.)}$	2.112 $\pm 0.517 \text{ (stat.)} \pm 0.457 \text{ (sys.)}$		
$\Lambda K^-$	0-10%	$0.400 \pm 0.187 \text{ (stat.)} \pm 0.116 \text{ (sys.)}$	0.453 $\pm 0.162 \text{ (stat.)} \pm 0.186 \text{ (sys.)}$	4.787 $\pm 0.788 \text{ (stat.)} \pm 1.375 \text{ (sys.)}$	-5.292 $\pm 2.895 \text{ (stat.)} \pm 7.658 \text{ (sys.)}$	$-0.292 \pm 2.895 \text{ (stat.)} \pm 7.658 \text{ (sys.)}$
	10-30%		0.395 $\pm 0.149 \text{ (stat.)} \pm 0.198 \text{ (sys.)}$	4.001 $\pm 0.719 \text{ (stat.)} \pm 0.978 \text{ (sys.)}$		
	30-50%		0.199 $\pm 0.077 \text{ (stat.)} \pm 0.132 \text{ (sys.)}$	2.112 $\pm 0.517 \text{ (stat.)} \pm 0.457 \text{ (sys.)}$		
	0-10%		0.479 $\pm 0.170 \text{ (stat.)} \pm 0.152 \text{ (sys.)}$	4.787 $\pm 0.788 \text{ (stat.)} \pm 1.375 \text{ (sys.)}$		
	10-30%		0.491 $\pm 0.179 \text{ (stat.)} \pm 0.148 \text{ (sys.)}$	4.001 $\pm 0.719 \text{ (stat.)} \pm 0.978 \text{ (sys.)}$		
	30-50%		0.224 $\pm 0.083 \text{ (stat.)} \pm 0.106 \text{ (sys.)}$	2.112 $\pm 0.517 \text{ (stat.)} \pm 0.457 \text{ (sys.)}$		
$\bar{\Lambda} K^+$	0-10%	$0.400 \pm 0.187 \text{ (stat.)} \pm 0.116 \text{ (sys.)}$	0.453 $\pm 0.162 \text{ (stat.)} \pm 0.186 \text{ (sys.)}$	4.787 $\pm 0.788 \text{ (stat.)} \pm 1.375 \text{ (sys.)}$	-5.292 $\pm 2.895 \text{ (stat.)} \pm 7.658 \text{ (sys.)}$	$-0.292 \pm 2.895 \text{ (stat.)} \pm 7.658 \text{ (sys.)}$
	10-30%		0.395 $\pm 0.149 \text{ (stat.)} \pm 0.198 \text{ (sys.)}$	4.001 $\pm 0.719 \text{ (stat.)} \pm 0.978 \text{ (sys.)}$		
	30-50%		0.199 $\pm 0.077 \text{ (stat.)} \pm 0.132 \text{ (sys.)}$	2.112 $\pm 0.517 \text{ (stat.)} \pm 0.457 \text{ (sys.)}$		
	0-10%		0.479 $\pm 0.170 \text{ (stat.)} \pm 0.152 \text{ (sys.)}$	4.787 $\pm 0.788 \text{ (stat.)} \pm 1.375 \text{ (sys.)}$		
	10-30%		0.491 $\pm 0.179 \text{ (stat.)} \pm 0.148 \text{ (sys.)}$	4.001 $\pm 0.719 \text{ (stat.)} \pm 0.978 \text{ (sys.)}$		
	30-50%		0.224 $\pm 0.083 \text{ (stat.)} \pm 0.106 \text{ (sys.)}$	2.112 $\pm 0.517 \text{ (stat.)} \pm 0.457 \text{ (sys.)}$		

**Table 8:** Fit Results  $\Lambda(\bar{\Lambda})K^\pm$ , with NO residual correlations included. Each pair is fit simultaneously with its conjugate (ie.  $\Lambda K^+$  with  $\bar{\Lambda} K^-$  and  $\Lambda K^-$  with  $\bar{\Lambda} K^+$ ) across all centralities (0-10%, 10-30%, 30-50%), for a total of 6 simultaneous analyses in the fit. Each analysis has a unique  $\lambda$  and normalization parameter. The radii are shared between analyses of like centrality, as these should have similar source sizes. The scattering parameters ( $\mathbb{R}f_0$ ,  $\mathbb{I}f_0$ ,  $d_0$ ) are shared amongst all. The fit is done on the data with only statistical error bars. The errors marked as “stat.” are those returned by MINUIT. The errors marked as “sys.” are those which result from my systematic analysis (as outlined in Section 6).

**Fit Parameters (value  $\pm$  statistical error  $\pm$  systematic error)**

<b>Pair Type</b>	<b>Centrality</b>	<b>R</b>		
$\Lambda K^+ & \bar{\Lambda} K^-$	<b>0-10%</b>	<b><math>4.04 \pm 0.38 \pm 0.83</math></b>		
	<b>10-30%</b>	<b><math>3.92 \pm 0.45 \pm 0.66</math></b>		
	<b>30-50%</b>	<b><math>3.72 \pm 0.55 \pm 0.42</math></b>		
		<b><math>\Re f_0</math></b>	<b><math>\Im f_0</math></b>	<b><math>d_0</math></b>
		<b><math>-0.69 \pm 0.16 \pm 0.22</math></b>	<b><math>0.39 \pm 0.14 \pm 0.11</math></b>	<b><math>0.64 \pm 0.53 \pm 1.62</math></b>
$\Lambda K^- & \bar{\Lambda} K^+$	<b>0-10%</b>	<b><math>4.79 \pm 0.79 \pm 1.38</math></b>		
	<b>10-30%</b>	<b><math>4.00 \pm 0.72 \pm 0.98</math></b>		
	<b>30-50%</b>	<b><math>2.11 \pm 0.52 \pm 0.46</math></b>		
		<b><math>\Re f_0</math></b>	<b><math>\Im f_0</math></b>	<b><math>d_0</math></b>
		<b><math>0.18 \pm 0.13 \pm 0.10</math></b>	<b><math>0.45 \pm 0.18 \pm 0.18</math></b>	<b><math>-5.29 \pm 2.94 \pm 7.66</math></b>
$\Lambda K_S^0 & \bar{\Lambda} K_S^0$	<b>0-10%</b>	<b><math>3.02 \pm 0.54 \pm 0.33</math></b>		
	<b>10-30%</b>	<b><math>2.27 \pm 0.41 \pm 0.32</math></b>		
	<b>30-50%</b>	<b><math>1.67 \pm 0.30 \pm 0.28</math></b>		
		<b><math>\Re f_0</math></b>	<b><math>\Im f_0</math></b>	<b><math>d_0</math></b>
		<b><math>-0.16 \pm 0.03 \pm 0.04</math></b>	<b><math>0.18 \pm 0.08 \pm 0.06</math></b>	<b><math>3.57 \pm 0.95 \pm 2.84</math></b>

**Table 9:** Fit Results  $\Lambda(\bar{\Lambda})K^\pm$  and  $\Lambda(\bar{\Lambda})K_S^0$ , with NO residual correlations included ( $\lambda$  parameters not shown). This table is a condensed version of Tables 7 and ??

663 Figure 45 shows extracted  $R_{\text{inv}}$  parameters as a function of transverse mass ( $m_T$ ) for various pair systems  
 664 over several centralities. The published ALICE data [11] is shown with transparent, open symbols. The  
 665 new  $\Lambda K$  results are shown with opaque, filled symbols. The radii show an increasing size with increas-  
 666 ing centrality, as is expected from the simple geometric picture of the collisions. The radii decrease  
 667 in size with increasing  $m_T$ , and we see an approximate scaling of the radii with transverse mass, as is  
 668 expected in the presence of collective flow in the system.

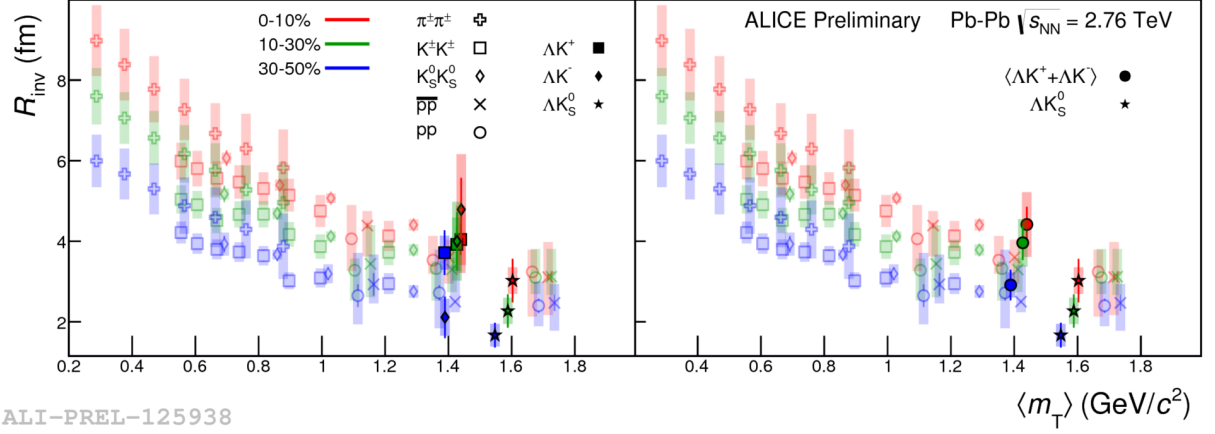


**Fig. 31:** No residual correlations in  $\Lambda K$  fits. Extracted fit  $R_{\text{inv}}$  parameters as a function of pair transverse mass ( $m_T$ ) for various pair systems over several centralities. The ALICE published data [11] is shown with transparent, open symbols. The new  $\Lambda K$  results are shown with opaque, filled symbols. In the left, the  $\Lambda K^+$  (with its conjugate pair) results are shown separately from the  $\Lambda K^-$  (with its conjugate pair) results. In the right, all  $\Lambda K^\pm$  results are averaged.

669 7.1.2 Results:  $\Lambda K_S^0$  and  $\bar{\Lambda} K_S^0$ : 3 Residual Correlations Included in Fit

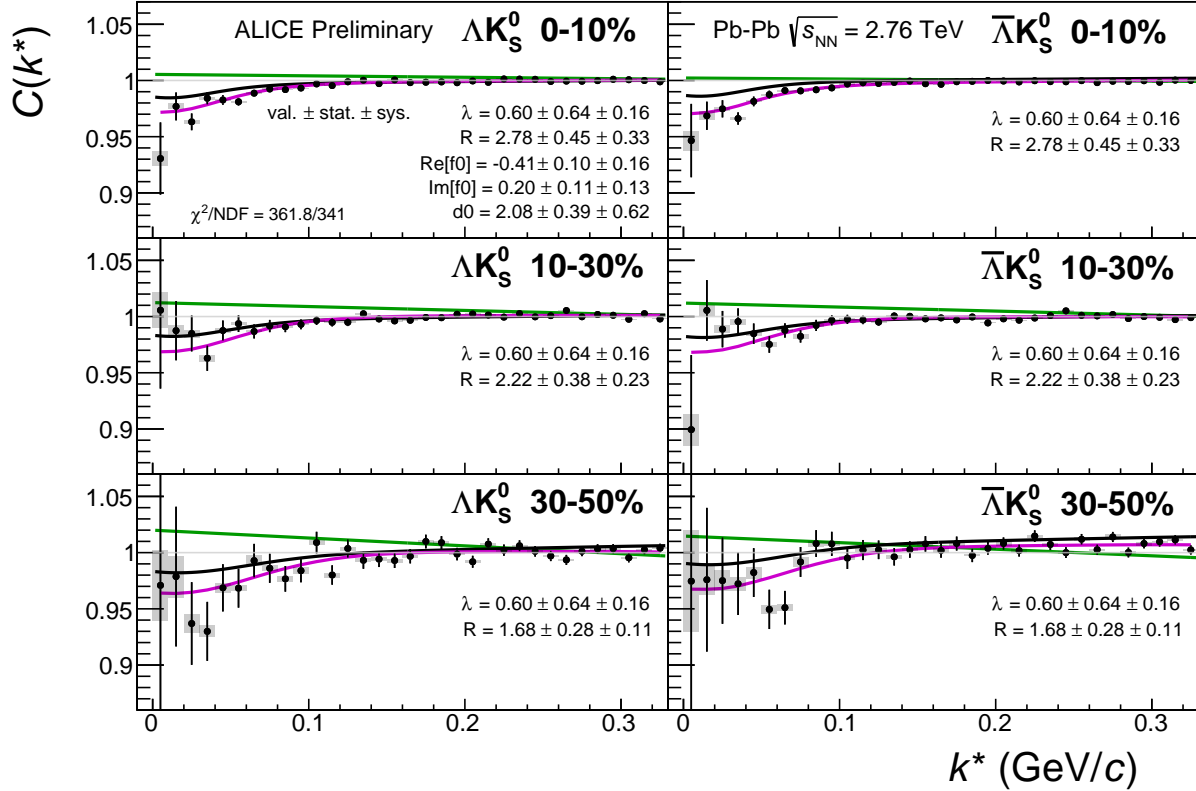


**Fig. 32:** Fits, with 3 residual correlations included, to the  $\Lambda K_S^0$  (left) and  $\bar{\Lambda} K_S^0$  (right) data for the centralities 0-10% (top), 10-30% (middle), and 30-50% (bottom). The lines represent the statistical errors, while the boxes represent the systematic errors. Each has unique  $\lambda$  and normalization parameters. The radii are shared amongst like centralities; the scattering parameters ( $\text{Re}[f_0]$ ,  $\text{Im}[f_0]$ ,  $d_0$ ) are shared amongst all. The black solid line represents the “raw” fit, i.e. not corrected for momentum resolution effects nor non-flat background. The green line shows the fit to the non-flat background. The purple points show the fit after momentum resolution and non-flat background corrections have been applied. The initial values of the parameters is listed, as well as the final fit values with uncertainties. Here,  $R$  was restricted to [2.,10.] and  $\Lambda$  was restricted to [0.1,0.8].

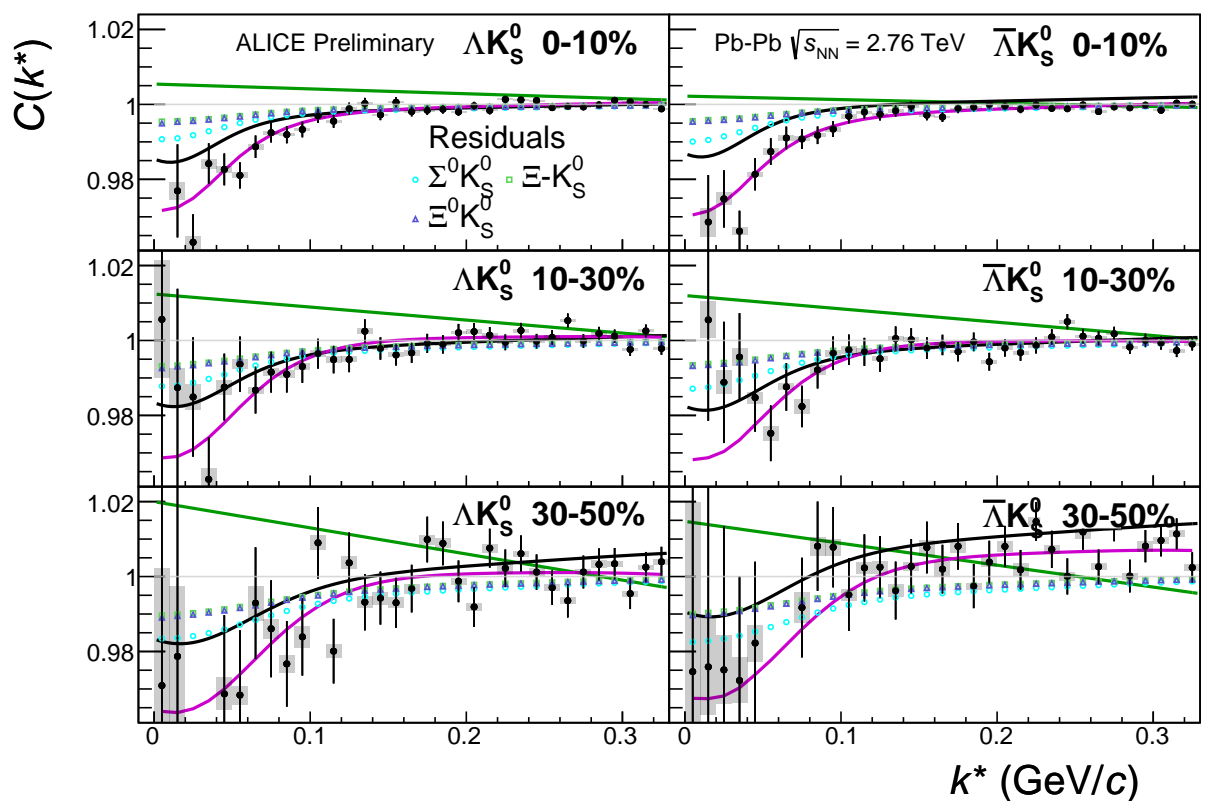


**Fig. 33:** Caption

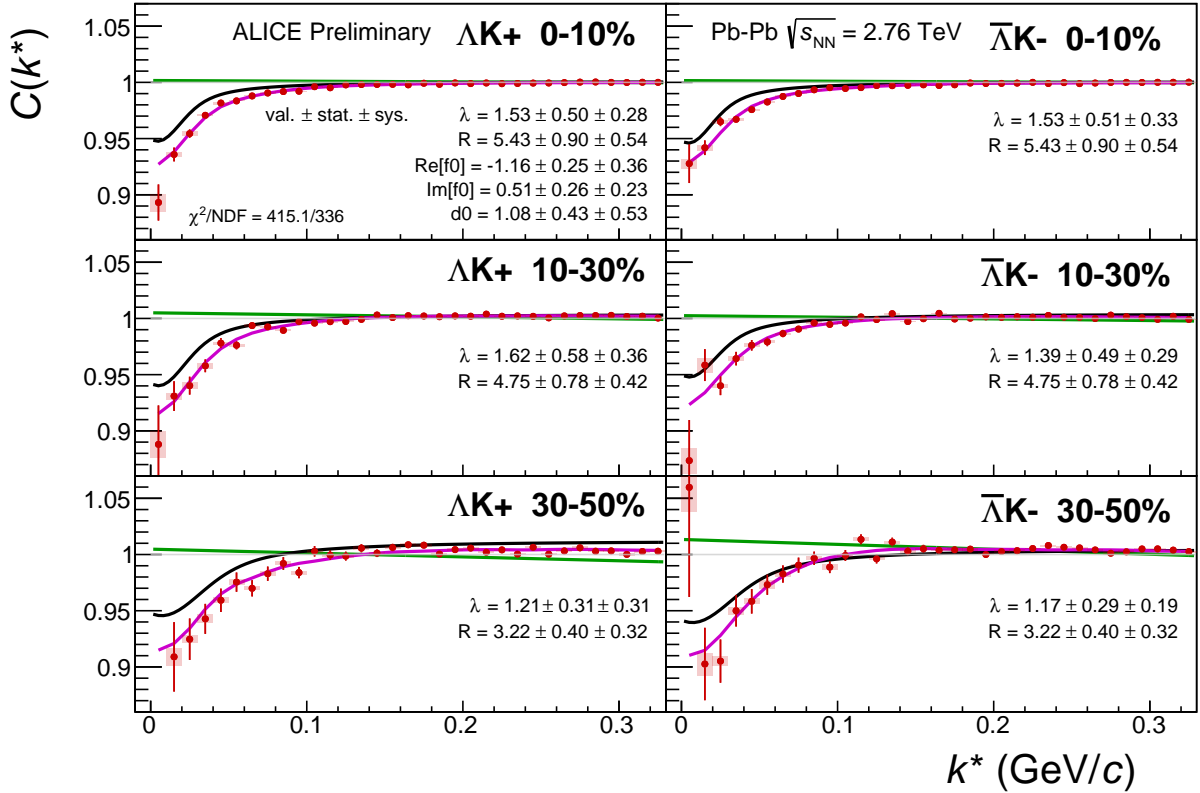


**Fig. 34:** Fits, with 3 residual correlations included, to the  $\Lambda K^+$  (left) and  $\bar{\Lambda} K^-$  (right) data for the centralities 0-10% (top), 10-30% (middle), and 30-50% (bottom). The lines represent the statistical errors, while the boxes represent the systematic errors. Each has unique  $\lambda$  and normalization parameters. The radii are shared amongst like centralities; the scattering parameters ( $\mathbb{R}f_0, \mathbb{I}f_0, d_0$ ) are shared amongst all. The black solid line represents the “raw” fit, i.e. not corrected for momentum resolution effects nor non-flat background. The green line shows the fit to the non-flat background. The purple points show the fit after momentum resolution and non-flat background corrections have been applied. The initial values of the parameters is listed, as well as the final fit values with uncertainties.

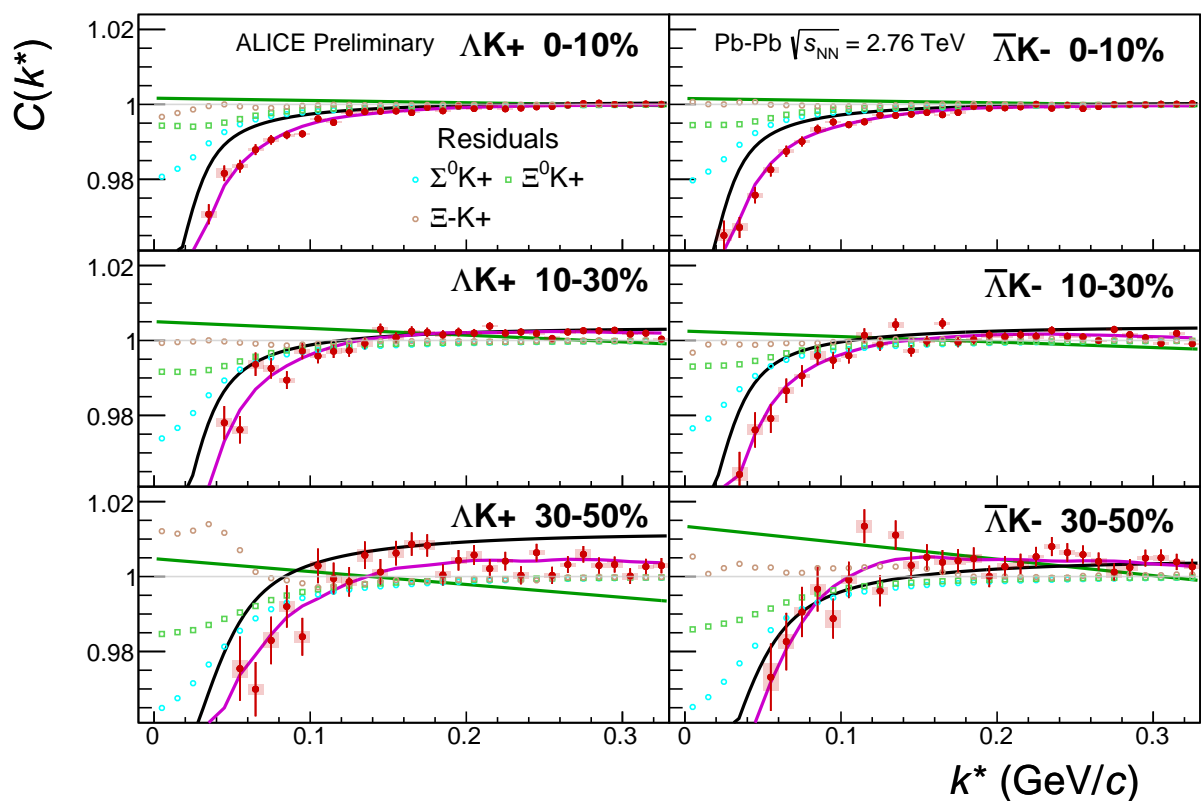


**Fig. 35:** Caption

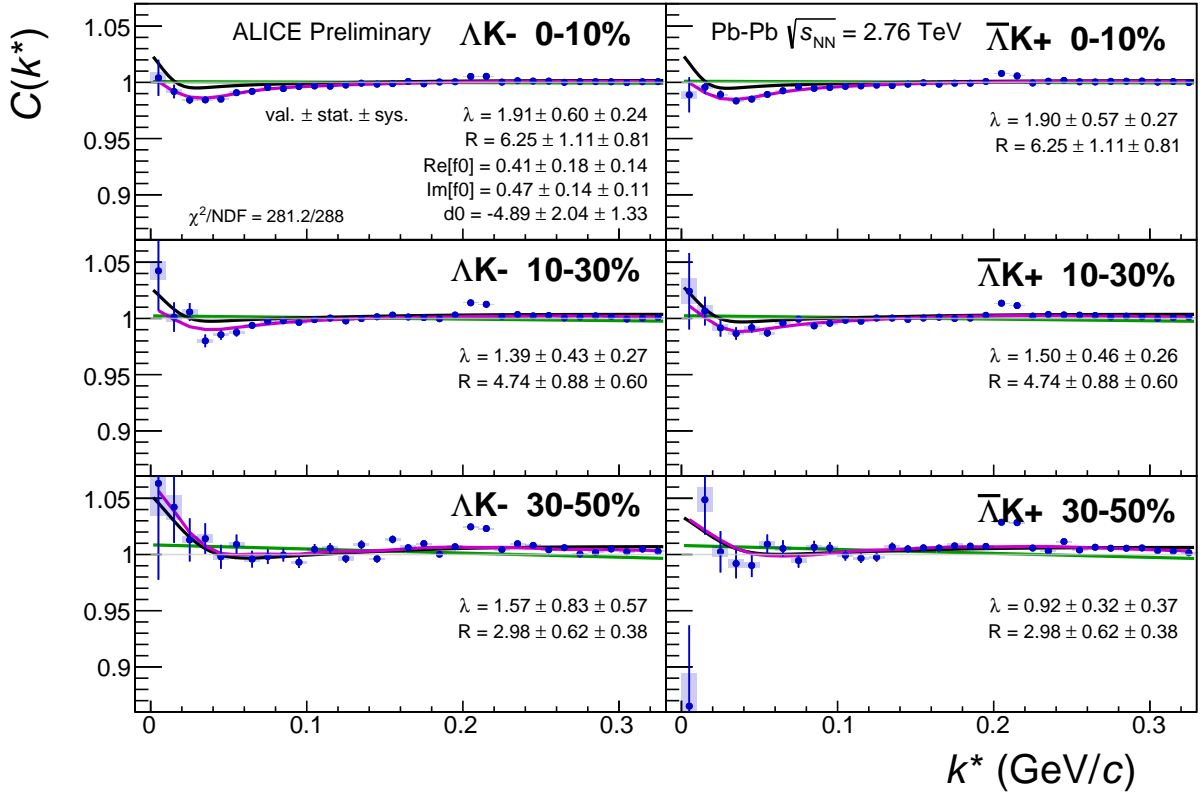


**Fig. 36:** Fits, with 3 residual correlations included, to the  $\Lambda K^-$  (left) with  $\bar{\Lambda} K^+$  (right) data for the centralities 0-10% (top), 10-30% (middle), and 30-50% (bottom). The lines represent the statistical errors, while the boxes represent the systematic errors. Each has unique  $\lambda$  and normalization parameters. The radii are shared amongst like centralities; the scattering parameters ( $\mathbb{R}f_0, \mathbb{I}f_0, d_0$ ) are shared amongst all. The black solid line represents the “raw” fit, i.e. not corrected for momentum resolution effects nor non-flat background. The green line shows the fit to the non-flat background. The purple points show the fit after momentum resolution and non-flat background corrections have been applied. The initial values of the parameters is listed, as well as the final fit values with uncertainties.

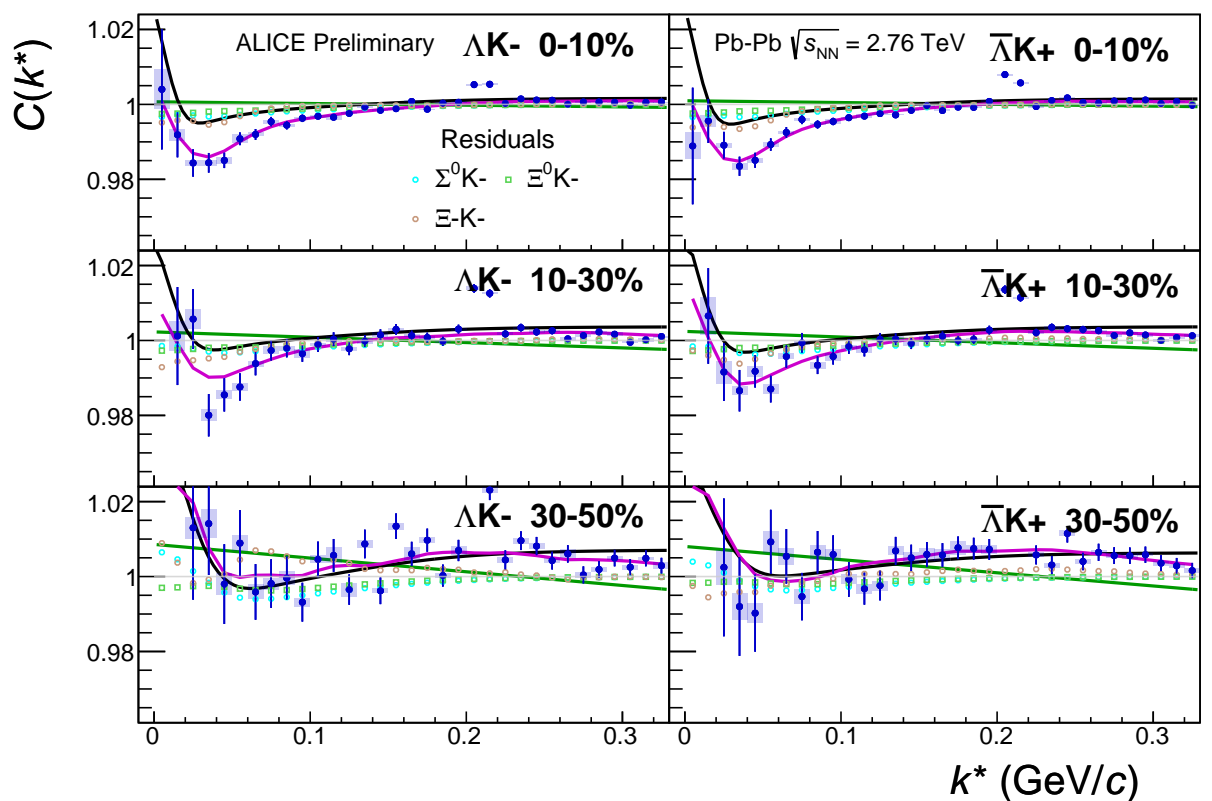


**Fig. 37:** Caption

		Fit Results $\Lambda(\bar{\Lambda})K_S^0$				
Pair Type	Centrality	Fit Parameters				
		$\lambda$	$R$	$\mathbb{R}f_0$	$\mathbb{I}f_0$	$d_0$
$\Lambda K_S^0$	0-10%	$0.60 \pm 0.63$ (stat.) $\pm 0.16$ (sys.)	$2.78 \pm 0.45$ (stat.) $\pm 0.33$ (sys.)	$-0.41 \pm 0.10$ (stat.) $\pm 0.16$ (sys.)	$0.20 \pm 0.10$ (stat.) $\pm 0.13$ (sys.)	$2.08 \pm 0.39$ (stat.) $\pm 0.62$ (sys.)
	10-30%		$2.22 \pm 0.37$ (stat.) $\pm 0.23$ (sys.)			
	30-50%		$1.68 \pm 0.28$ (stat.) $\pm 0.11$ (sys.)			
$\bar{\Lambda} K_S^0$	0-10%	$0.60 \pm 0.63$ (stat.) $\pm 0.16$ (sys.)	$2.78 \pm 0.45$ (stat.) $\pm 0.33$ (sys.)	$-0.41 \pm 0.10$ (stat.) $\pm 0.16$ (sys.)	$0.20 \pm 0.10$ (stat.) $\pm 0.13$ (sys.)	$2.08 \pm 0.39$ (stat.) $\pm 0.62$ (sys.)
	10-30%		$2.22 \pm 0.37$ (stat.) $\pm 0.23$ (sys.)			
	30-50%		$1.68 \pm 0.28$ (stat.) $\pm 0.11$ (sys.)			

**Table 10:** Fit Results  $\Lambda(\bar{\Lambda})K_S^0$ , with 3 residual correlations included. Each pair is fit simultaneously with its conjugate (ie.  $\Lambda K_S^0$  with  $\bar{\Lambda} K_S^0$ ) across all centralities (0-10%, 10-30%, 30-50%), for a total of 6 simultaneous analyses in the fit. Each analysis has a unique  $\lambda$  and normalization parameter. The radii are shared between analyses of like centrality, as these should have similar source sizes. The scattering parameters ( $\mathbb{R}f_0$ ,  $\mathbb{I}f_0$ ,  $d_0$ ) are shared amongst all. The fit is done on the data with only statistical error bars. The errors marked as “stat.” are those returned by MINUIT. The errors marked as “sys.” are those which result from my systematic analysis (as outlined in Section 6).

Fit Results $\Lambda(\bar{\Lambda})K^\pm$						
Pair Type	Centrality	Fit Parameters				
		$\lambda$	$R$	$\mathbb{R}f_0$	$\mathbb{I}f_0$	$d_0$
$\Lambda K^+$	0-10%	$1.53 \pm 0.56$ (stat.) $\pm 0.28$ (sys.)	$5.43 \pm 1.09$ (stat.) $\pm 0.54$ (sys.)	$-1.16 \pm 0.25$ (stat.) $\pm 0.36$ (sys.)	$0.51 \pm 0.28$ (stat.) $\pm 0.23$ (sys.)	$1.08 \pm 0.43$ (stat.) $\pm 0.53$ (sys.)
	10-30%	$1.62 \pm 0.58$ (stat.) $\pm 0.36$ (sys.)	$4.75 \pm 0.82$ (stat.) $\pm 0.42$ (sys.)			
	30-50%	$1.21 \pm 0.31$ (stat.) $\pm 0.31$ (sys.)	$3.22 \pm 0.41$ (stat.) $\pm 0.32$ (sys.)			
$\bar{\Lambda} K^-$	0-10%	$1.53 \pm 0.57$ (stat.) $\pm 0.33$ (sys.)	$5.43 \pm 1.09$ (stat.) $\pm 0.54$ (sys.)	$0.41 \pm 0.18$ (stat.) $\pm 0.14$ (sys.)	$0.47 \pm 0.15$ (stat.) $\pm 0.11$ (sys.)	$-4.89 \pm 2.16$ (stat.) $\pm 1.33$ (sys.)
	10-30%	$1.39 \pm 0.49$ (stat.) $\pm 0.29$ (sys.)	$4.75 \pm 0.82$ (stat.) $\pm 0.42$ (sys.)			
	30-50%	$1.17 \pm 0.30$ (stat.) $\pm 0.19$ (sys.)	$3.22 \pm 0.41$ (stat.) $\pm 0.32$ (sys.)			
$\Lambda K^-$	0-10%	$1.91 \pm 0.60$ (stat.) $\pm 0.24$ (sys.)	$6.25 \pm 1.08$ (stat.) $\pm 0.81$ (sys.)			
	10-30%	$1.39 \pm 0.43$ (stat.) $\pm 0.27$ (sys.)	$4.74 \pm 0.86$ (stat.) $\pm 0.60$ (sys.)			
	30-50%	$1.57 \pm 0.82$ (stat.) $\pm 0.57$ (sys.)	$2.98 \pm 0.61$ (stat.) $\pm 0.38$ (sys.)			
$\bar{\Lambda} K^+$	0-10%	$1.90 \pm 0.57$ (stat.) $\pm 0.27$ (sys.)	$6.25 \pm 1.08$ (stat.) $\pm 0.81$ (sys.)			
	10-30%	$1.50 \pm 0.46$ (stat.) $\pm 0.26$ (sys.)	$4.74 \pm 0.86$ (stat.) $\pm 0.60$ (sys.)			
	30-50%	$0.92 \pm 0.31$ (stat.) $\pm 0.37$ (sys.)	$2.98 \pm 0.61$ (stat.) $\pm 0.38$ (sys.)			

**Table 11:** Fit Results  $\Lambda(\bar{\Lambda})K^\pm$ , with 3 residual correlations included. Each pair is fit simultaneously with its conjugate (ie.  $\Lambda K^+$  with  $\bar{\Lambda} K^-$  and  $\Lambda K^-$  with  $\bar{\Lambda} K^+$ ) across all centralities (0-10%, 10-30%, 30-50%), for a total of 6 simultaneous analyses in the fit. Each analysis has a unique  $\lambda$  and normalization parameter. The radii are shared between analyses of like centrality, as these should have similar source sizes. The scattering parameters ( $\mathbb{R}f_0$ ,  $\mathbb{I}f_0$ ,  $d_0$ ) are shared amongst all. The fit is done on the data with only statistical error bars. The errors marked as “stat.” are those returned by MINUIT. The errors marked as “sys.” are those which result from my systematic analysis (as outlined in Section 6).

**Fit Parameters (value  $\pm$  statistical error  $\pm$  systematic error)**

<b>Pair Type</b>	<b>Centrality</b>	<b>R</b>		
$\Lambda K^+ & \bar{\Lambda} K^-$	<b>0-10%</b>		<b><math>5.43 \pm 1.09 \pm 0.54</math></b>	
	<b>10-30%</b>		<b><math>4.75 \pm 0.82 \pm 0.42</math></b>	
	<b>30-50%</b>		<b><math>3.22 \pm 0.41 \pm 0.32</math></b>	
		<b><math>\Re f_0</math></b>	<b><math>\Im f_0</math></b>	<b><math>d_0</math></b>
		<b><math>-1.16 \pm 0.25 \pm 0.36</math></b>	<b><math>0.51 \pm 0.28 \pm 0.23</math></b>	<b><math>1.08 \pm 0.43 \pm 0.53</math></b>
$\Lambda K^- & \bar{\Lambda} K^+$	<b>0-10%</b>		<b><math>6.25 \pm 1.08 \pm 0.81</math></b>	
	<b>10-30%</b>		<b><math>4.74 \pm 0.86 \pm 0.60</math></b>	
	<b>30-50%</b>		<b><math>2.98 \pm 0.61 \pm 0.38</math></b>	
		<b><math>\Re f_0</math></b>	<b><math>\Im f_0</math></b>	<b><math>d_0</math></b>
		<b><math>0.41 \pm 0.18 \pm 0.14</math></b>	<b><math>0.47 \pm 0.15 \pm 0.11</math></b>	<b><math>-4.89 \pm 2.16 \pm 1.33</math></b>
$\Lambda K_S^0 & \bar{\Lambda} K_S^0$	<b>0-10%</b>		<b><math>2.78 \pm 0.45 \pm 0.33</math></b>	
	<b>10-30%</b>		<b><math>2.22 \pm 0.37 \pm 0.23</math></b>	
	<b>30-50%</b>		<b><math>1.68 \pm 0.28 \pm 0.11</math></b>	
		<b><math>\Re f_0</math></b>	<b><math>\Im f_0</math></b>	<b><math>d_0</math></b>
		<b><math>-0.41 \pm 0.10 \pm 0.16</math></b>	<b><math>0.20 \pm 0.10 \pm 0.13</math></b>	<b><math>2.08 \pm 0.39 \pm 0.62</math></b>

**Table 12:** Fit Results  $\Lambda(\bar{\Lambda})K^\pm$  and  $\Lambda(\bar{\Lambda})K_S^0$ , with 3 residual correlations included ( $\lambda$  parameters not shown). This table is a condensed version of Tables 10 and 11

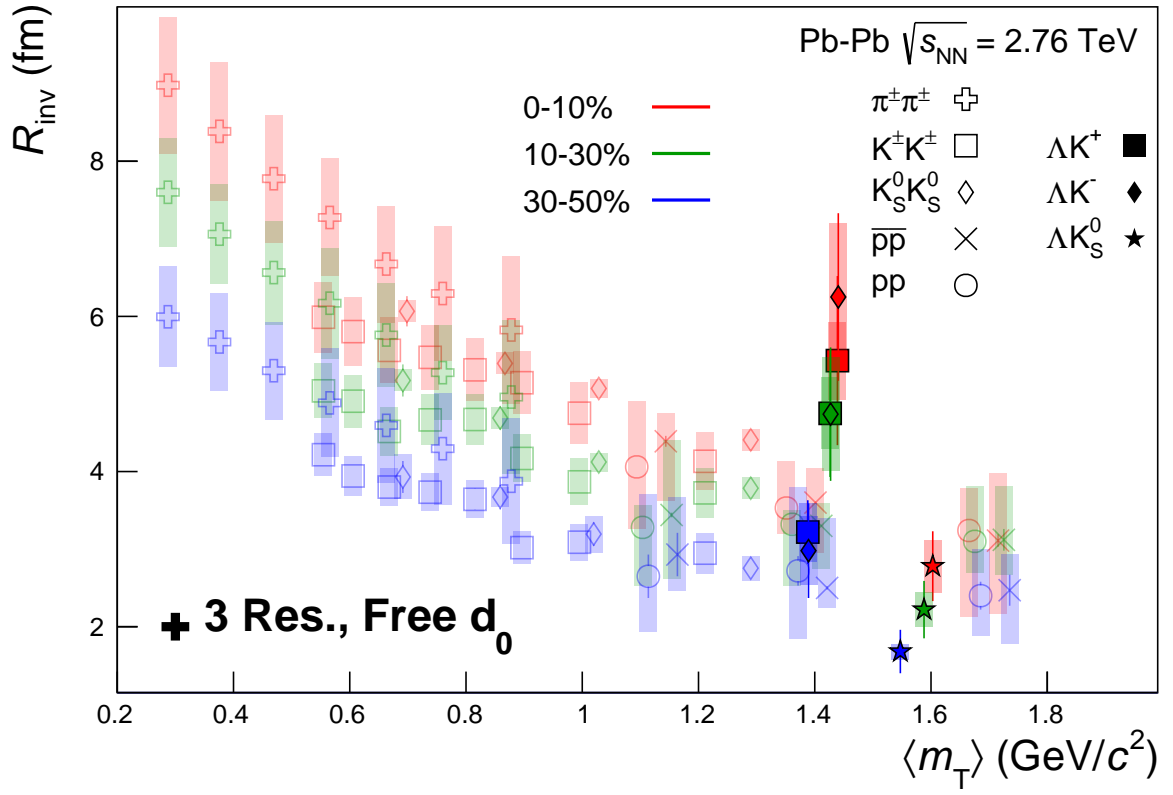


**Fig. 38:** 3 residual correlations in  $\Lambda K$  fits. Extracted fit  $R_{\text{inv}}$  parameters as a function of pair transverse mass ( $m_T$ ) for various pair systems over several centralities. The ALICE published data [11] is shown with transparent, open symbols. The new  $\Lambda K$  results are shown with opaque, filled symbols. In the left, the  $\Lambda K^+$  (with its conjugate pair) results are shown separately from the  $\Lambda K^-$  (with its conjugate pair) results. In the right, all  $\Lambda K^\pm$  results are averaged.

670 7.1.3 Results:  $\Lambda K_S^0$  and  $\bar{\Lambda} K_S^0$ : 10 Residual Correlations Included in Fit

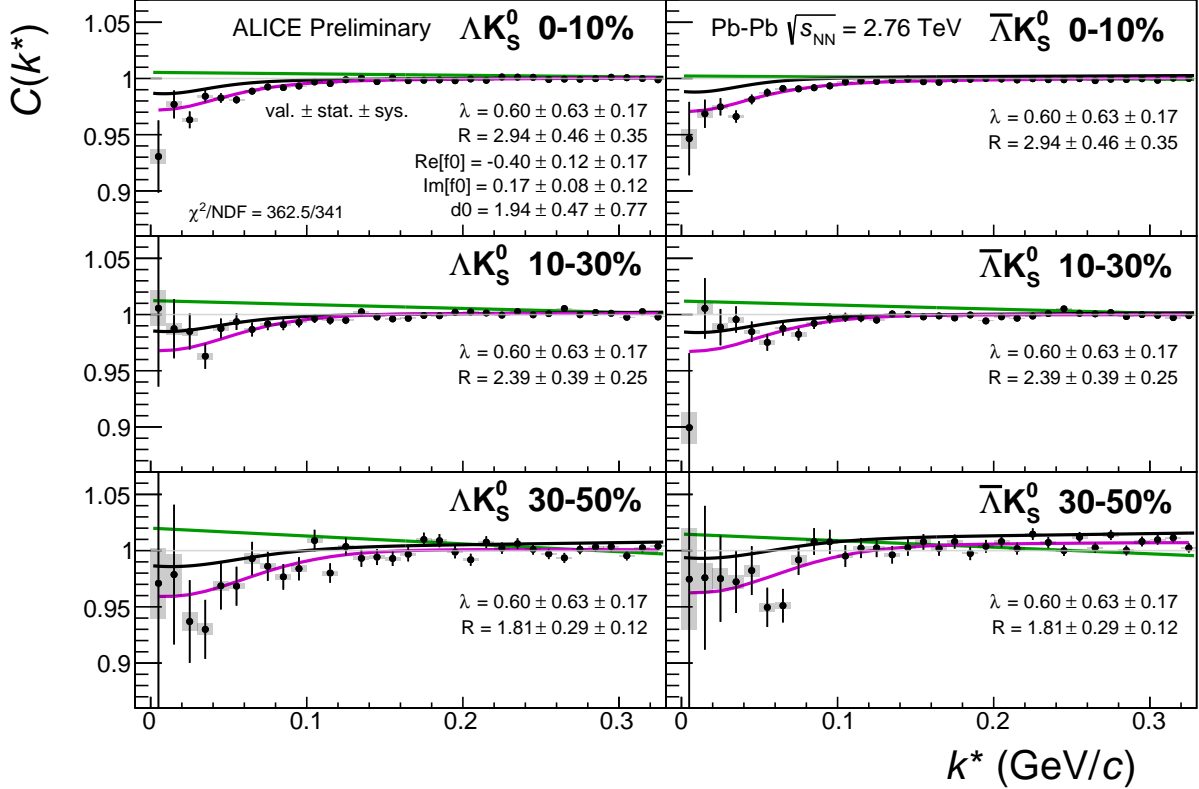


**Fig. 39:** Fits, with 10 residual correlations included, to the  $\Lambda K_S^0$  (left) and  $\bar{\Lambda} K_S^0$  (right) data for the centralities 0-10% (top), 10-30% (middle), and 30-50% (bottom). The lines represent the statistical errors, while the boxes represent the systematic errors. Each has unique  $\lambda$  and normalization parameters. The radii are shared amongst like centralities; the scattering parameters ( $\text{Re}[f_0]$ ,  $\text{Im}[f_0]$ ,  $d_0$ ) are shared amongst all. The black solid line represents the “raw” fit, i.e. not corrected for momentum resolution effects nor non-flat background. The green line shows the fit to the non-flat background. The purple points show the fit after momentum resolution and non-flat background corrections have been applied. The initial values of the parameters is listed, as well as the final fit values with uncertainties. Here,  $R$  was restricted to [2.,10.] and  $\Lambda$  was restricted to [0.1,0.8].

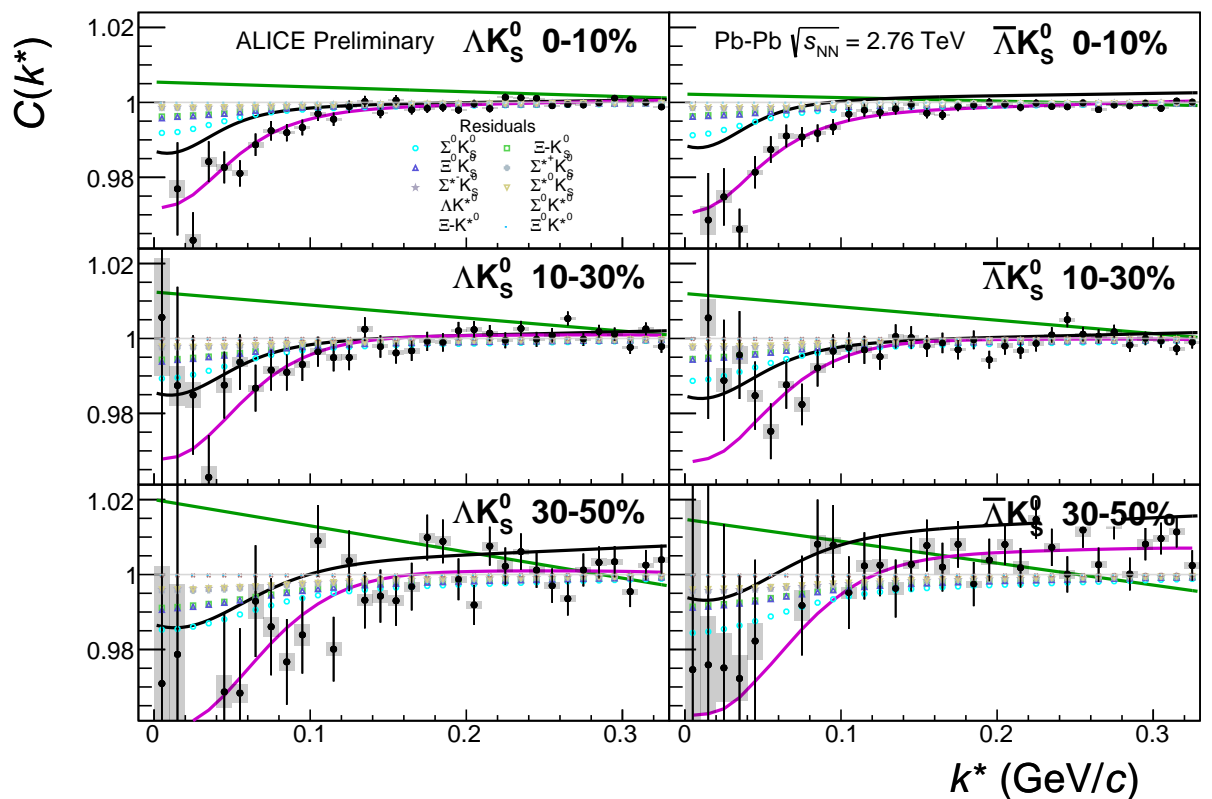


**Fig. 40:** Caption

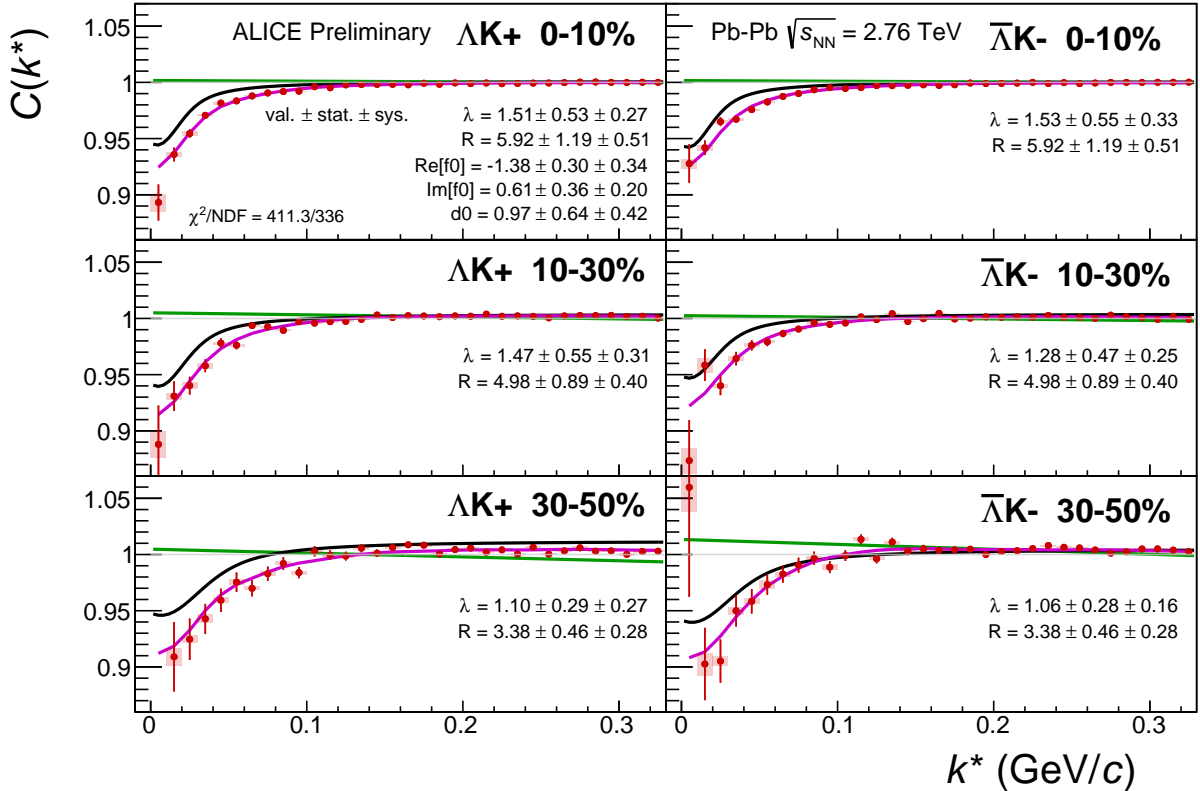


**Fig. 41:** Fits, with 10 residual correlations included, to the  $\Lambda K^+$  (left) and  $\bar{\Lambda} K^-$  (right) data for the centralities 0-10% (top), 10-30% (middle), and 30-50% (bottom). The lines represent the statistical errors, while the boxes represent the systematic errors. Each has unique  $\lambda$  and normalization parameters. The radii are shared amongst like centralities; the scattering parameters ( $\mathbb{R}f_0, \mathbb{I}f_0, d_0$ ) are shared amongst all. The black solid line represents the “raw” fit, i.e. not corrected for momentum resolution effects nor non-flat background. The green line shows the fit to the non-flat background. The purple points show the fit after momentum resolution and non-flat background corrections have been applied. The initial values of the parameters is listed, as well as the final fit values with uncertainties.

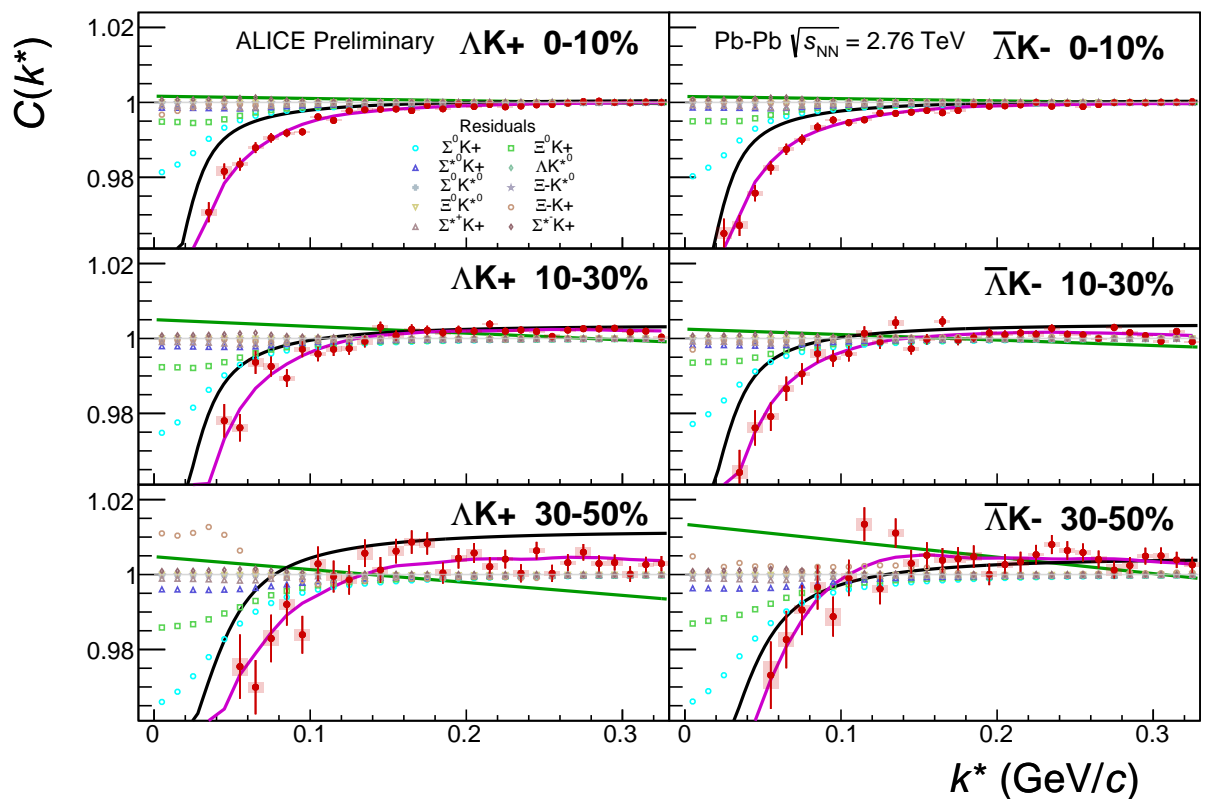


**Fig. 42:** Caption

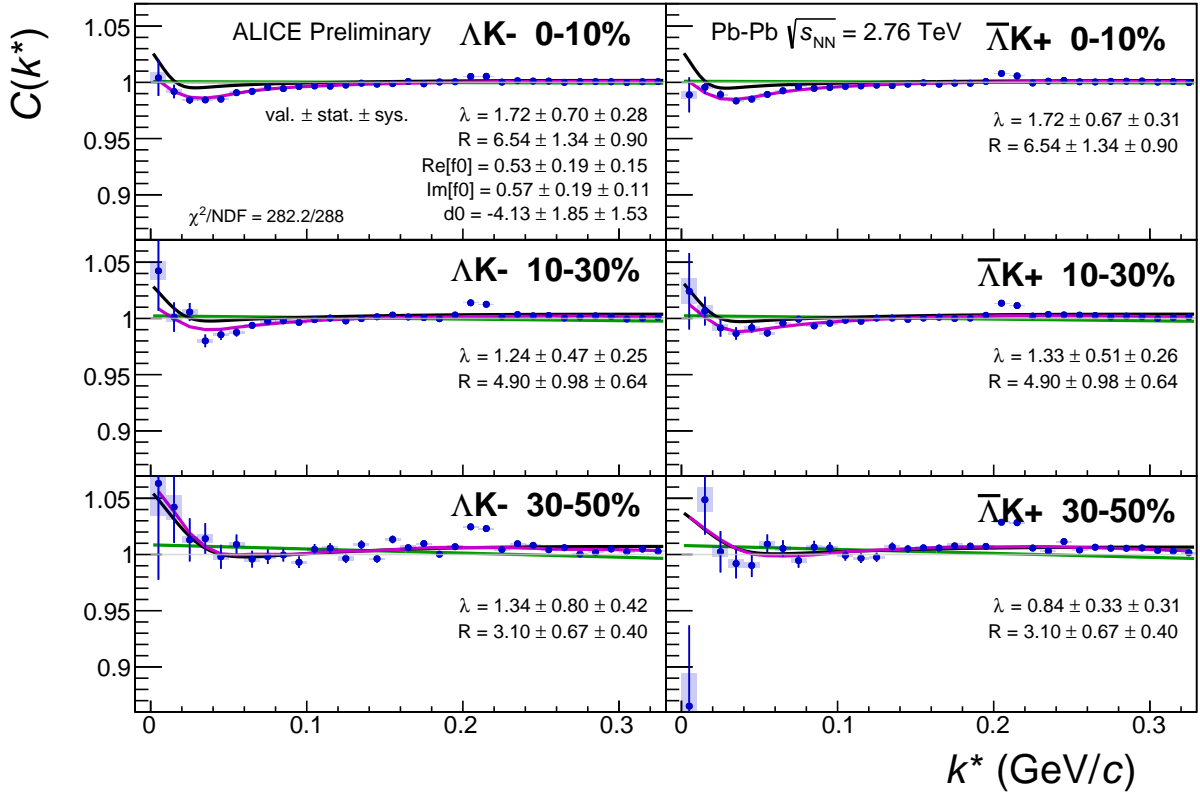


**Fig. 43:** Fits, with 10 residual correlations included, to the  $\Lambda K^-$  (left) with  $\bar{\Lambda} K^+$  (right) data for the centralities 0-10% (top), 10-30% (middle), and 30-50% (bottom). The lines represent the statistical errors, while the boxes represent the systematic errors. Each has unique  $\lambda$  and normalization parameters. The radii are shared amongst like centralities; the scattering parameters ( $\mathbb{R}f_0, \mathbb{I}f_0, d_0$ ) are shared amongst all. The black solid line represents the “raw” fit, i.e. not corrected for momentum resolution effects nor non-flat background. The green line shows the fit to the non-flat background. The purple points show the fit after momentum resolution and non-flat background corrections have been applied. The initial values of the parameters is listed, as well as the final fit values with uncertainties.

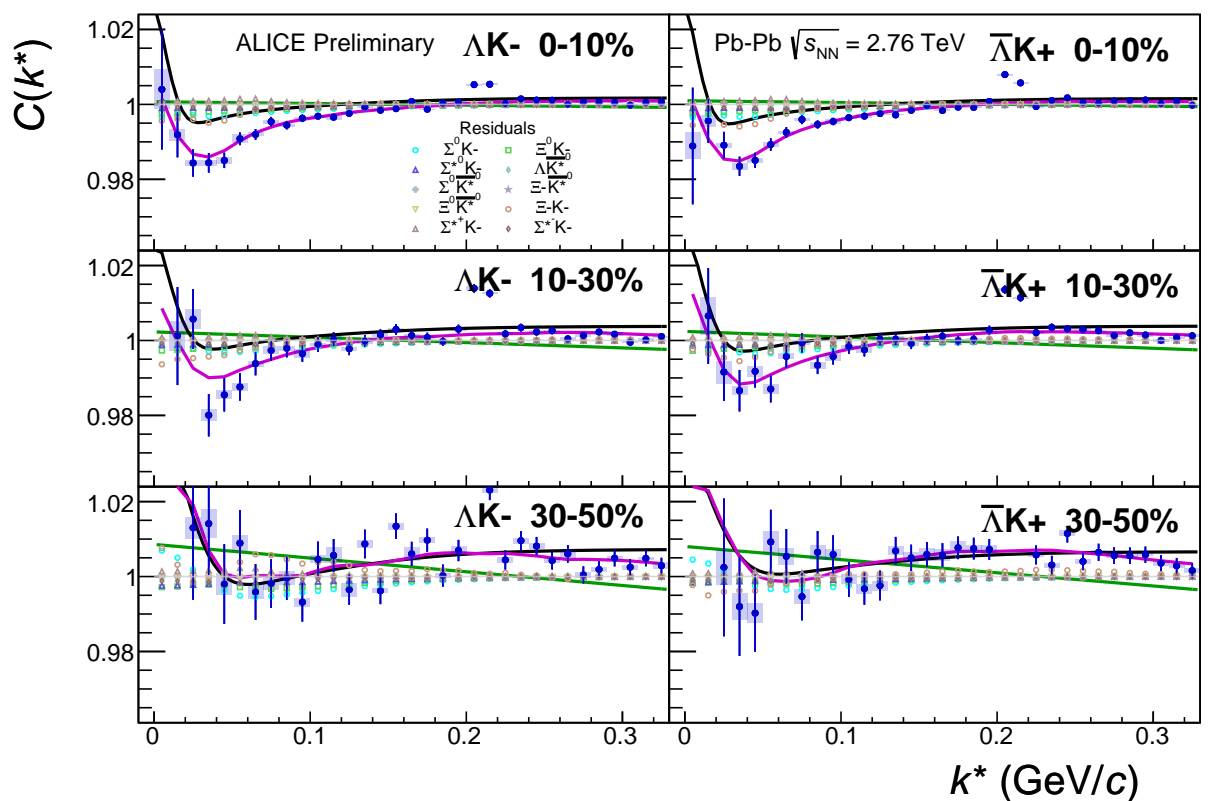


**Fig. 44:** Caption

		Fit Results $\Lambda(\bar{\Lambda})K_S^0$				
Pair Type	Centrality	Fit Parameters				
		$\lambda$	$R$	$\mathbb{R}f_0$	$\mathbb{I}f_0$	$d_0$
$\Lambda K_S^0$	0-10%	$0.60 \pm 0.63$ (stat.) $\pm 0.17$ (sys.)	$2.94 \pm 0.45$ (stat.) $\pm 0.35$ (sys.)	$-0.40 \pm 0.12$ (stat.) $\pm 0.17$ (sys.)	$0.17 \pm 0.08$ (stat.) $\pm 0.12$ (sys.)	$1.94 \pm 0.47$ (stat.) $\pm 0.77$ (sys.)
	10-30%		$2.39 \pm 0.38$ (stat.) $\pm 0.25$ (sys.)			
	30-50%		$1.81 \pm 0.29$ (stat.) $\pm 0.12$ (sys.)			
$\bar{\Lambda} K_S^0$	0-10%	$0.60 \pm 0.63$ (stat.) $\pm 0.17$ (sys.)	$2.94 \pm 0.45$ (stat.) $\pm 0.35$ (sys.)	$-0.40 \pm 0.12$ (stat.) $\pm 0.17$ (sys.)	$0.17 \pm 0.08$ (stat.) $\pm 0.12$ (sys.)	$1.94 \pm 0.47$ (stat.) $\pm 0.77$ (sys.)
	10-30%		$2.39 \pm 0.38$ (stat.) $\pm 0.25$ (sys.)			
	30-50%		$1.81 \pm 0.29$ (stat.) $\pm 0.12$ (sys.)			

**Table 13:** Fit Results  $\Lambda(\bar{\Lambda})K_S^0$ , with 10 residual correlations included. Each pair is fit simultaneously with its conjugate (ie.  $\Lambda K_S^0$  with  $\bar{\Lambda} K_S^0$ ) across all centralities (0-10%, 10-30%, 30-50%), for a total of 6 simultaneous analyses in the fit. Each analysis has a unique  $\lambda$  and normalization parameter. The radii are shared between analyses of like centrality, as these should have similar source sizes. The scattering parameters ( $\mathbb{R}f_0$ ,  $\mathbb{I}f_0$ ,  $d_0$ ) are shared amongst all. The fit is done on the data with only statistical error bars. The errors marked as “stat.” are those returned by MINUIT. The errors marked as “sys.” are those which result from my systematic analysis (as outlined in Section 6).

Fit Results $\Lambda(\bar{\Lambda})K^\pm$						
Pair Type	Centrality	Fit Parameters				
		$\lambda$	$R$	$\mathbb{R}f_0$	$\mathbb{I}f_0$	$d_0$
$\Lambda K^+$	0-10%	$1.51 \pm 0.56$ (stat.) $\pm 0.27$ (sys.)	$5.92 \pm 1.08$ (stat.) $\pm 0.51$ (sys.)	$-1.38 \pm 0.32$ (stat.) $\pm 0.34$ (sys.)	$0.61 \pm 0.34$ (stat.) $\pm 0.20$ (sys.)	$0.97 \pm 0.66$ (stat.) $\pm 0.42$ (sys.)
	10-30%	$1.47 \pm 0.55$ (stat.) $\pm 0.31$ (sys.)	$4.98 \pm 0.86$ (stat.) $\pm 0.40$ (sys.)			
	30-50%	$1.10 \pm 0.30$ (stat.) $\pm 0.27$ (sys.)	$3.38 \pm 0.45$ (stat.) $\pm 0.28$ (sys.)			
$\bar{\Lambda} K^-$	0-10%	$1.52 \pm 0.58$ (stat.) $\pm 0.33$ (sys.)	$5.92 \pm 1.08$ (stat.) $\pm 0.51$ (sys.)	$0.53 \pm 0.20$ (stat.) $\pm 0.15$ (sys.)	$0.57 \pm 0.17$ (stat.) $\pm 0.11$ (sys.)	$-4.13 \pm 1.74$ (stat.) $\pm 1.53$ (sys.)
	10-30%	$1.28 \pm 0.47$ (stat.) $\pm 0.25$ (sys.)	$4.98 \pm 0.86$ (stat.) $\pm 0.40$ (sys.)			
	30-50%	$1.06 \pm 0.28$ (stat.) $\pm 0.16$ (sys.)	$3.38 \pm 0.45$ (stat.) $\pm 0.28$ (sys.)			
$\Lambda K^-$	0-10%	$1.72 \pm 0.61$ (stat.) $\pm 0.28$ (sys.)	$6.54 \pm 1.22$ (stat.) $\pm 0.90$ (sys.)	$0.53 \pm 0.20$ (stat.) $\pm 0.15$ (sys.)	$0.57 \pm 0.17$ (stat.) $\pm 0.11$ (sys.)	$-4.13 \pm 1.74$ (stat.) $\pm 1.53$ (sys.)
	10-30%	$1.24 \pm 0.43$ (stat.) $\pm 0.25$ (sys.)	$4.90 \pm 0.94$ (stat.) $\pm 0.64$ (sys.)			
	30-50%	$1.34 \pm 0.75$ (stat.) $\pm 0.42$ (sys.)	$3.10 \pm 0.67$ (stat.) $\pm 0.40$ (sys.)			
$\bar{\Lambda} K^+$	0-10%	$1.72 \pm 0.58$ (stat.) $\pm 0.31$ (sys.)	$6.54 \pm 1.22$ (stat.) $\pm 0.90$ (sys.)	$0.53 \pm 0.20$ (stat.) $\pm 0.15$ (sys.)	$0.57 \pm 0.17$ (stat.) $\pm 0.11$ (sys.)	$-4.13 \pm 1.74$ (stat.) $\pm 1.53$ (sys.)
	10-30%	$1.33 \pm 0.46$ (stat.) $\pm 0.26$ (sys.)	$4.90 \pm 0.94$ (stat.) $\pm 0.64$ (sys.)			
	30-50%	$0.84 \pm 0.31$ (stat.) $\pm 0.31$ (sys.)	$3.10 \pm 0.67$ (stat.) $\pm 0.40$ (sys.)			

**Table 14:** Fit Results  $\Lambda(\bar{\Lambda})K^\pm$ , with 10 residual correlations included.. Each pair is fit simultaneously with its conjugate (ie.  $\Lambda K^+$  with  $\bar{\Lambda} K^-$  and  $\Lambda K^-$  with  $\bar{\Lambda} K^+$ ) across all centralities (0-10%, 10-30%, 30-50%), for a total of 6 simultaneous analyses in the fit. Each analysis has a unique  $\lambda$  and normalization parameter. The radii are shared between analyses of like centrality, as these should have similar source sizes. The scattering parameters ( $\mathbb{R}f_0$ ,  $\mathbb{I}f_0$ ,  $d_0$ ) are shared amongst all. The fit is done on the data with only statistical error bars. The errors marked as “stat.” are those returned by MINUIT. The errors marked as “sys.” are those which result from my systematic analysis (as outlined in Section 6).

**Fit Parameters (value  $\pm$  statistical error  $\pm$  systematic error)**

<b>Pair Type</b>	<b>Centrality</b>	<b>R</b>		
$\Lambda K^+ \& \bar{\Lambda} K^-$	<b>0-10%</b>		<b><math>5.92 \pm 1.08 \pm 0.51</math></b>	
	<b>10-30%</b>		<b><math>4.98 \pm 0.86 \pm 0.40</math></b>	
	<b>30-50%</b>		<b><math>3.38 \pm 0.45 \pm 0.28</math></b>	
		<b><math>\Re f_0</math></b>	<b><math>\Im f_0</math></b>	<b><math>d_0</math></b>
		<b><math>-1.38 \pm 0.32 \pm 0.34</math></b>	<b><math>0.61 \pm 0.34 \pm 0.20</math></b>	<b><math>0.97 \pm 0.66 \pm 0.42</math></b>
$\Lambda K^- \& \bar{\Lambda} K^+$	<b>0-10%</b>		<b><math>6.54 \pm 1.22 \pm 0.90</math></b>	
	<b>10-30%</b>		<b><math>4.90 \pm 0.94 \pm 0.64</math></b>	
	<b>30-50%</b>		<b><math>3.10 \pm 0.67 \pm 0.40</math></b>	
		<b><math>\Re f_0</math></b>	<b><math>\Im f_0</math></b>	<b><math>d_0</math></b>
		<b><math>0.53 \pm 0.20 \pm 0.15</math></b>	<b><math>0.57 \pm 0.17 \pm 0.11</math></b>	<b><math>-4.13 \pm 1.74 \pm 1.53</math></b>
$\Lambda K_S^0 \& \bar{\Lambda} K_S^0$	<b>0-10%</b>		<b><math>2.94 \pm 0.45 \pm 0.35</math></b>	
	<b>10-30%</b>		<b><math>2.39 \pm 0.38 \pm 0.25</math></b>	
	<b>30-50%</b>		<b><math>1.81 \pm 0.29 \pm 0.12</math></b>	
		<b><math>\Re f_0</math></b>	<b><math>\Im f_0</math></b>	<b><math>d_0</math></b>
		<b><math>-0.40 \pm 0.12 \pm 0.17</math></b>	<b><math>0.17 \pm 0.08 \pm 0.12</math></b>	<b><math>1.94 \pm 0.47 \pm 0.77</math></b>

**Table 15:** Fit Results  $\Lambda(\bar{\Lambda})K^\pm$  and  $\Lambda(\bar{\Lambda})K_S^0$ , with 10 residual correlations included. ( $\lambda$  parameters not shown). This table is a condensed version of Tables 13 and 14

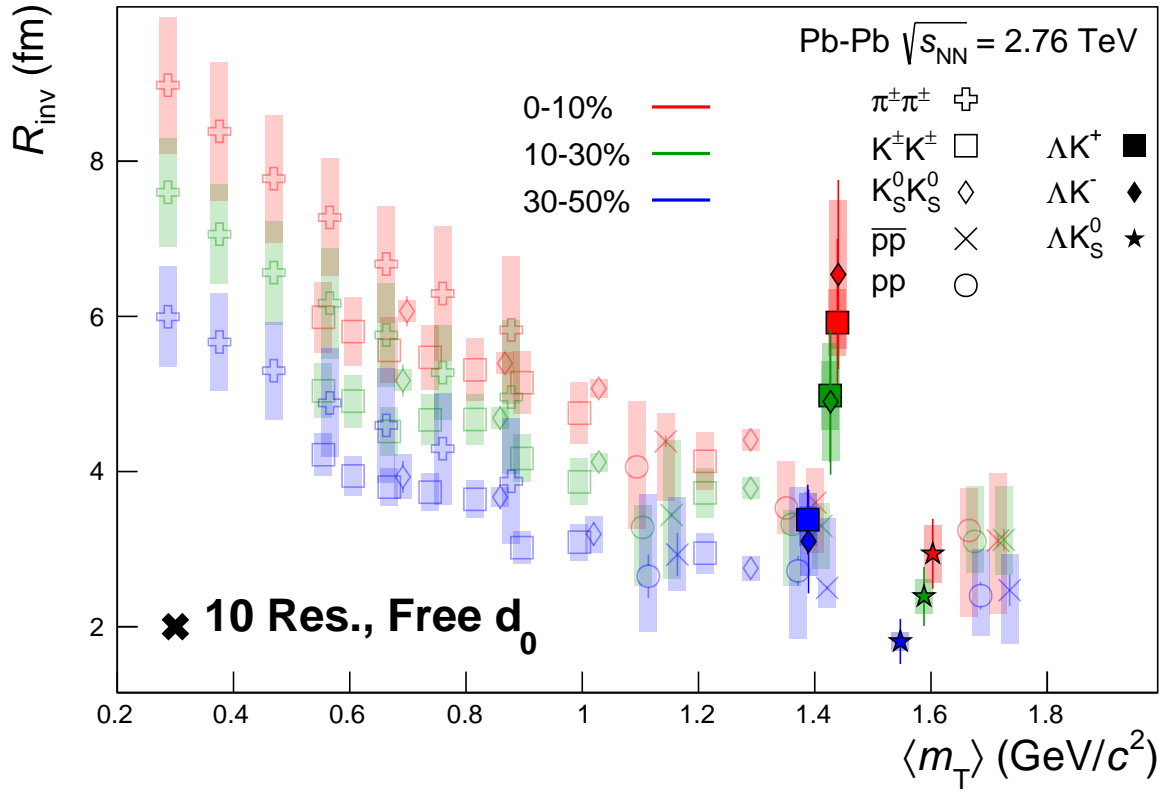


**Fig. 45:** 10 residual correlations in  $\Lambda K$  fits. Extracted fit  $R_{\text{inv}}$  parameters as a function of pair transverse mass ( $m_T$ ) for various pair systems over several centralities. The ALICE published data [11] is shown with transparent, open symbols. The new  $\Lambda K$  results are shown with opaque, filled symbols. In the left, the  $\Lambda K^+$  (with its conjugate pair) results are shown separately from the  $\Lambda K^-$  (with its conjugate pair) results. In the right, all  $\Lambda K^\pm$  results are averaged.

## 671 7.2 Results: $\Xi K^\pm$

672 Even without any fits to the data, the fact that the  $\Xi^- K^+$  data dips below unity (Fig. 46) is exciting, as  
 673 this cannot occur purely from a Coulomb interaction. We hope that this dip signifies that we are able to  
 674 peer through the overwhelming contribution from the Coulomb interaction to see the effects arising from  
 675 the strong interaction.

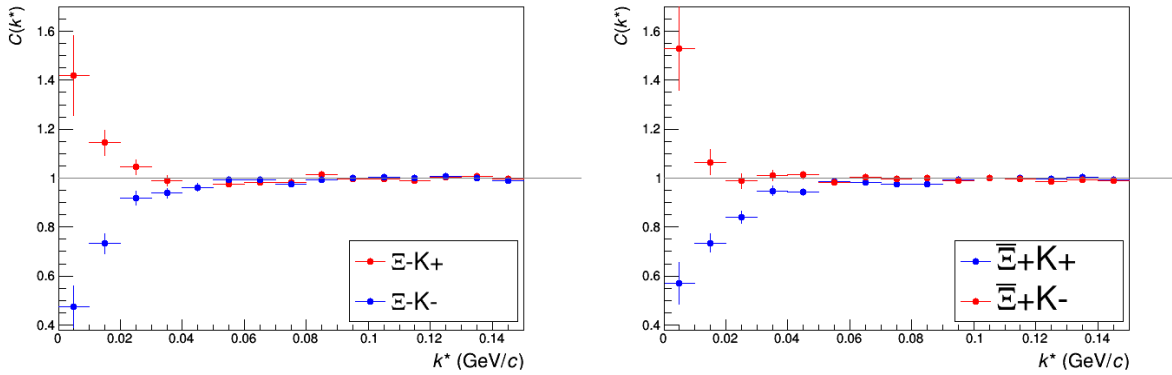
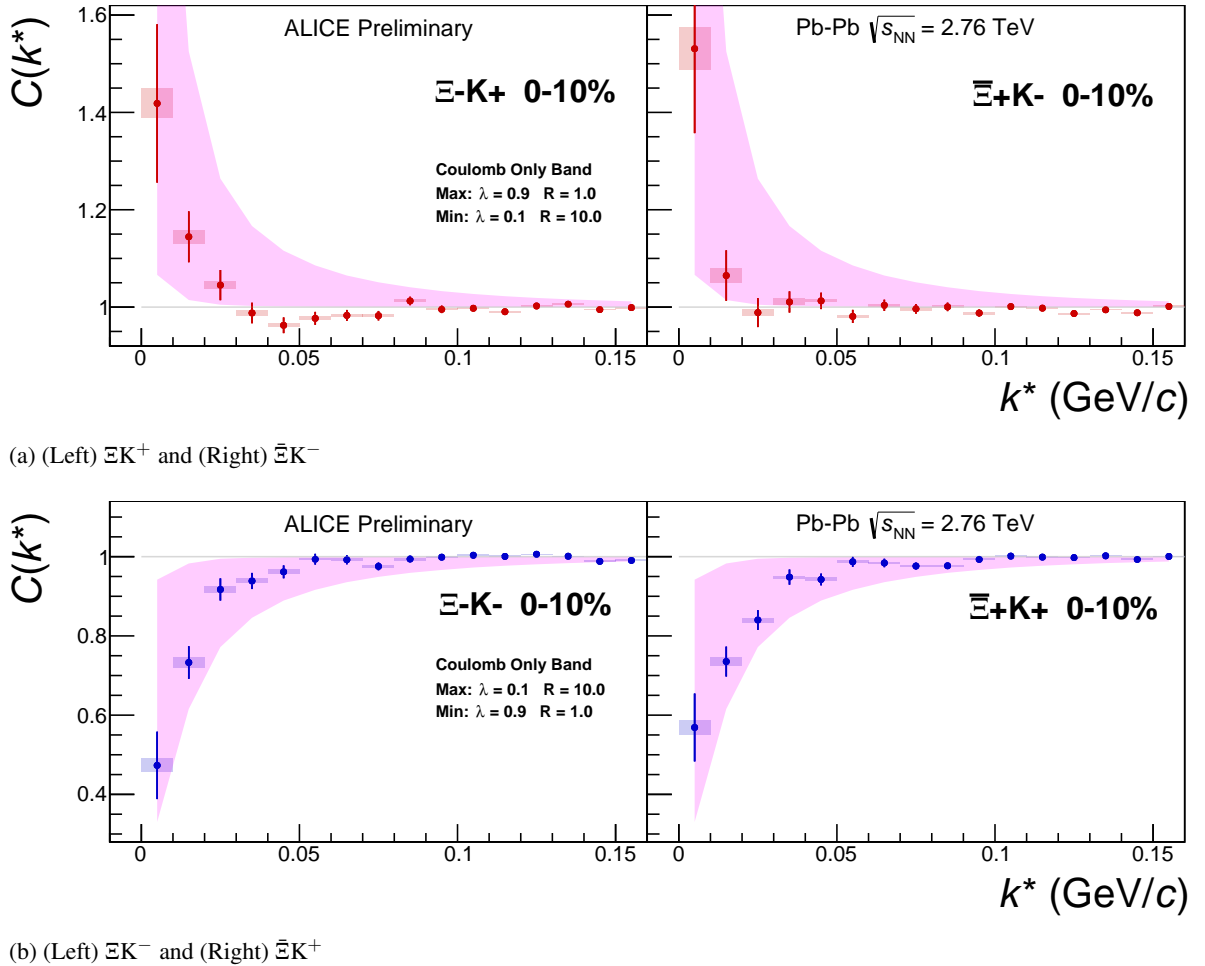


**Fig. 46:**  $\Xi K^\pm$  Results for 0-10% Centrality. (Left)  $\Xi^- K^+$  and  $\Xi^- K^-$  (Right)  $\Xi^+ K^+$  and  $\Xi^+ K^-$

676 Figure 47 demonstrates graphically, that the  $\Xi^- K^+$  results cannot be described by solely the Coulomb  
 677 interaction. In this figure, we present the data along with a Coulomb-only band. The Coulomb-only  
 678 band is spanned by two Coulomb-only curves, whose parameters are given in the figure. The Coulomb-  
 679 only curves were generated using a technique identical to the generation of the fit function, described  
 680 in Sec. 5.2, except, of course, with the nuclear scattering parameters all set to zero. The Coulomb-only  
 681 curves change monotonically with varying  $\lambda$  or varyin radius parametre, therefore, any curves built with  
 682 parameter sets intermediate to those use in the Coulomb-only band will be contained in the band.

683 Including the strong interaction into the simulation can dramatically change the resulting correlation  
 684 function, as shown in Figure 48. In the figure, the solid line represents a Coulomb-only curve, i.e. a  
 685 simulated correlation function with the strong interaction turned off. The dashed lines represent a full  
 686 simulation, including both the strong and Coulomb interactions. The two dashed lines differ only in the  
 687 real part of the assumed scattering length: positive in Set 1, and negative in Set 2. In the top figure,  
 688 for the  $\Xi^- K^+$  simulation, we see that parameter set 2, with a negative real part of the scattering length,  
 689 causes the simulated curve to dip below unity, as is seen in the data. If there is a parallel to be drawn  
 690 between this analysis and the  $\Lambda K$  analysis, we expect to see similar effects in the  $\Lambda K^+$  system and the  
 691  $\Xi^- K^+$  systems. In these systems, we could have an  $s\bar{s}$  annihilation picture. Or, another possible way of  
 692 thinking about these systems is in terms of net strangeness. The  $\Lambda K^+$  system has  $S=0$ , while the  $\Lambda K^-$   
 693 has  $S=-2$ . The  $\Xi^- K^+$  has  $S=-1$ , while the  $\Xi^- K^-$  has  $S=-3$ .

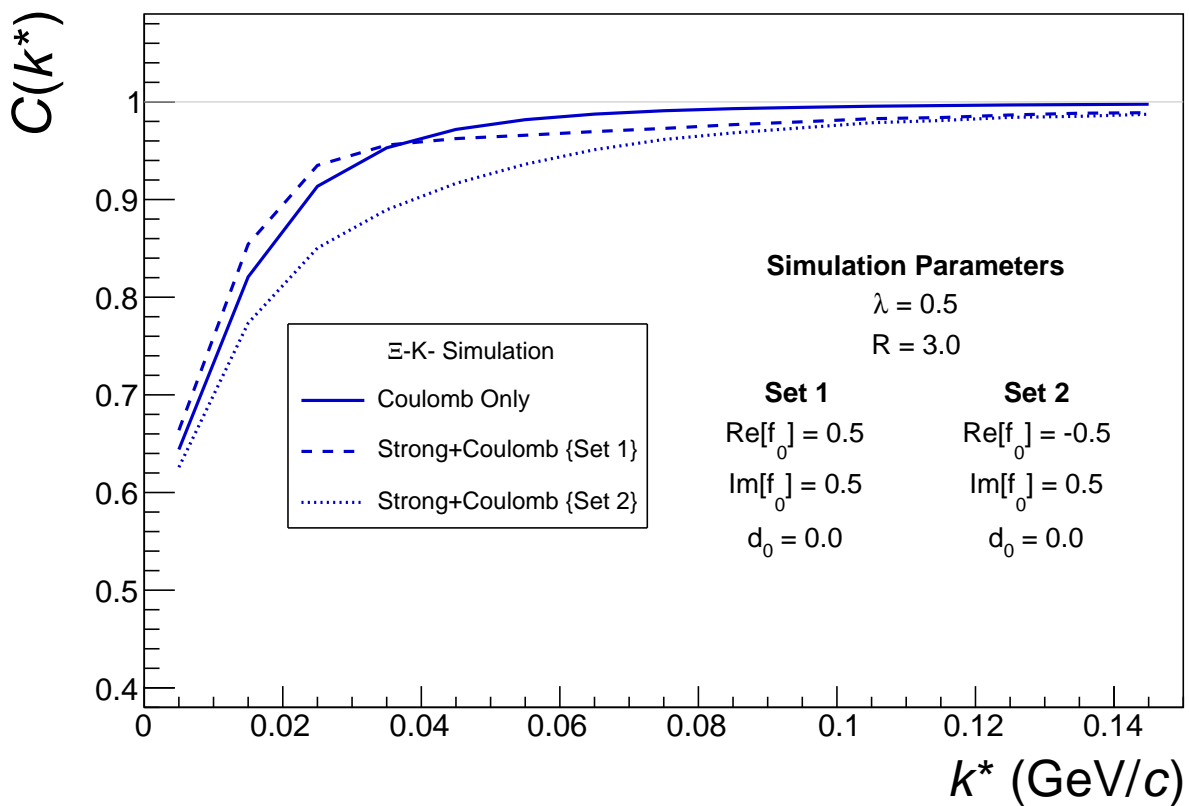
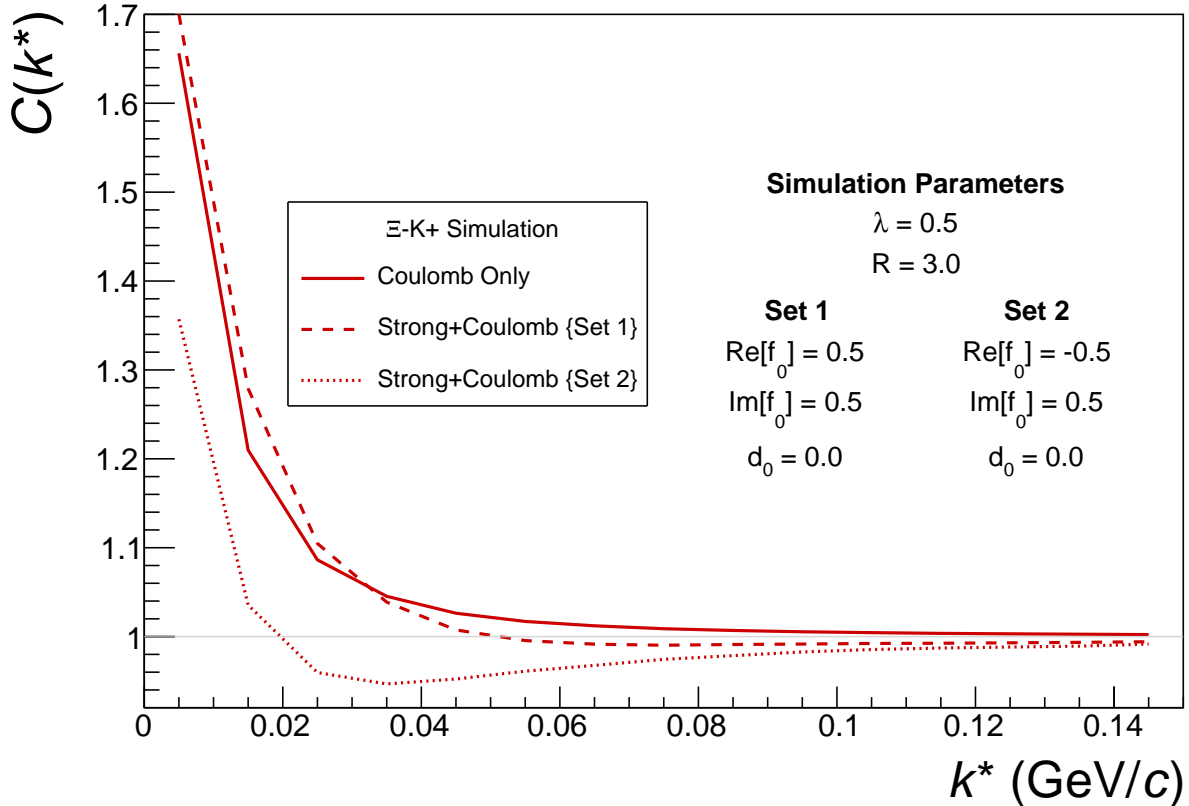
694 The author was asked to perform a global Coulomb-only fit to the data, to ensure that the system truly  
 695 could not be described simply by the Coulomb interaction. In order words, in the fit, the strong force was  
 696 turned off, and the  $\Xi^- K^+$ ,  $\Xi^+ K^-$ ,  $\Xi^- K^-$ ,  $\Xi^+ K^+$  systems all share one sinlge radius parameter, while the  
 697 pair and conjugate pair systems share a  $\lambda$  parameter. The results of this fit are shown in Figures 49 and  
 698 50. In Fig. 49, there was a lower limit of 0.1 fm placed on the radius parameter, and the radius parameter  
 699 was initialized to 3 fm (as seems reasonable, when considering the transverse mass of the system and  
 700 looking at Fig. 45). As is shown in the results, the radius parameter reached this unrealistic lower bound  
 701 of 0.1 fm. In Fig. 50, the parameters were all unbounded, and the radius parameter was initialized to 10  
 702 fm. In this case, the radius parameters reamins high, and ends at an unrealistic value of 10.84 fm. In both  
 703 cases, the  $\lambda$  parameters are too low. From these figures, we conclude that a global Coulomb-only fit is  
 704 not suitable for the data.



**Fig. 47:**  $\Xi K^\pm$  data with Coulomb-only bands for the 0-10% centrality bin. The Coulomb-only bands span two sets of Coulomb-only curves: (1)  $\lambda = 0.9$ ,  $R = 1.0$  fm and (2)  $\lambda = 0.1$ ,  $R = 10.0$  fm. The Coulomb-only curves are simulated correlation functions for the respective pair system assuming only a Coulomb interaction, i.e. ignoring the strong interaction. The Coulomb-only curves change monotonically with varying  $\lambda$  and varying  $R$ , therefore, any intermediate parameter set will fall within this Coulomb-only band.

Although the global Coulomb-only fit failed, it is possible that a Coulomb-only fit performed on  $\Xi^- K^+$  and  $\bar{\Xi}^+ K^-$  separately from  $\Xi^- K^-$  and  $\bar{\Xi}^+ K^+$  could be suitable. The result of such fits are shown in Figures 51 and 52. Figure 51, shows that the fit is not able to describe the dip in the  $\Xi^- K^+$  data below unity. Of course, this is obviously true for an attractive Coulomb-only fit. The radius parameter of 8.43 fm extracted from this fit is unrealistically large. In Figure 52 shows the Coulomb-only fit can described the  $\Xi^- K^-$  data reasonable well; although the extracted radius of 3.73 fm is somewhat larger than expected.

## 8 To Do

(b)  $\Xi K^-$  and  $\bar{\Xi} K^+$  simulation

**Fig. 48:** Effect on the Coulomb-only curve of including the strong interaction for  $\Xi K^\pm$  systems. The solid line represents a Coulomb-only curve, i.e. a simulated correlation function with the strong interaction turned off. The dashed lines represent a full simulation, including both the strong and Coulomb interactions. The two dashed lines differ only in the real part of the assumed scattering length: positive in Set 1, and negative in Set 2.

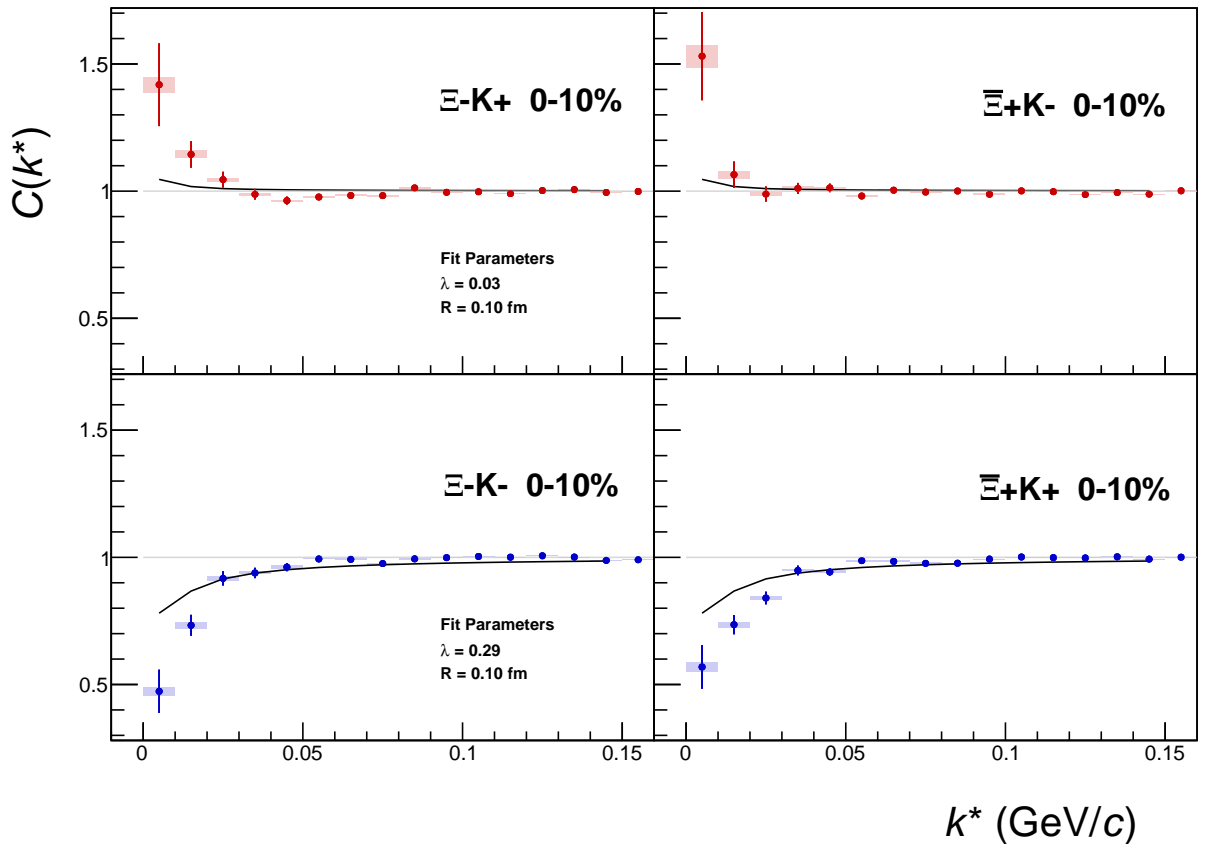


**Fig. 49:**  $\Xi K^\pm$  Global Coulomb-only fit (Set 1) for 0-10% centrality. In this fit, there was a lower limit of 0.1 fm placed on the radius parameter, and the radius parameter was initialized to 3 fm (as seems reasonable, when considering the transverse mass of the system and looking at Fig. 45). As is shown in the results, the radius parameter reached this unrealistic lower bound of 0.1 fm. Also, the extracted  $\lambda$  parameters are too low.

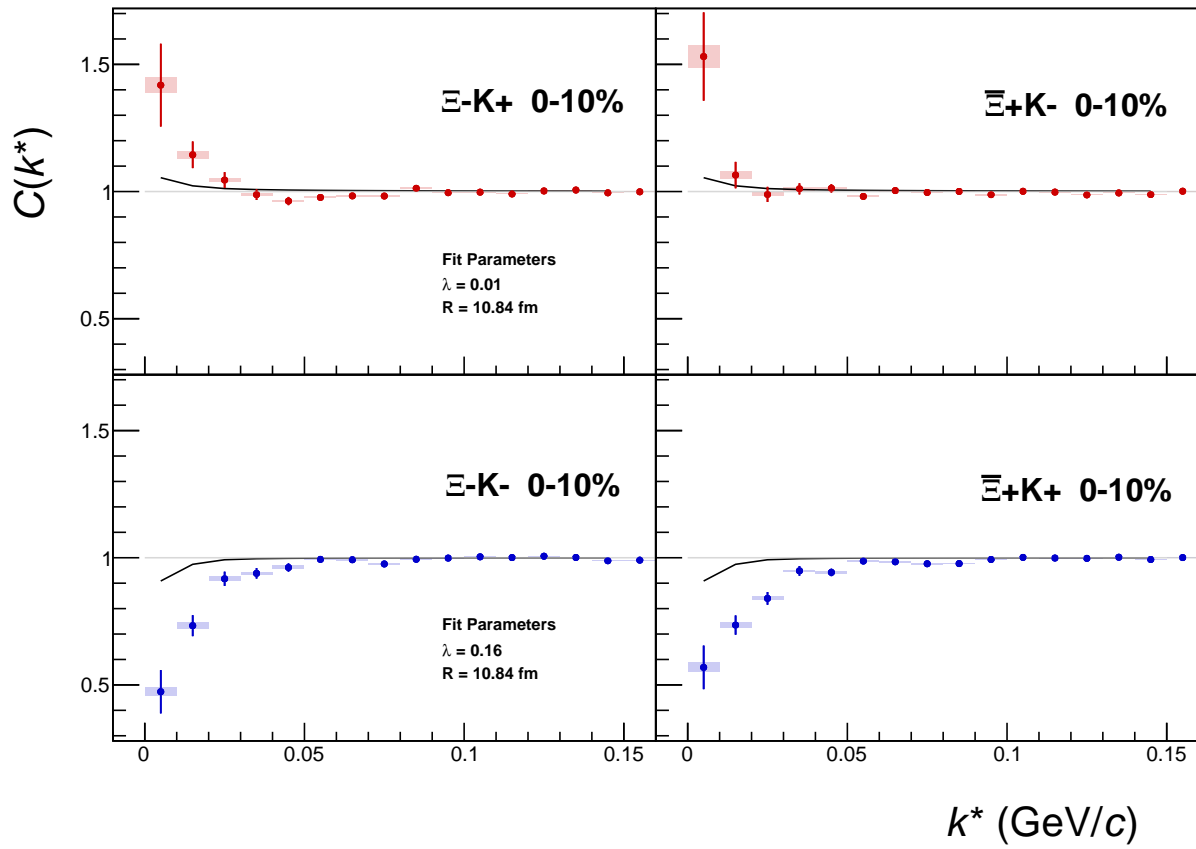


**Fig. 50:**  $\Xi K^{\pm}$  Global Coulomb-only fit (Set 2) for 0-10% centrality. In this fit, the parameters were all unbounded, and the radius parameter was initialized to 10 fm. In this case, the radius parameter remains high, and ends at an unrealistic value of 10.84 fm. Also, the extracted  $\lambda$  parameters are too low.

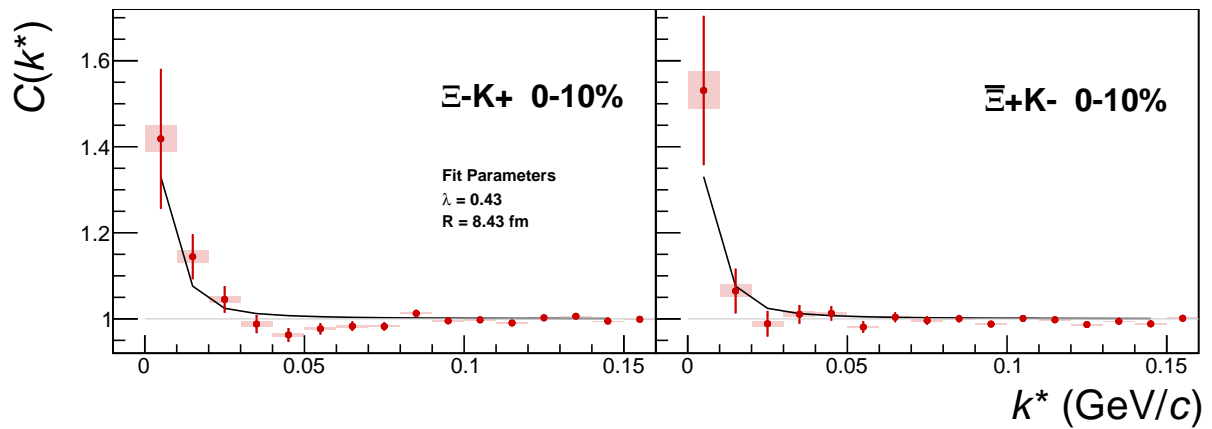


**Fig. 51:**  $\Xi^- K^+$  Coulomb-only fit for 0-10% centrality

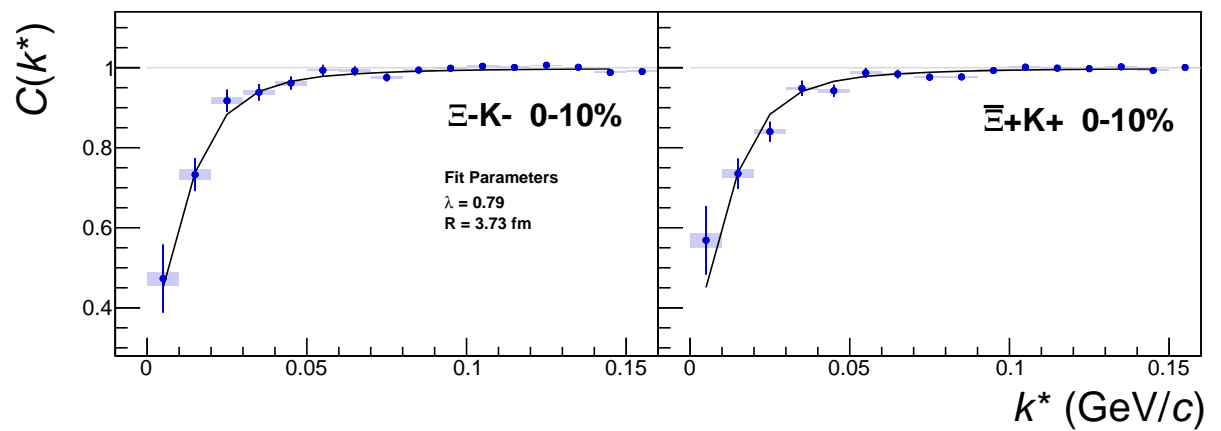
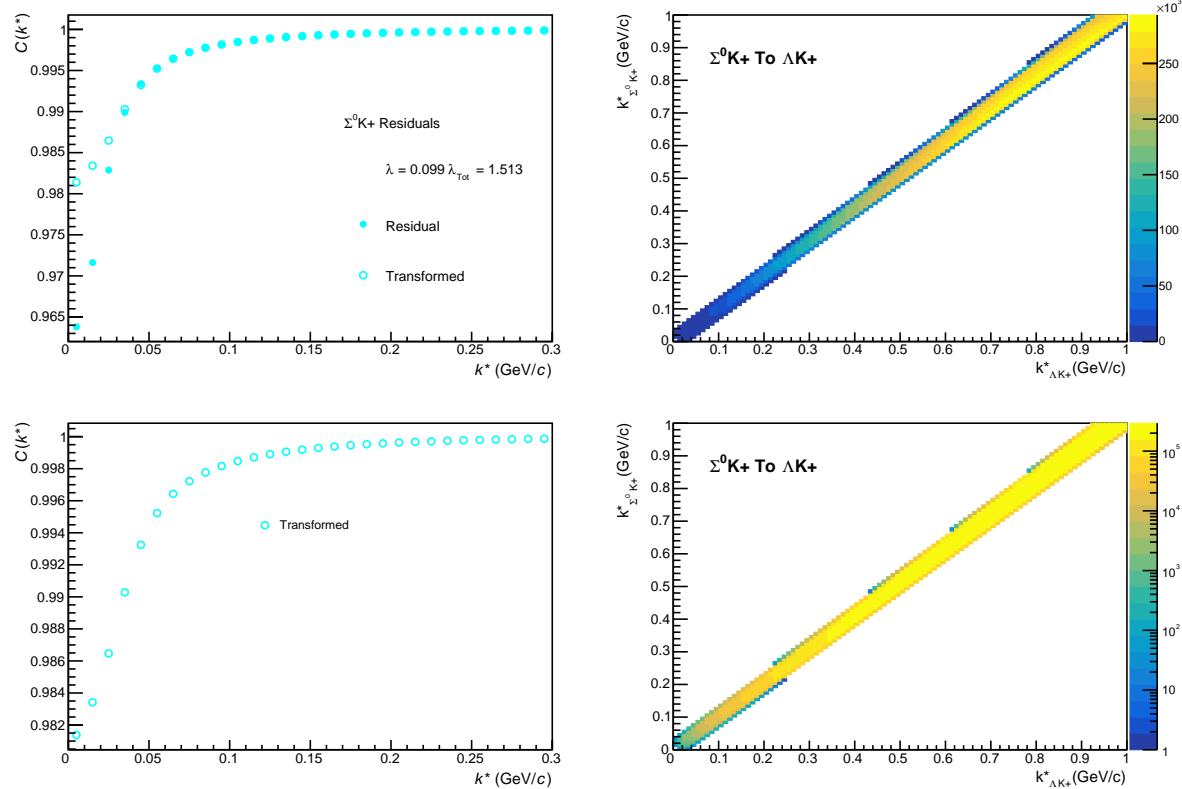


**Fig. 52:**  $\Xi^- K^-$  Coulomb-only fit for 0-10% centrality

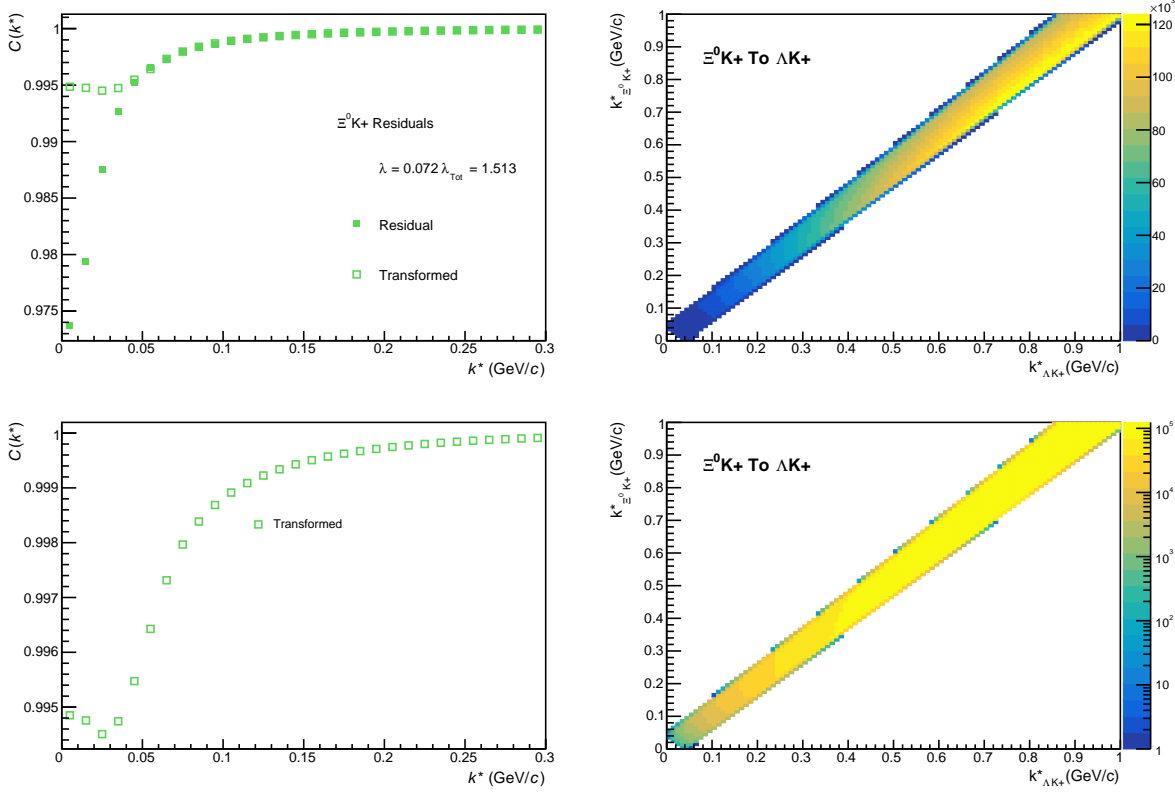
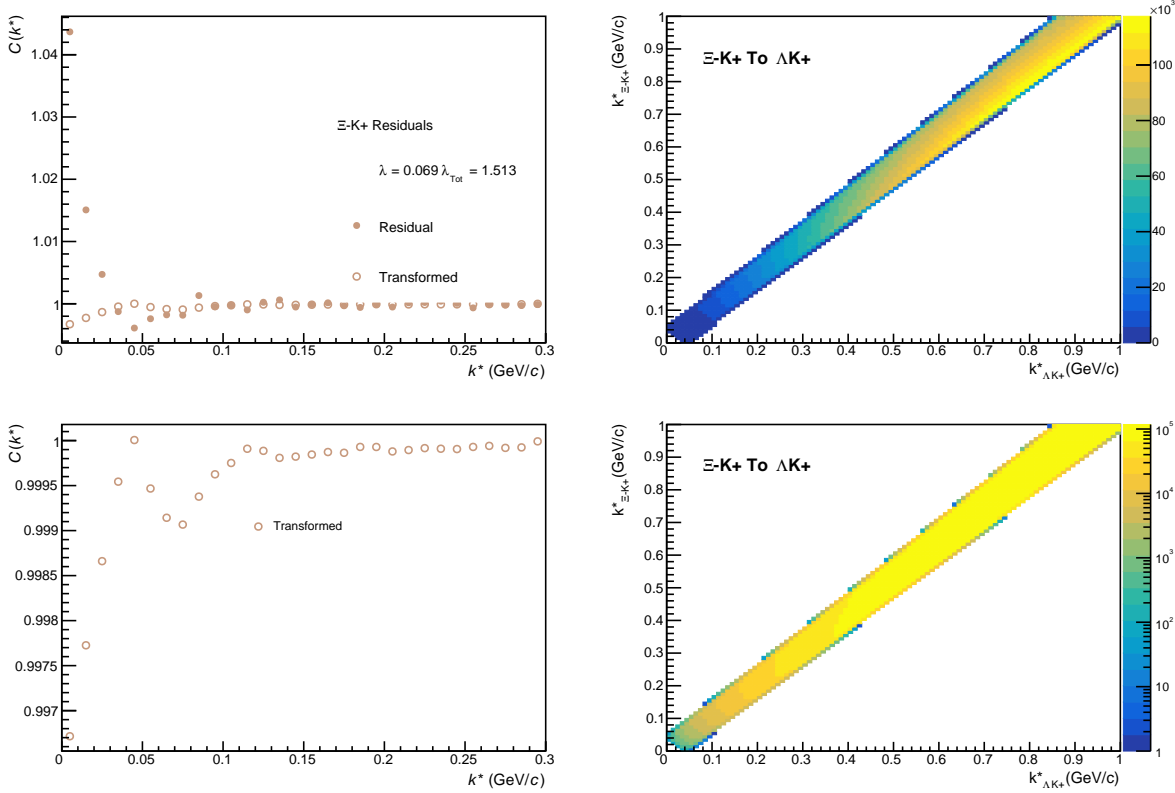
713 **9 Additional Figures**

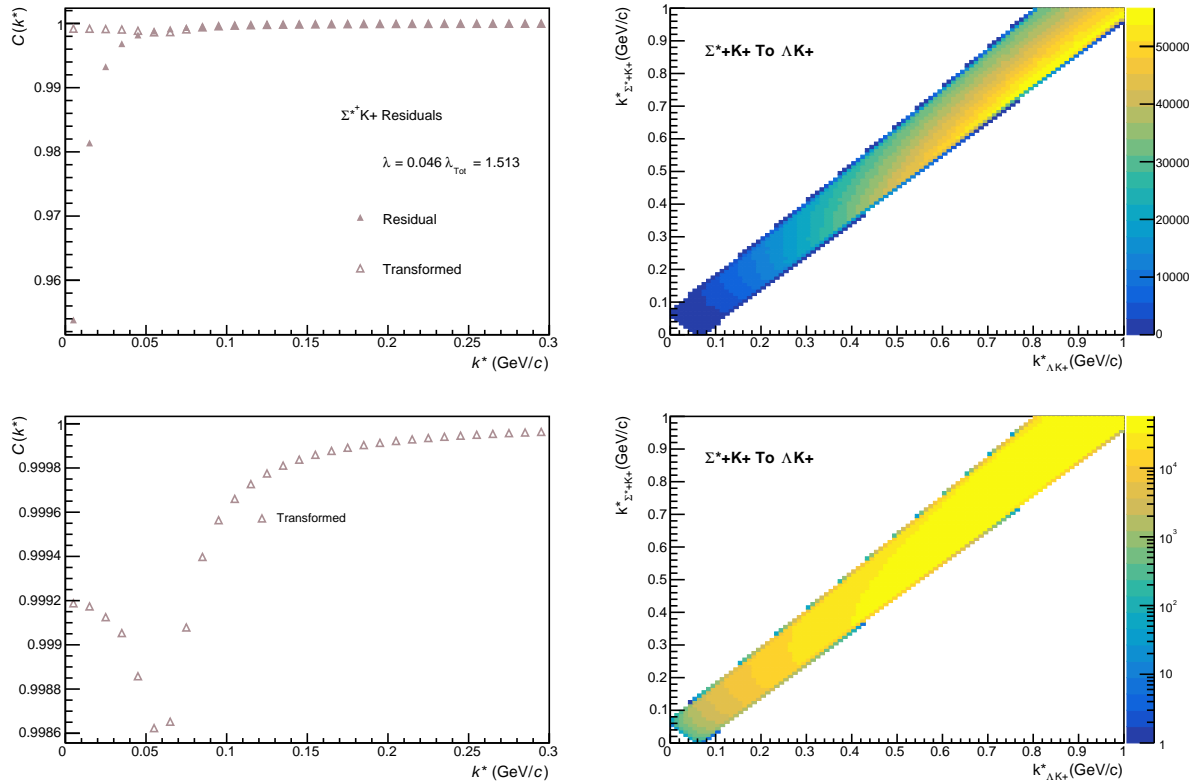
714 **9.1 Residuals**

715 **9.1.1  $\Lambda K^+$  Residuals**

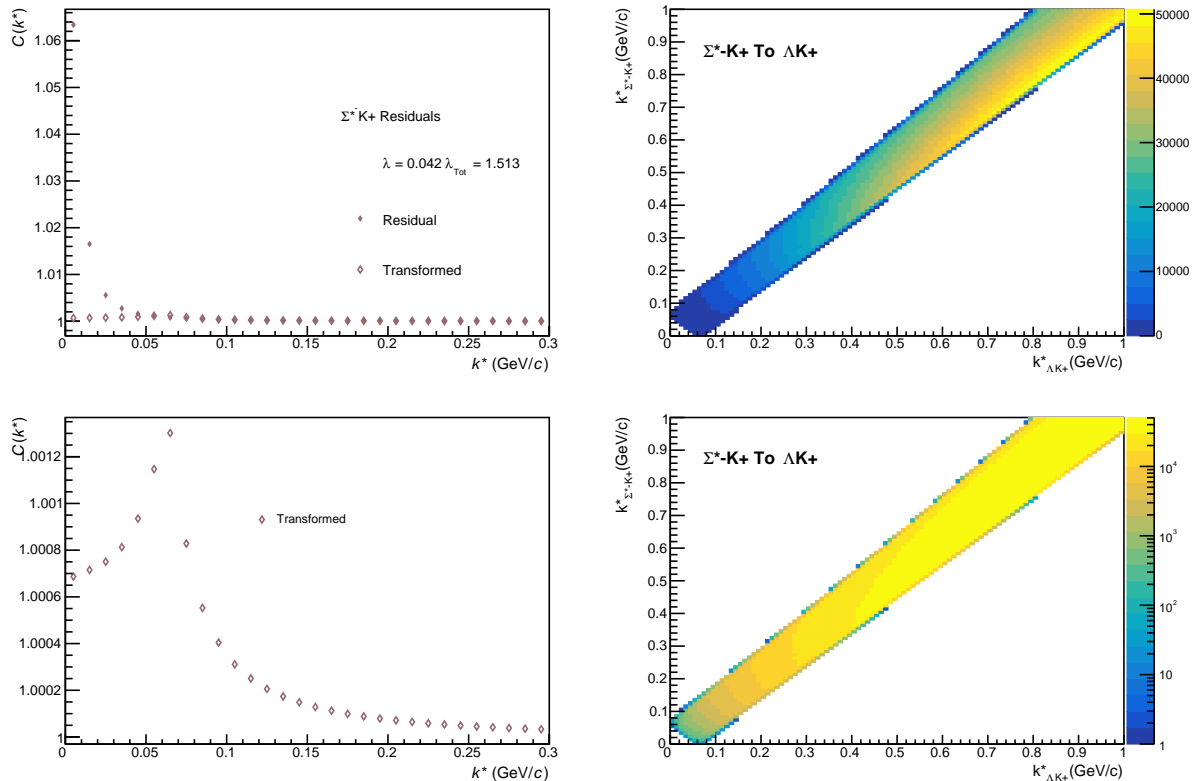


**Fig. 53:** Residuals:  $\Sigma^0 K^+$  to  $\Lambda K^+$  (0-10% Centrality)

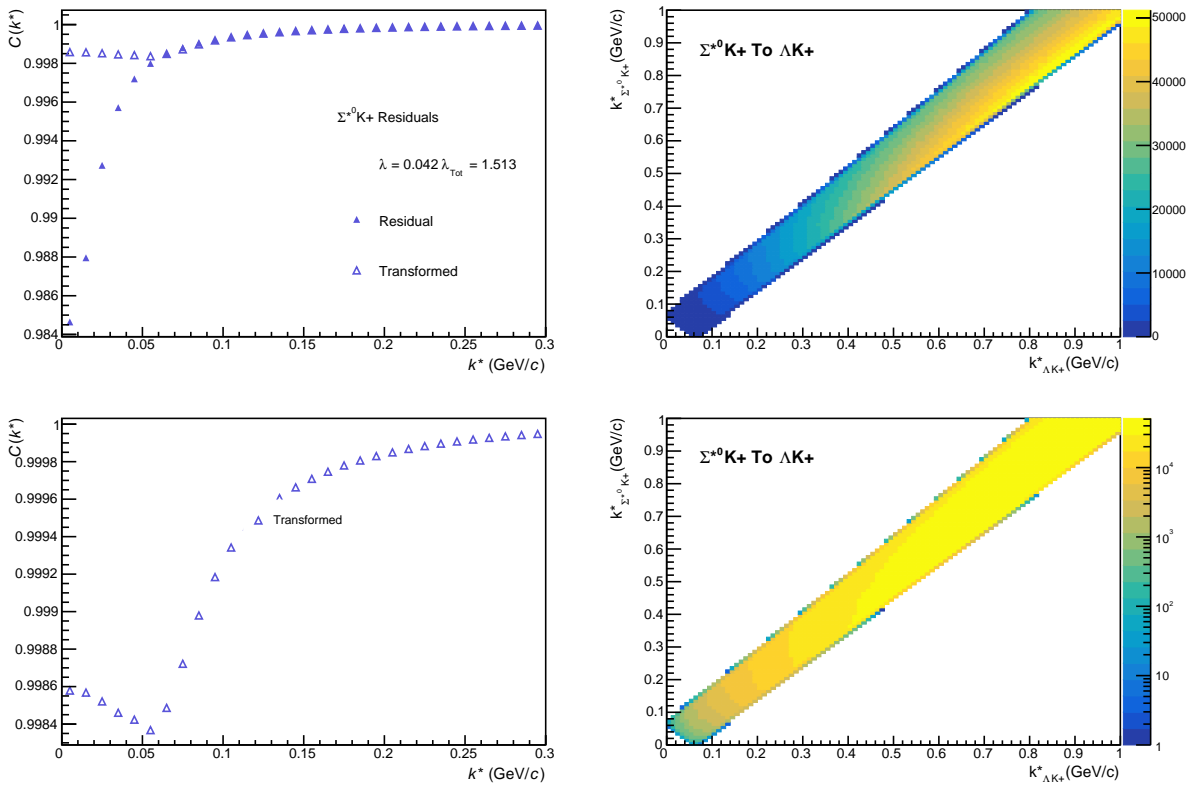
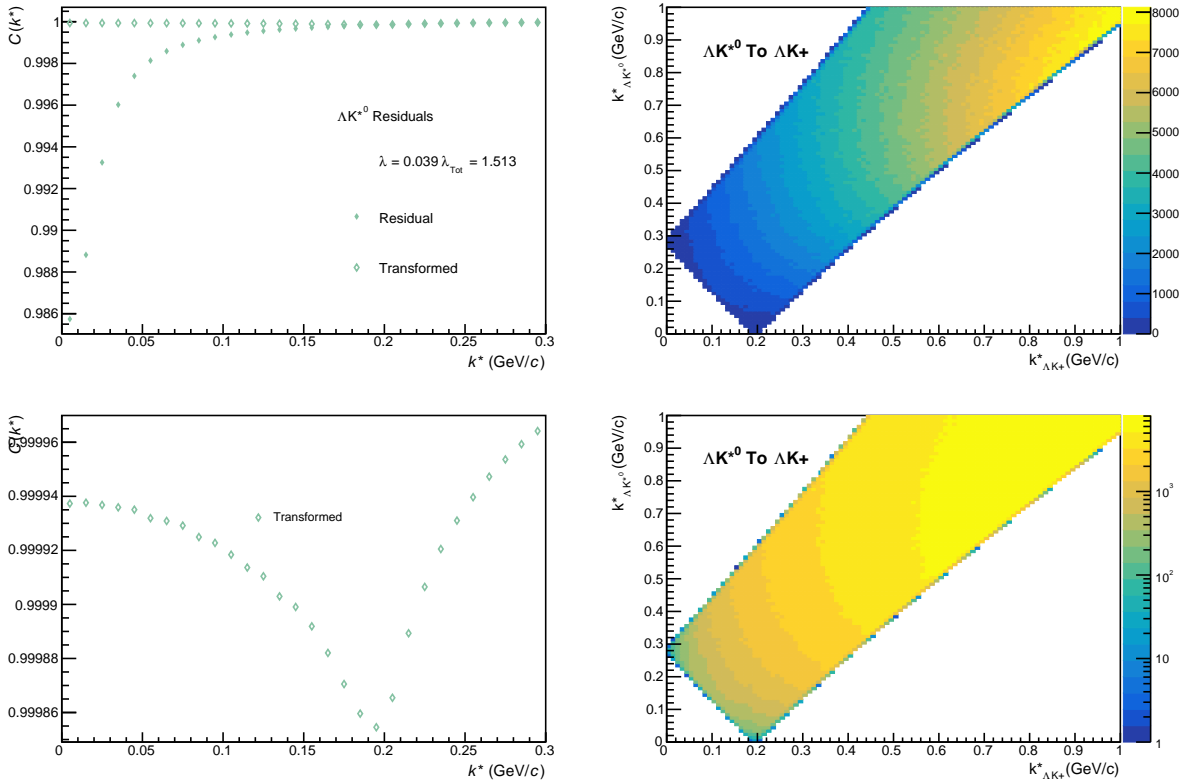

**Fig. 54:** Residuals:  $\Xi^0 \text{K}^+$  to  $\Lambda \text{K}^+$  (0-10% Centrality)

**Fig. 55:** Residuals:  $\Xi^- \text{K}^+$  to  $\Lambda \text{K}^+$  (0-10% Centrality)

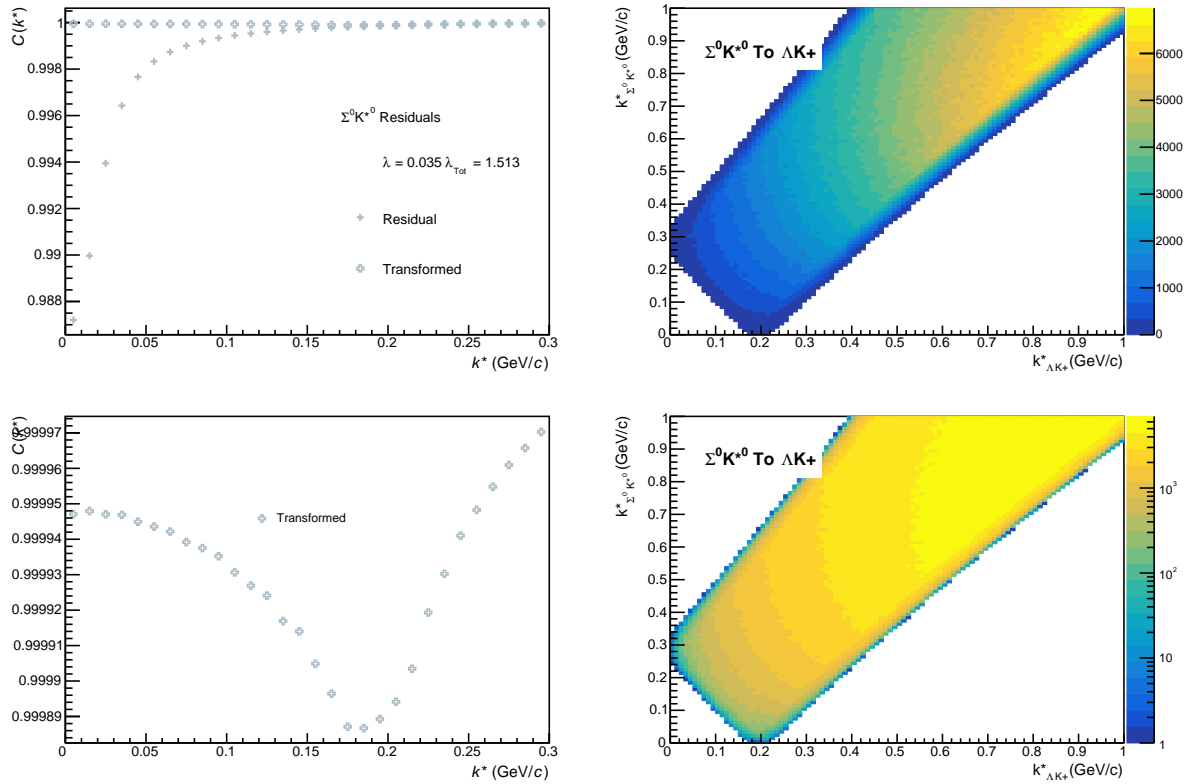


**Fig. 56:** Residuals:  $\Sigma^+ K^+$  to  $\Lambda K^+$  (0-10% Centrality)

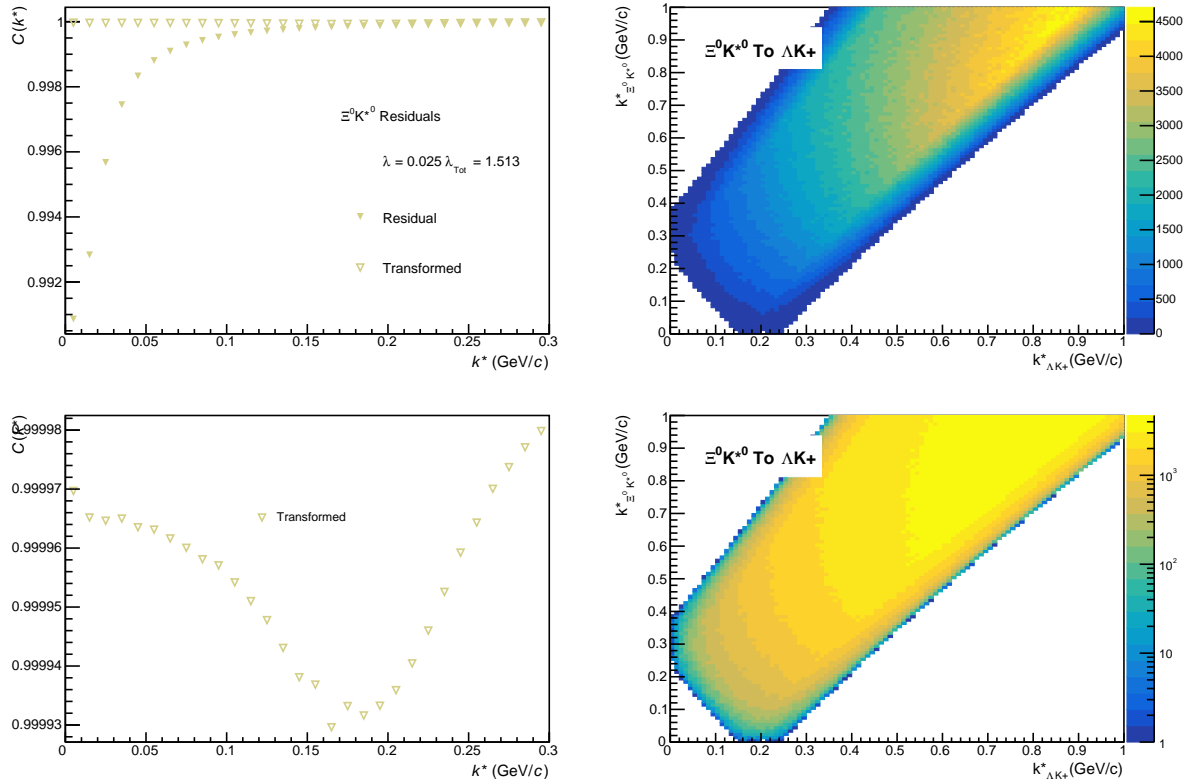


**Fig. 57:** Residuals:  $\Sigma^- K^+$  to  $\Lambda K^+$  (0-10% Centrality)

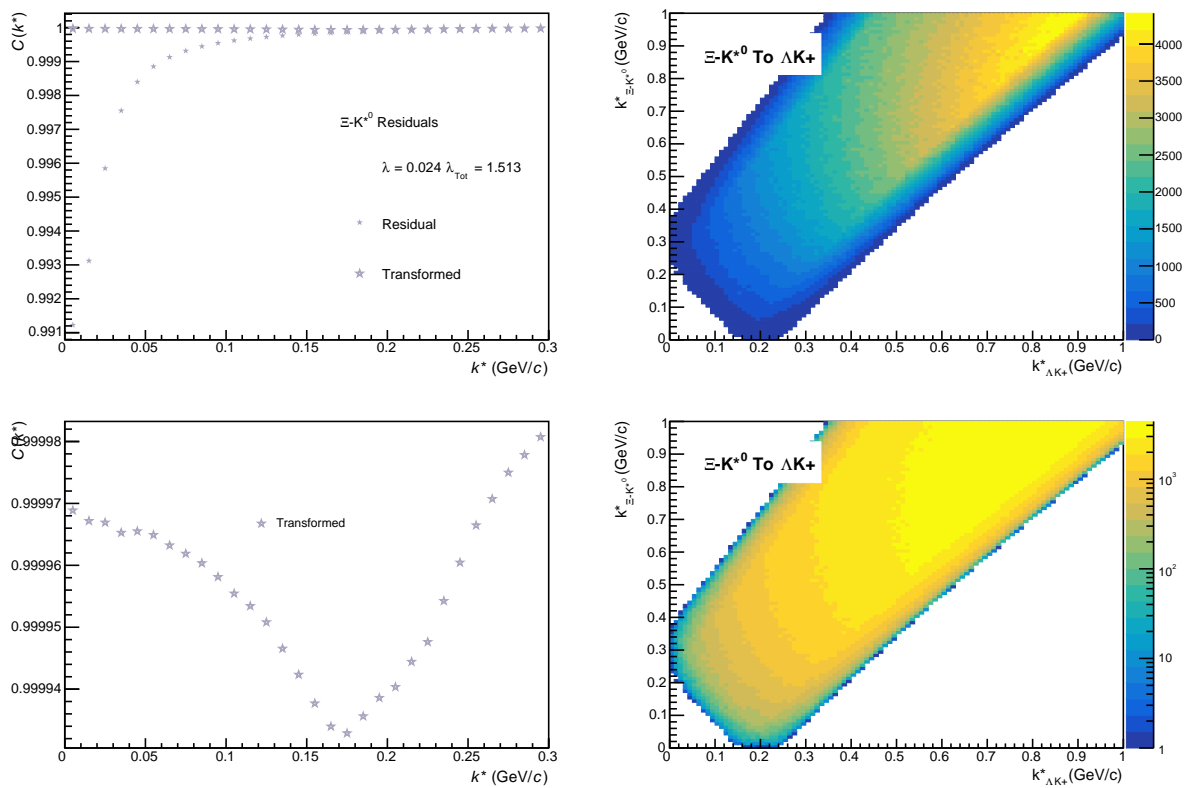

**Fig. 58:** Residuals:  $\Sigma^{*0} \text{K}^+$  to  $\Lambda \text{K}^+$  (0-10% Centrality)

**Fig. 59:** Residuals:  $\Lambda \text{K}^{*0}$  to  $\Lambda \text{K}^+$  (0-10% Centrality)



**Fig. 60:** Residuals:  $\Sigma^0 K^{*0}$  to  $\Lambda K^+$  (0-10% Centrality)

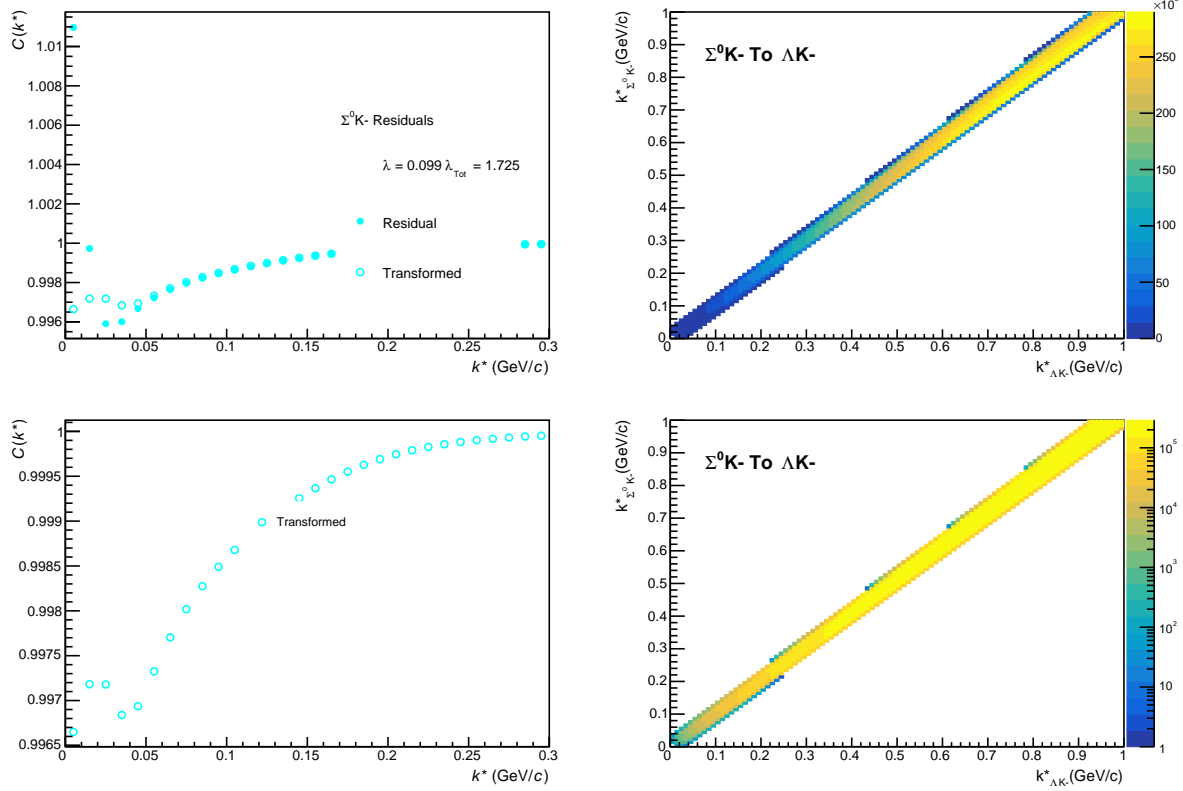


**Fig. 61:** Residuals:  $\Xi^0 K^{*0}$  to  $\Lambda K^+$  (0-10% Centrality)

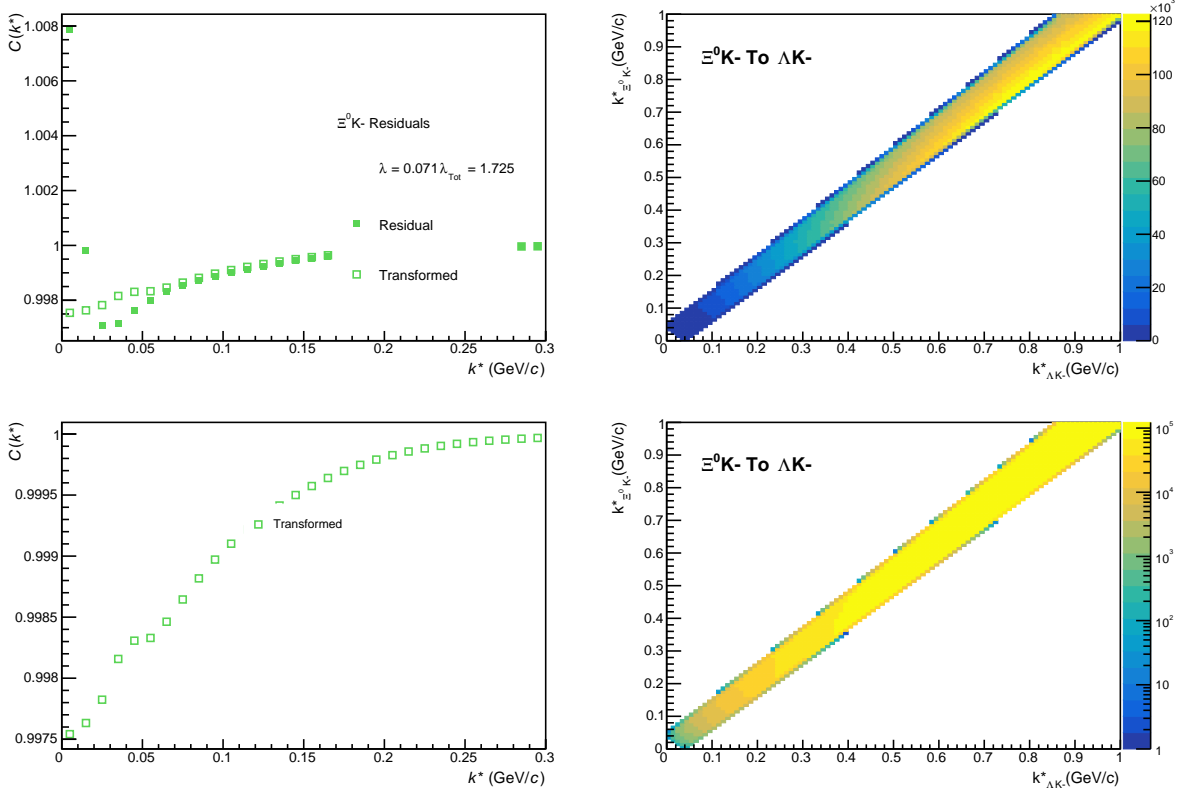
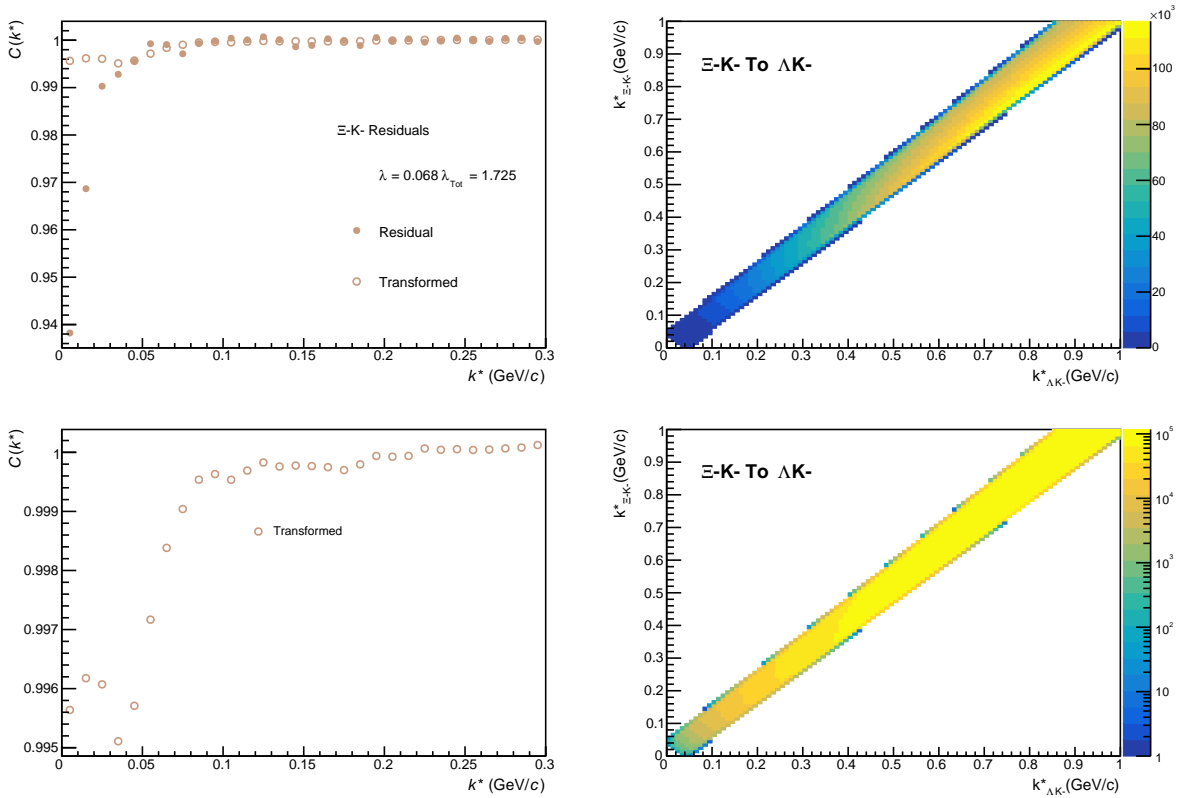


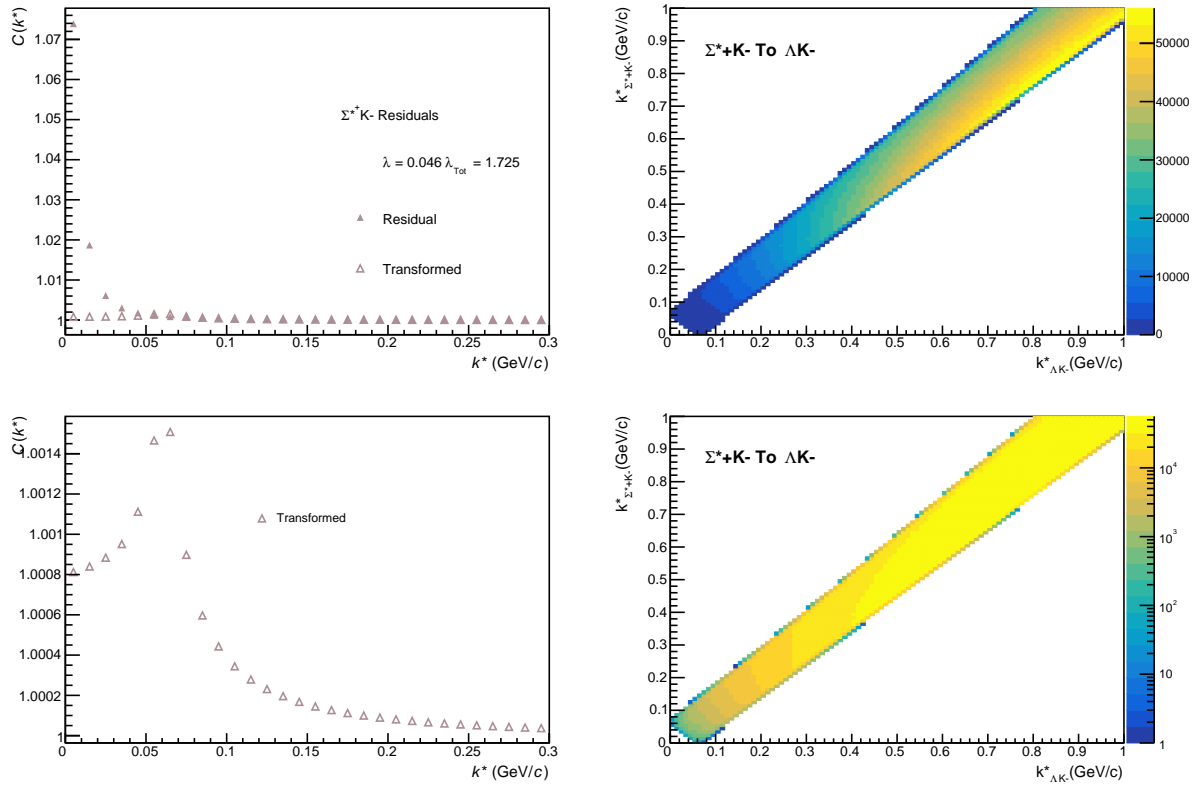
**Fig. 62:** Residuals:  $\Xi\text{-}K^{*0}$  to  $\Lambda K^+$  (0-10% Centrality)

716 **9.1.2  $\Lambda K^-$  Residuals**

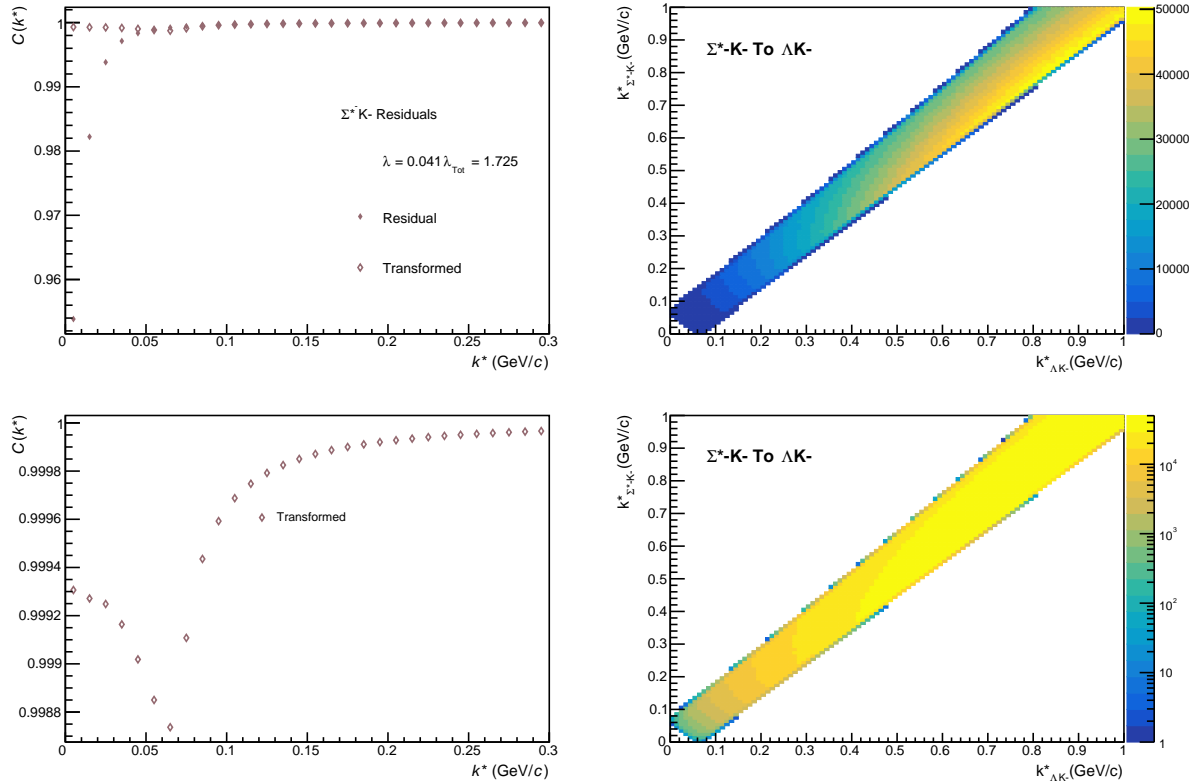


**Fig. 63:** Residuals:  $\Sigma^0 K^-$  to  $\Lambda K^-$  (0-10% Centrality)

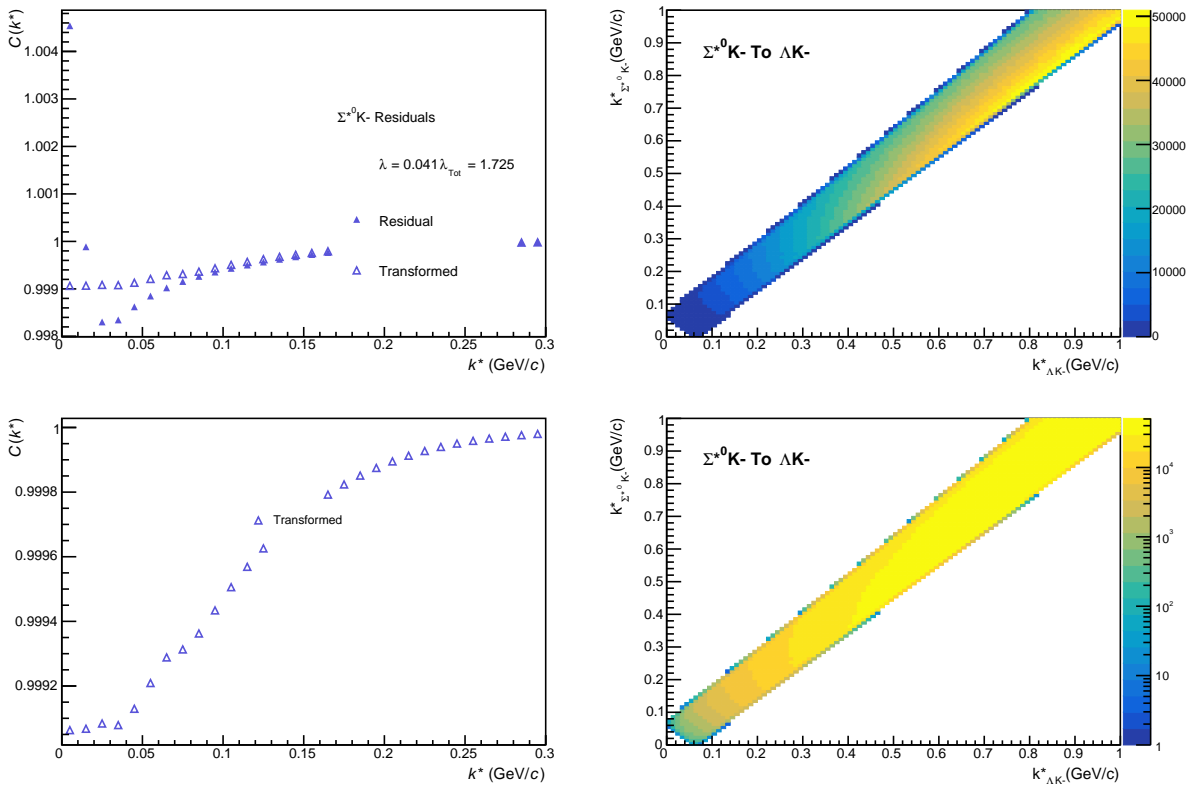
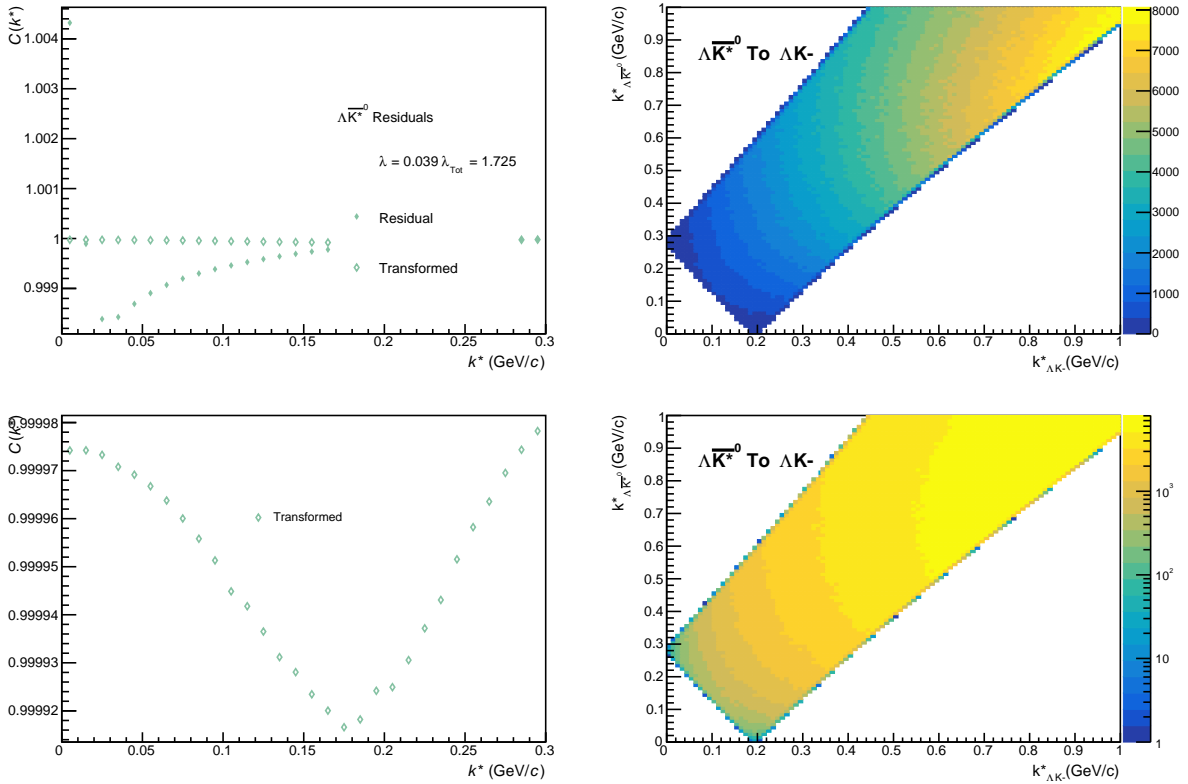

**Fig. 64:** Residuals:  $\Xi^0 \text{K}^-$  to  $\Lambda \text{K}^-$  (0-10% Centrality)

**Fig. 65:** Residuals:  $\Xi^- \text{K}^-$  to  $\Lambda \text{K}^-$  (0-10% Centrality)

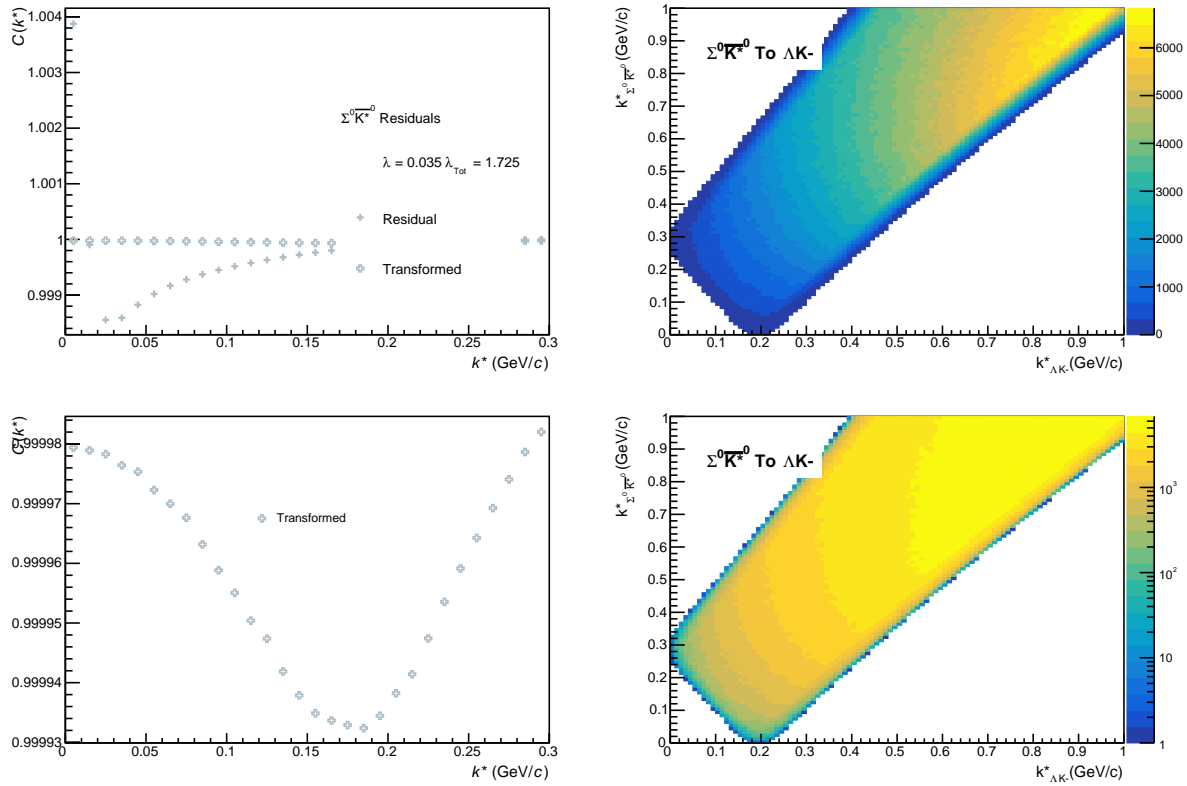


**Fig. 66:** Residuals:  $\Sigma^* + K^- \rightarrow \Lambda K^-$  (0-10% Centrality)

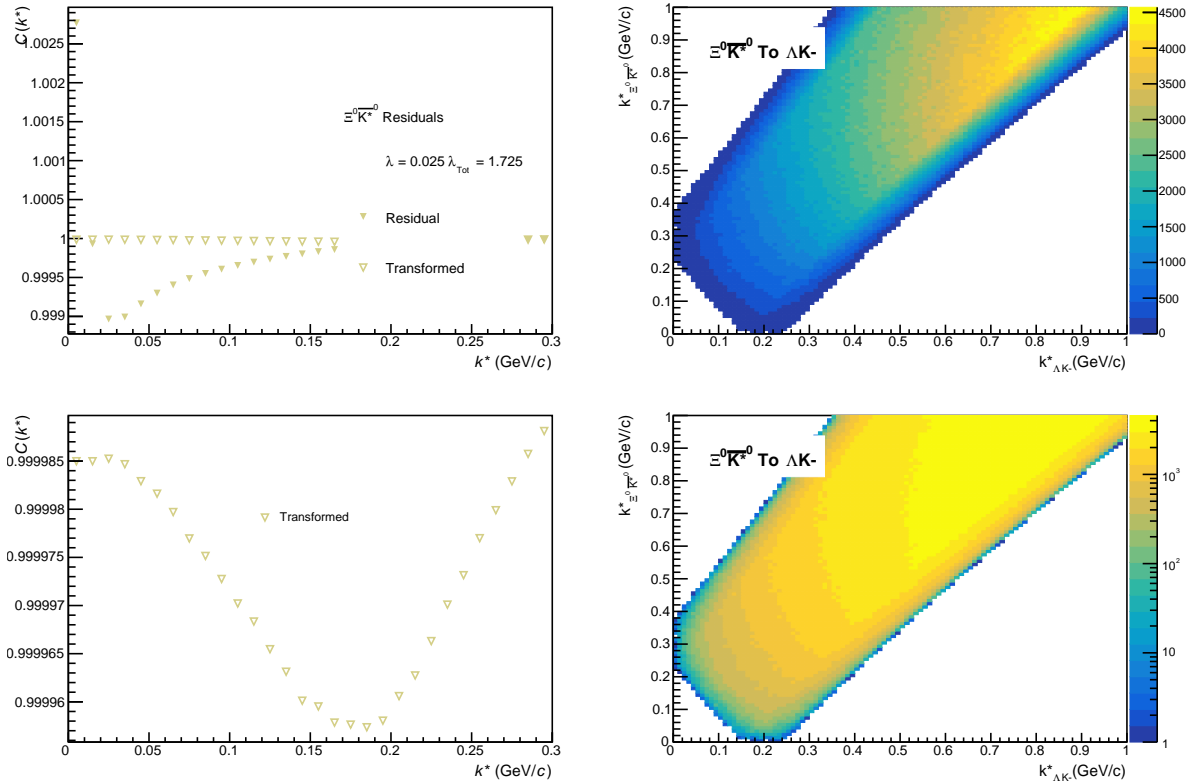


**Fig. 67:** Residuals:  $\Sigma^* - K^- \rightarrow \Lambda K^-$  (0-10% Centrality)

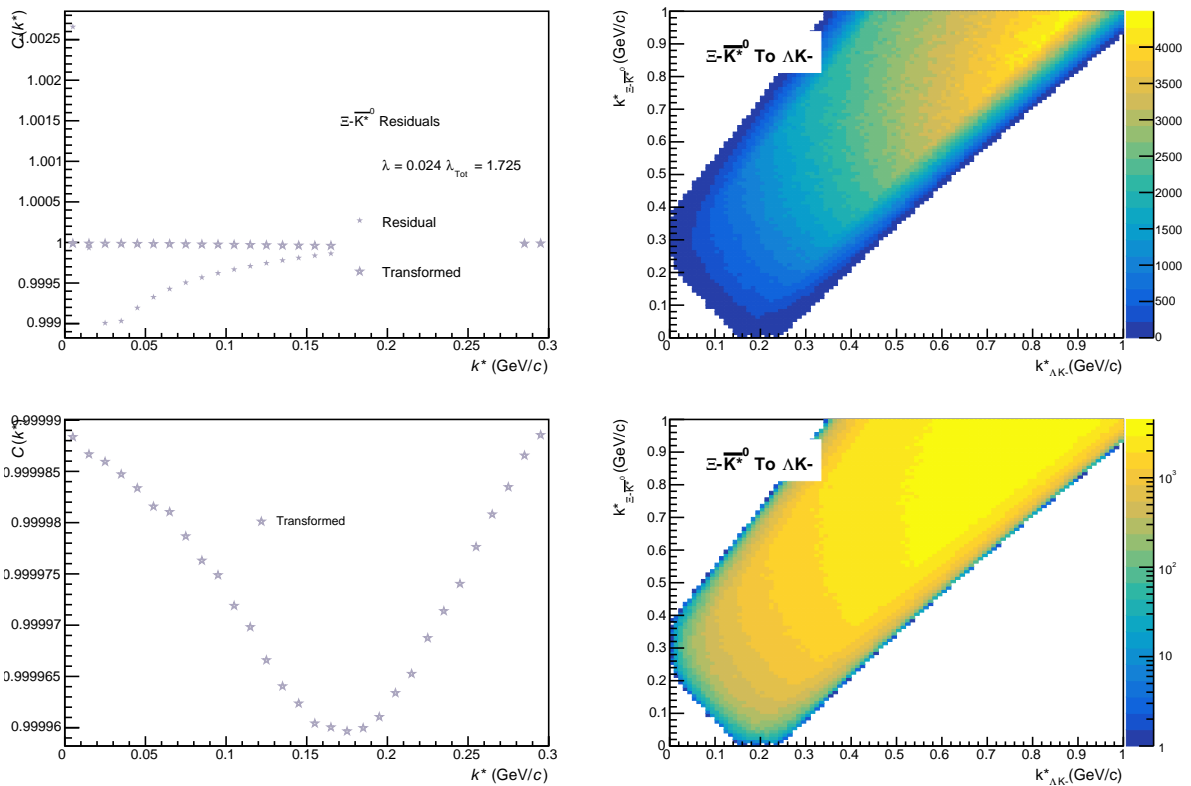

**Fig. 68:** Residuals:  $\Sigma^{*0} \text{K-}$  to  $\Lambda \text{K-}$  (0-10% Centrality)

**Fig. 69:** Residuals:  $\Lambda \bar{K}^*0$  to  $\Lambda \text{K-}$  (0-10% Centrality)



**Fig. 70:** Residuals:  $\Sigma^0 \bar{K}^{*0}$  to  $\Lambda K^-$  (0-10% Centrality)

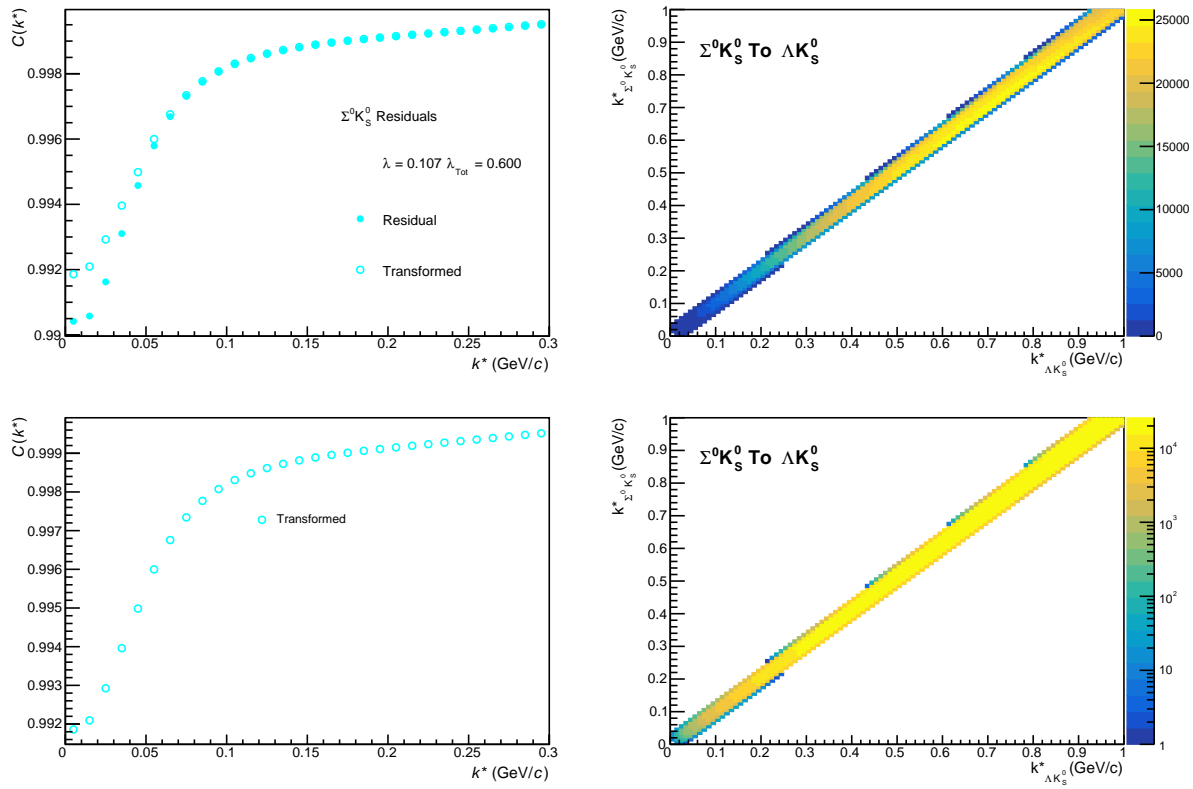


**Fig. 71:** Residuals:  $\Xi^0 \bar{K}^{*0}$  to  $\Lambda K^-$  (0-10% Centrality)

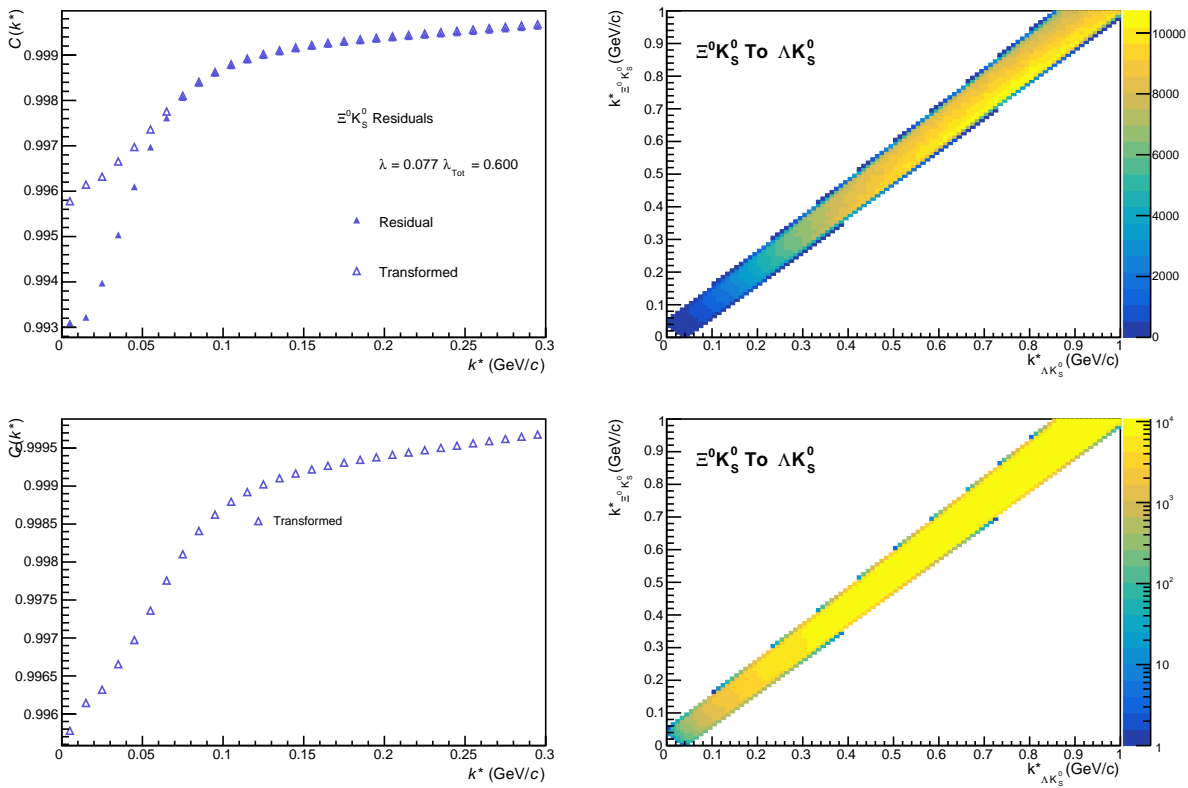


**Fig. 72:** Residuals:  $\Xi-\bar{K}^{*0}$  to  $\Lambda K^-$  (0-10% Centrality)

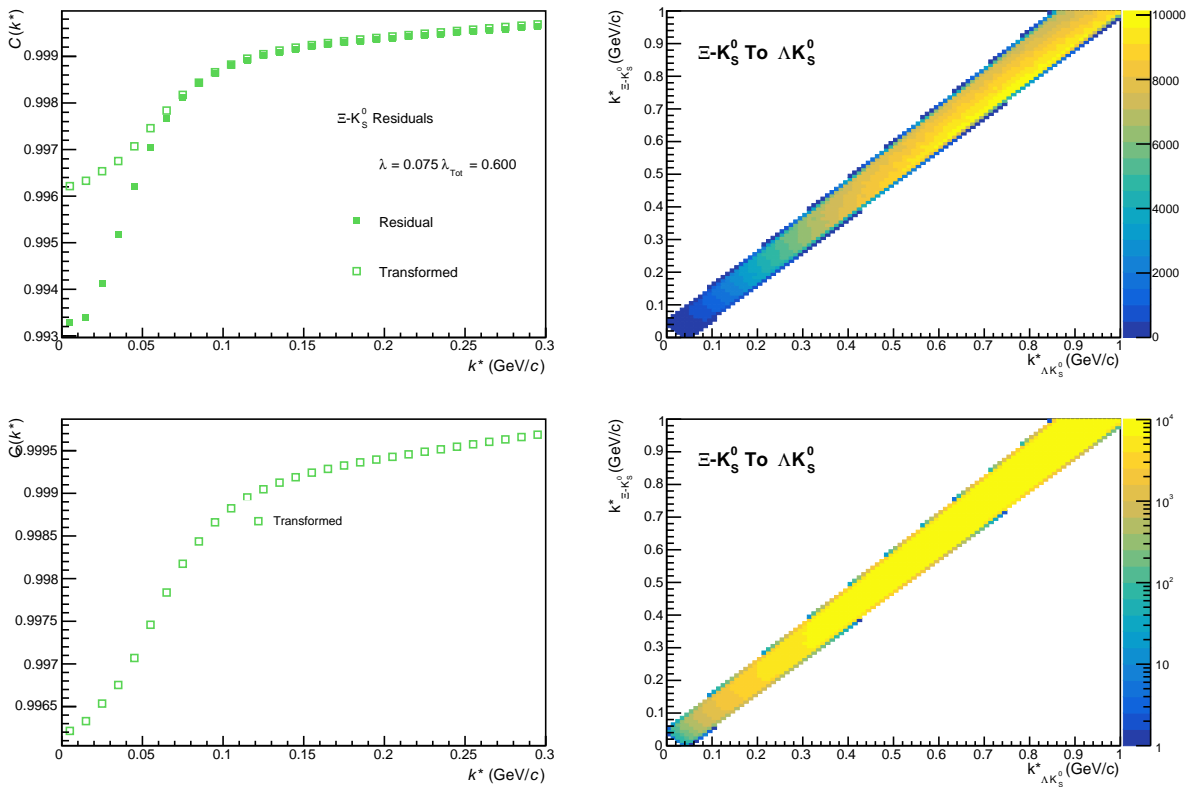
717 **9.1.3  $\Lambda K_S^0$  Residuals**



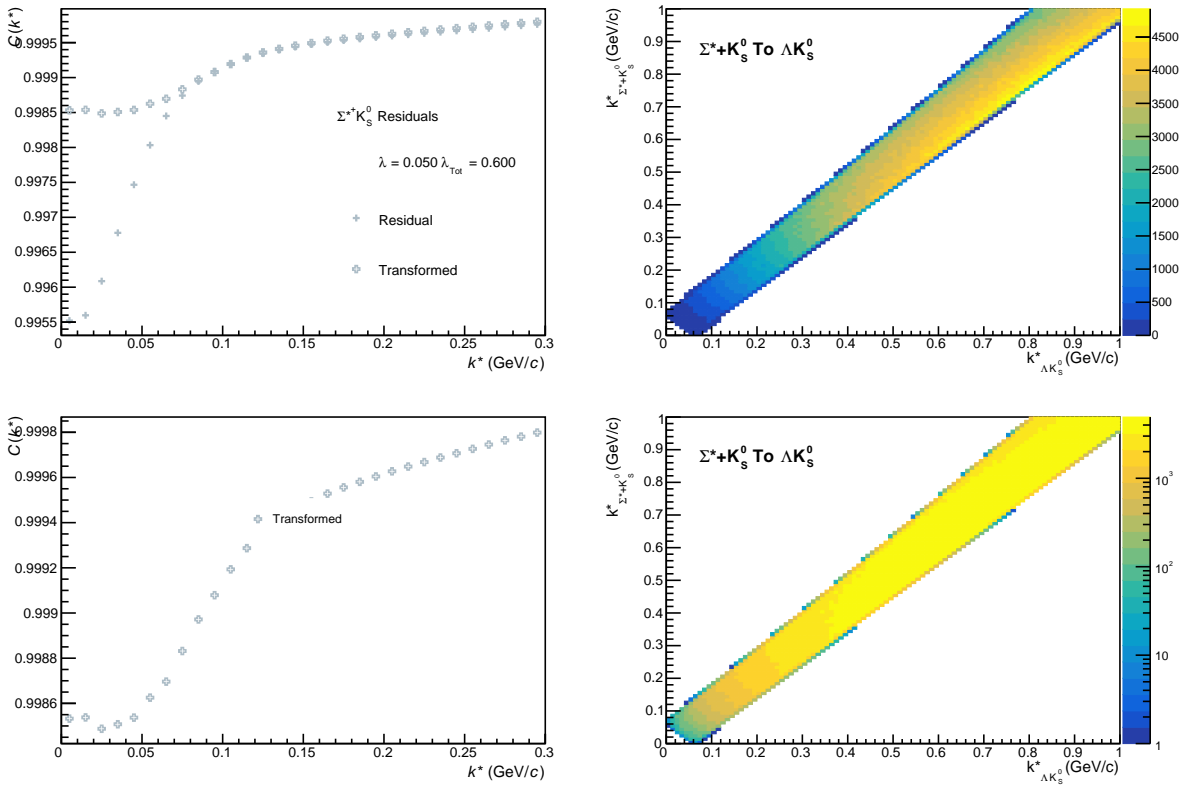
**Fig. 73:** Residuals:  $\Sigma^0 K_S^0$  to  $\Lambda K_S^0$  (0-10% Centrality)



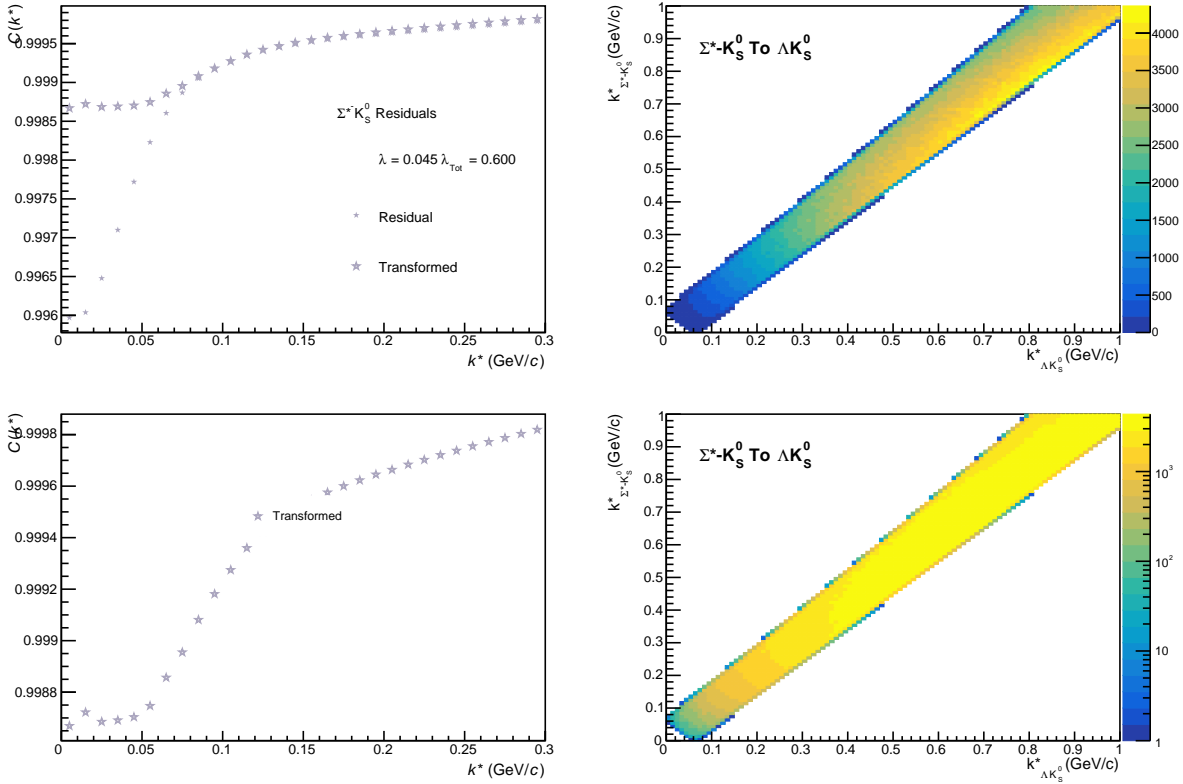
**Fig. 74:** Residuals:  $\Xi^0 K_S^0$  to  $\Lambda K_S^0$  (0-10% Centrality)



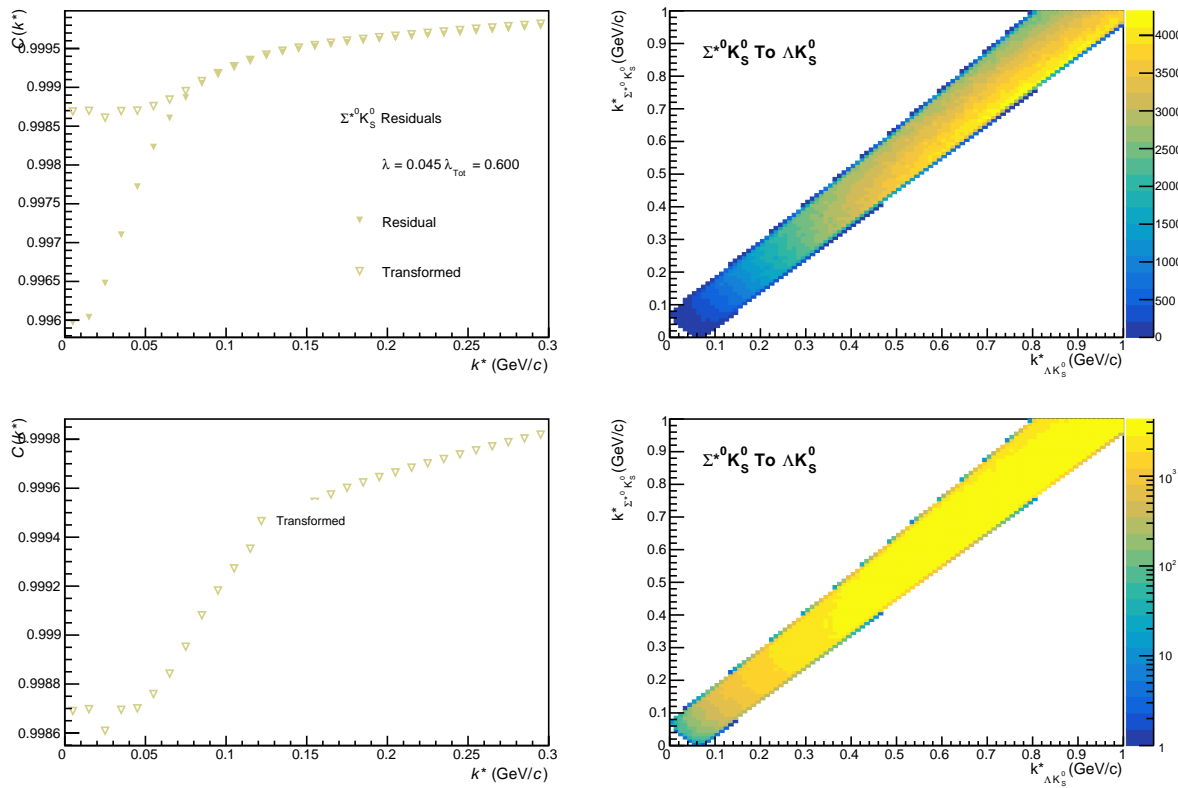
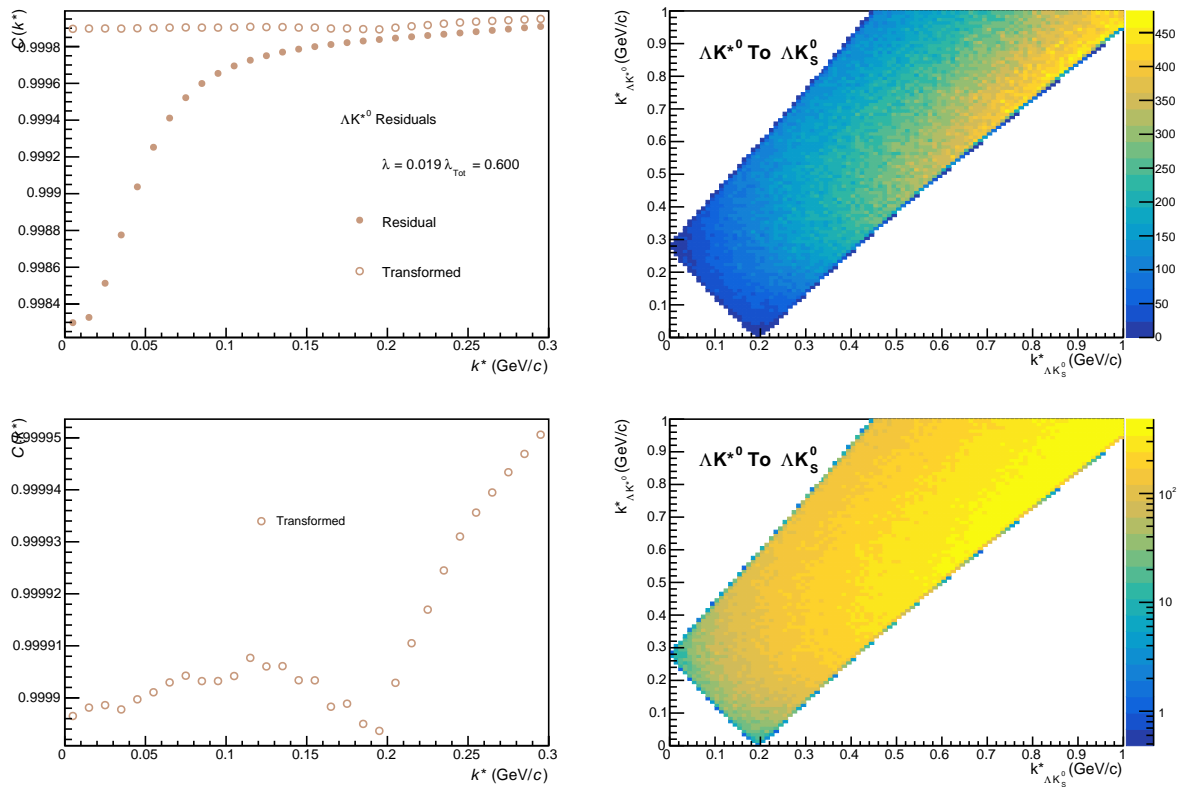
**Fig. 75:** Residuals:  $\Xi^- K_S^0$  to  $\Lambda K_S^0$  (0-10% Centrality)

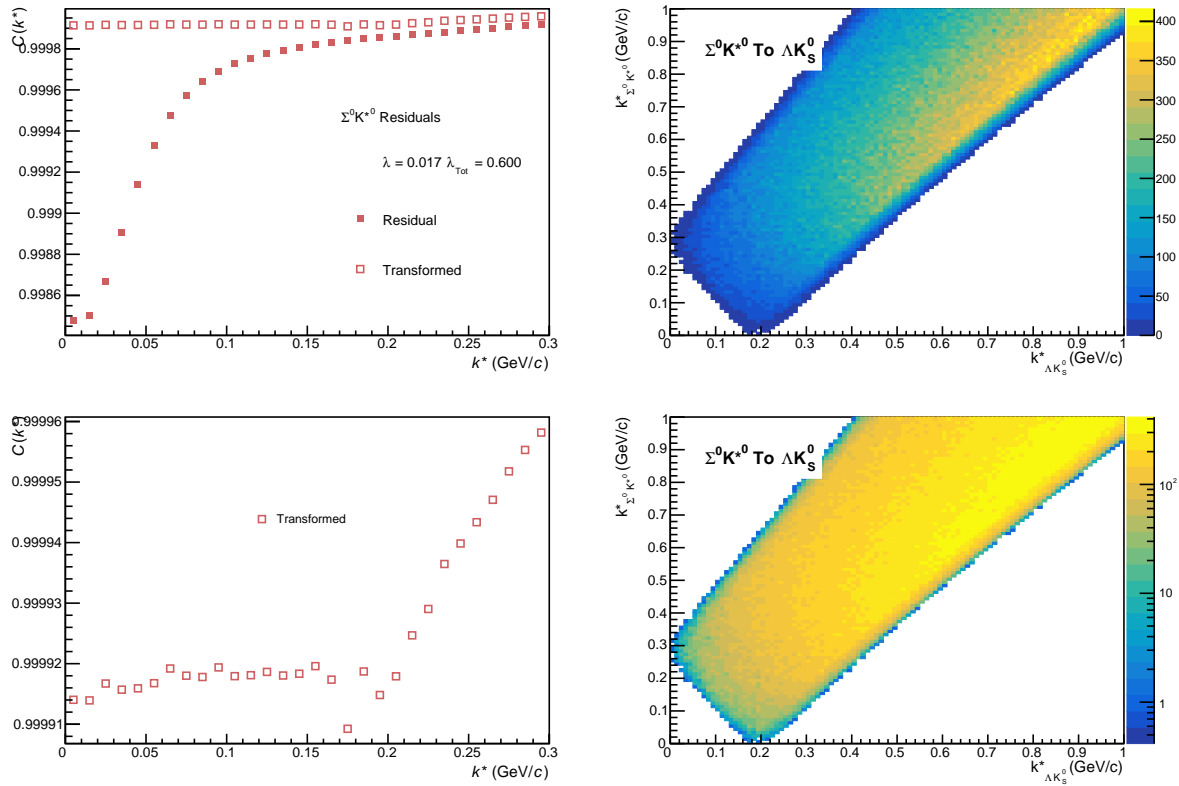


**Fig. 76: Residuals:  $\Sigma^*+K_S^0$  to  $\Lambda K_S^0$  (0-10% Centrality)**

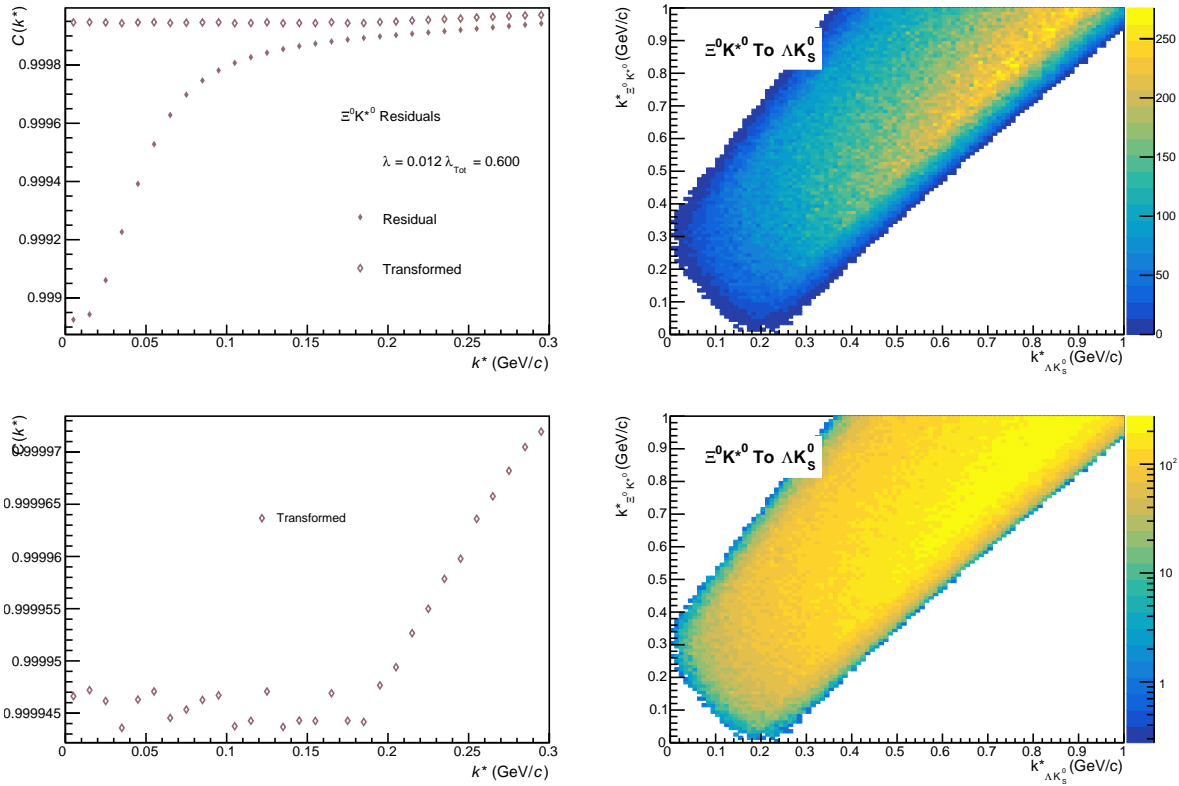


**Fig. 77: Residuals:  $\Sigma^- K_S^0$  to  $\Lambda K_S^0$  (0-10% Centrality)**

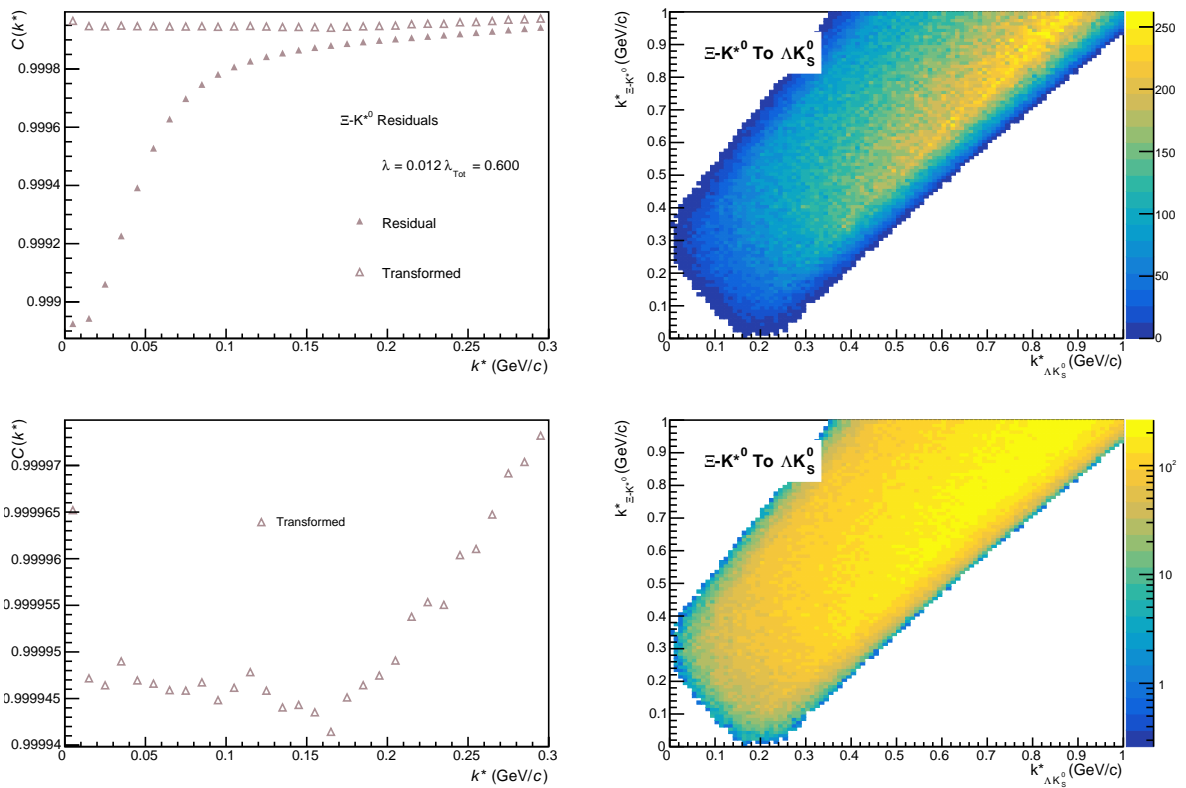

**Fig. 78:** Residuals:  $\Sigma^{*0} K_S^0$  to  $\Lambda K_S^0$  (0-10% Centrality)

**Fig. 79:** Residuals:  $\Lambda K^{*0}$  to  $\Lambda K_S^0$  (0-10% Centrality)



**Fig. 80:** Residuals:  $\Sigma^0 K^{*0}$  to  $\Lambda K_S^0$  (0-10% Centrality)



**Fig. 81:** Residuals:  $\Xi^0 K^{*0}$  to  $\Lambda K_S^0$  (0-10% Centrality)



**Fig. 82:** Residuals:  $\Xi\text{-}K^{*0}$  to  $\Lambda K_S^0$  (0-10% Centrality)

## References

- [1] R. Lednicky and V. L. Lyuboshitz. *Sov. J. Nucl. Phys.*, 35:770, 1982.
- [2] Michael Annan Lisa, Scott Pratt, Ron Soltz, and Urs Wiedemann. Femtoscopy in relativistic heavy ion collisions. *Ann. Rev. Nucl. Part. Sci.*, 55:357–402, 2005.
- [3] S. E. Koonin. Proton Pictures of High-Energy Nuclear Collisions. *Phys. Lett.*, B70:43–47, 1977.
- [4] S. Pratt, T. Csorgo, and J. Zimanyi. Detailed predictions for two pion correlations in ultrarelativistic heavy ion collisions. *Phys. Rev.*, C42:2646–2652, 1990.
- [5] Richard Lednicky. Finite-size effects on two-particle production in continuous and discrete spectrum. *Phys. Part. Nucl.*, 40:307–352, 2009.
- [6] Adam Kisiel, Hanna Zbroszczyk, and Maciej Szymaski. Extracting baryon-antibaryon strong interaction potentials from  $p\bar{\Lambda}$  femtoscopic correlation functions. *Phys. Rev.*, C89(5):054916, 2014.
- [7] Jai Salzwedel and Thomas Humanic. Lambda femtoscopy in  $\sqrt{s_{NN}} = 2.76$  TeV Pb-Pb collisions at ALICE, Jan 2017. Presented 15 Dec 2016.
- [8] A Kisiel. Non-identical particle correlation analysis in the presence of non-femtoscopic correlations. *Acta Physica Polonica B*, 48:717, 04 2017.
- [9] Yan-Rui Liu and Shi-Lin Zhu. Meson-baryon scattering lengths in HB chi PT. *Phys. Rev.*, D75:034003, 2007.
- [10] Maxim Mai, Peter C. Bruns, Bastian Kubis, and Ulf-G. Meissner. Aspects of meson-baryon scattering in three and two-flavor chiral perturbation theory. *Phys. Rev.*, D80:094006, 2009.
- [11] Jaroslav Adam et al. One-dimensional pion, kaon, and proton femtoscopy in Pb-Pb collisions at  $\sqrt{s_{NN}} = 2.76$  TeV. *Phys. Rev.*, C92(5):054908, 2015.